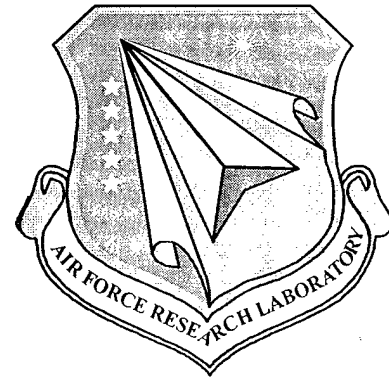


**ENERGETIC MATERIALS PYROMETRY**

---

**MARK F. HOPKINS**  
**Air Force Research Laboratory**  
**AFRL/MNSA**  
**101 West Eglin Blvd.**  
**Eglin AFB, Florida 32542-6810**



**EUSTACE L. DERNIAK**  
**and**  
**JOHN P. GARCIA**  
**University of Arizona**  
**Optical Sciences Center**  
**University of Arizona**  
**Tucson, AZ 85721**

**MARCH 2000**

**FINAL REPORT FOR PERIOD (OCT 1996 - OCT 1998)**

**APPROVED FOR PUBLIC RELEASE- DISTRIBUTION UNLIMITED**

**AIR FORCE RESEARCH LABORATORY, MUNITIONS DIRECTORATE**

**Air Force Materiel Command ■ United States Air Force ■ Eglin Air Force Base**

**20011005 119**

## NOTICE

When Government drawings, specifications, or other data are used for any purpose other than in connection with a definitely Government-related procurement, the United States Government incurs no responsibility or any obligation whatsoever. The fact that the Government may have formulated or in any way supplied the said drawings, specifications, or other data, is not to be regarded by implication, or otherwise in any manner construed, as licensing the holder, or any other person or corporation; or as conveying any rights or permission to manufacture, use, or sell any patented invention that may in any way be related thereto.

This technical report is releasable to the National Technical Information Services (NTIS). At NTIS it will be available to the general public, including foreign nations.

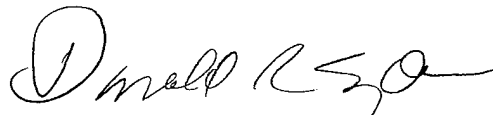
Contractor: Optical Sciences Center, University of Arizona  
Tucson, AZ 85721

This technical report has been reviewed and is approved for publication. Due to extenuating circumstances, it is not practical to edit this report for format and it is, therefore, approved, "as submitted" by the contractor.

FOR THE COMMANDER



PAUL K. LAIRD  
Technical Director  
Ordnance Division



DONALD R. SNYDER, III  
Program Manager

Anyone having need for a copy of this report should first contact the Defense Technical Information Center (DTIC) at the address shown below. If you are a registered DTIC User, DTIC can provide you with a copy. Please do not request copies from the Air Force Research Laboratory, Munitions Directorate. Requests for additional copies should be directed to:

Defense Technical Information Center (DTIC)  
8725 John J. Kingman Road, Ste 0944  
Ft Belvoir, VA 22060-6218

This report is published in the interest of the scientific and technical information exchange. Publication of this report does not constitute approval or disapproval of the ideas or findings

If your address has changed, if you wish to be removed from our mailing list, or if your organization no longer employs the addressee, please notify AFRL/MNMF, Eglin AFB FL 32542-6810, to help us maintain a current mailing list. Do not return copies of this report unless contractual obligations or notice on a specific document requires that it be returned.

REPORT DOCUMENTATION PAGE			Form Approved OMB No. 0704-0188	
Public reporting burden for this collection of information is estimated to average 1 hour per response, including the time for reviewing instructions, searching existing data sources, gathering and maintaining the data needed, and completing and reviewing the collection of information. Send comments regarding this burden estimate or any other aspect of this collection of information, including suggestions for reducing this burden, to Washington Headquarters Services, Directorate for Information Operations and Reports, 1215 Jefferson Davis Highway, Suite 1204, Arlington, VA 22202-4302, and to the Office of Management and Budget, Paperwork Reduction Project (0704-0188), Washington, DC 20503.				
1. AGENCY USE ONLY (Leave blank)		2. REPORT DATE October 1999		3. REPORT TYPE AND DATES COVERED FINAL October 1996-October 1998
4. TITLE AND SUBTITLE ENERGETIC MATERIAL PYROMETRY			5. FUNDING NUMBERS JON: 25022849 PE: 62602F PR: 2502 TA: 28 WU: 49	
6. AUTHOR(S) Mark F. Hopkins <sup>(1)</sup> Eustace L. Dereniak and John P. Garcia <sup>(2)</sup>				
7. PERFORMING ORGANIZATION NAME(S) AND ADDRESS(ES) AFRL/MNSA <sup>(1)</sup> Optical Sciences Center <sup>(2)</sup> 101 W. Eglin Blvd. University of Arizona Eglin AFB, FL 32542 Tucson, AZ 85721			8. PERFORMING ORGANIZATION REPORT NUMBER	
8. SPONSORING/MONITORING AGENCY NAME(S) AND ADDRESS(ES) Donald R. Snyder Telephone (850) 882-2005 ext. 215 snyder@eglin.af.mil AFRL/MNMF 101 W. Eglin Blvd Eglin AFB, FL 32542			10. SPONSORING/MONITORING AGENCY REPORT NUMBER AFRL-MN-EG-TR-2001-7066	
11. SUPPLEMENTARY NOTES				
12a. DISTRIBUTION/AVAILABILITY STATEMENT Approved for public release; distribution unlimited.			12b. DISTRIBUTION CODE	
13. ABSTRACT: THIS REPORT IS FOR AN IN-HOUSE EFFORT In this research, a remotely located, high-speed, infrared (IR) camera is used to obtain detailed measurements of the passive radiation from an object in an energetic environment. This radiation information is used to determine both the emissivity and the temperature of the surface of an object. However, before the temperature or emissivity was determined, the functional form of the emissivity was assumed to be an $M^{\text{th}}$ degree polynomial with respect to wavelength dependence. Using a commercial Fourier transform spectrometer, this functional form was verified to accuracy's on the order of 0.1%, to be a polynomial of the second degree. With the advent of large (greater than 128 X 128 pixels), high-speed, IR detector arrays, it has now become possible to realize IR imaging spectrometers that have very high spatial resolution. The IR spectrometer system developed in this research utilized a large detector array to allow multiple spectral images to be formed simultaneously on the image plane, with the information from each spectral image being concurrently collected. In conjunction with the correct emissivity model, this imaging IR spectrometer can determine the temperature of the surface of an object within an energetic environment to within $\pm 5$ degrees Celsius. These experimentally verified temperature/emissivity maps can then be integrated into the newly developed computer models. This additional information will result in more accurate computer codes for modeling the energetic environment. In turn, this will allow the weapon designer to optimize weapon performance with respect to different materials, geometries and kinetics.				
2. SUBJECT TERM Pyrometry, Emissivity, Spectrometer, High-Speed, Infrared, Temperature Measurement, Remote Sensing.			15. NUMBER OF PAGES 185	
			16. PRICE CODE	
17. SECURITY CLASSIFICATION OF REPORT UNCLASSIFIED	18. SECURITY CLASSIFICATION OF THIS PAGE UNCLASSIFIED	19. SECURITY CLASSIFICATION OF ABSTRACT UNCLASSIFIED	20. LIMITATION OF ABSTRACT U/L	

NSN 7540-01-280-5500

(Rev. 2-89) Prescribed by ANSI Std. Z39-18

Standard Form 298

## PREFACE/SPONSOR COMMENTS

This report is the final results of the experimentation and research conducted by Dr. Mark F. Hopkins while an employee of the Air Force Research Laboratory Munitions Directorate at Eglin AFB, Florida. Dr. Hopkins performed much of this research in the Instrumentation Research Facility and subsequent research at the Advanced Warhead Experimentation Facility Site C-64. Much of this research formed the basis for this dissertation, submitted in partial fulfillment of the requirements for an advanced degree at the University of Arizona while on Long Term Full Time Educational Leave and Leave of Absence. Dr. Hopkins successfully constructed and demonstrated a snapshot pyrometer based on these principles and presented that data at various SPIE Optical Sensing symposia and DOD/DOE technical symposia. He is now the chief scientist with Optical Insights LLC, 1807 Second Street, Suite #1, Santa Fe, NM 87505, Telephone (877)-4-OPT-INS; Local 1-505-955-1585, <http://www.optical-insights/contact.htm>. Several other papers were published by Dr. Hopkins and Dr. Dereniak that pertain to this study. Simultaneously with this effort, a 6.1 funded effort was being conducted for us by Dr. Dereniak and Dr. Garcia at University of Arizona. This work is included in this report for completeness. Other related references include.

-- M. F. Hopkins, et al, "Measuring temperature in a munition environment: optical pyrometer results compared to code predictions," Proc. SPIE, San Diego, July 1997.

-- M. F. Hopkins, "Multi-spectral measurement using a novel high-speed imaging pyrometer," Proc. SPIE, San Diego, July 1997.

-- M. F. Hopkins, "Infrared Imaging Spectrometer for Measurement of Temperature in High Speed Events," Ph.D. Dissertation, University of Arizona, October 1998.

-- M. R. Descour, C. E. Volin, T. M. Gleason, E. L. Dereniak, M. F. Hopkins, D. W. Wilson, and P. D. Marker, "Demonstration of a computer-tomography imaging spectrometer using a computer-generated hologram disperser," Applied Optics, Vol. 36, No. 2, Jan. 1997.

-- M. F. Hopkins, "Four-color pyrometer for metal emissivity characterization," Proc. SPIE, Vol. 2599, p. 294-301, Three-dimensional and Unconventional Imaging for Industrial Inspection, Oct. 1995.

-- E. L. Dereniak and M. F. Hopkins, "Feasibility study using an infrared camera and fiber optic bundle to image piston temperature inside a running engine," TCN 94140, US Army-TACOM (1994).

# TABLE OF CONTENTS

PREFACE/SPONSOR COMMENTS.....	iv
SECTION I. ENERGETIC MATERIAL PYROMETRY. HOPKINS).....	1
Appendix A-Temperature Estimation Software.....	103
Appendix B- Amber Proview Software.....	125
References.....	131
SECTION II. FOUR COLOR PYROMETRY FOR METAL EMISSIVITY CHARACTERIZATON. (HOPKINS).....	135
SECTION III. BEHIND PANEL DEBRIS TEMPERATURE PROFILOMETRY (DERENIAK AND GARCIA) .....	145
SECTION IV. BEHIND PANEL DEBRIS TEMPERATURE PROFILOMETRY WHITE PAPER. (DERENIAK AND GARCIA) .....	166
SECTION V. PATENT AWARD. (HOPKINS).....	172
DISTRIBUTION LIST .....	183
ENDNOTES.....	184

# **Section I**

## **INFRARED IMAGING SPECTROMETER FOR MEASUREMENT OF TEMPERATURE IN HIGH-SPEED EVENTS**

by

**Mark Franklin Hopkins<sup>(1)</sup>**

**AFRL/MNSA  
101 W EGLIN BLVD  
EGLIN AFB, FL**

<sup>1</sup> Now at Optical Insights LLC, Sante Fe, NM 87108

## ACKNOWLEDGMENTS

- The author would like to acknowledge the following persons for their help and support during his work and studies at the University of Arizona's Optical Sciences Center:
- Dr. Jack Gaskill for his understanding and insight into keeping the proper balance between the needs of the student and demands of the faculty and always with a healthy helping of humor.
- Dr. Roland Shack for his spirit for life and his door that is always open to talk about any problem in optics which often seems to lead to an appreciation for elegance in science.
- Dr. Angus Macleod for his energy and enthusiasm that reminds me that it should always be fun.
- Dr. Eiji Yafuso for teaching how two colliding billiard balls always separate at a right angle.
- Mr. Don Snyder my supervisor at Eglin AFB for not acting so much like a supervisor and for being an endless source of information.
- Mr. Mike Van Tassel for his extreme patience ordering the equipment I needed to complete my research.
- Dr. Yash Sabharwal for always standing in my corner and never letting me forget that, while I might be insane, I am not alone and I can always count on him.
- Dr. Cindi Vernold for always being there as my biggest supporter, which without, I would have not gone as far as I have gone, and with, I certainly will achieve my dreams.
- And to Cindi and Yash both for being my family.

## TABLE OF CONTENTS

INTRODUCTION.....	10
1. BACKGROUND.....	14
1.1. RADIATION LAW AND EMISSIVITY MODEL .....	14
1.2. SEPARATING TEMPERATURE AND EMISSIVITY FROM RADIANT POWER MEASUREMENTS.....	16
1.2.1. <i>Single-Color Pyrometry</i> .....	18
1.2.2. <i>Dual-Color Pyrometry</i> .....	19
1.2.3. <i>Multi-Color Pyrometry</i> .....	24
1.3. PRIOR PYROMETER INSTRUMENTATION .....	25
2. EMISSIVITY MODEL DEVELOPMENT, TEST AND ANALYSIS .....	29
2.1. VALIDATION OF THERMAL EQUILIBRIUM ASSUMPTION .....	29
2.2. EMISSIVITY BEHAVIOR FOR IDEAL METAL .....	33
2.2.1. <i>Free Electron Model</i> .....	35
2.2.2. <i>Effects of Surface on Emissivity</i> .....	41
2.2.2.1. Fresnel Reflection at Surface Boundary.....	41
2.2.2.2. Surface Topography .....	45
2.2.2.3. Surface Chemistry .....	47
2.3. THE OVERALL EMISSIVITY MODEL.....	48
2.4. VERIFICATION OF MODEL.....	49
2.5. ALGORITHM DESIGN .....	54
2.5.1. <i>Algorithm Design And Simulation (Gaussian Elimination)</i> .....	54
2.5.2. <i>Singular Value Decomposition</i> .....	57
2.5.3. <i>Levenberg Marquardt Nonlinear Optimization</i> .....	60
2.6. NOISE CONTRIBUTION TO TEMPERATURE ERROR .....	61

## TABLE OF CONTENTS (Continued)

3. IMAGING PYROMETER DESIGN .....	64
3.1. GENERAL DESIGN .....	65
3.2. INTERFERENCE FILTER DESIGN .....	69
3.3. OPTICAL LENS DESIGN .....	71
3.4. RADIOMETRY .....	77
4. HIGH SPEED PYROMETER FABRICATION .....	79
4.1. MULTI-SPECTRAL CAMERA .....	79
4.2. CALIBRATION: .....	85
4.3. EXPERIMENTAL SETUP .....	90
4.4. VALIDATION .....	91
4.5. RESULTS .....	92
5. CONCLUSIONS .....	101

## LIST OF FIGURES

FIGURE 1-1: OPERATIONAL SCENARIO FOR EXPLOSIVELY FORMED PROJECTILES.....	10
FIGURE 1-2: IN PENETRATING A HARD TARGET, THE WEAPON EXPERIENCES STRESS INDUCED BY THE MULTI LAYERS OF STEEL AND CONCRETE. ....	11
FIGURE 2-1: SURFACE FIELDS OF A METAL SAMPLE.....	42
FIGURE 2-2: VALIDATION EXPERIMENT. THE COMPONENTS FOR THIS EXPERIMENT WERE DELIVERED ON A CONTRACT FROM THE GOVERNMENT TO BOMEM, INC.....	52
FIGURE 2-3: PLOT OF ALUMINUM EMISSIVITY PROFILE. THE SOLID LINE REPRESENTS A SECOND DEGREE POLYNOMIAL.....	53
FIGURE 2-4: PLOT OF COOPER EMISSIVITY PROFILE. THE SOLID LINE REPRESENTS SECOND DEGREE POLYNOMIAL. ....	53
FIGURE 2-5: SIMULATED FILTERS AND EMISSIVITY TO TEST ALGORITHM PERFORMANCE.....	57
FIGURE 2-6: SYSTEM TEMPERATURE ACCURACY VERSUS DETECTOR INTEGRATION TIME.....	62
FIGURE 2-7: SYSTEM TEMPERATURE ACCURACY VERSUS SIGNAL TO NOISE. ....	62
FIGURE 3-1: IMAGING PYROMETER.....	64
FIGURE 3-2: THE PROPERTY OF AN INTERFERENCE FILTER CHANGING ITS PASS BAND AS THE ANGLE OF INCIDENCE ON THE FILTER CHANGES.....	65
FIGURE 3-3: INTERFERENCE FILTER BEHAVIOR WHEN TILTED.....	66
FIGURE 3-4: LENS CONFIGURATION WITH UNTILTED FILTER.....	67
FIGURE 3-5: LENS CONFIGURATION WITH TILTED FILTER AND MIRROR TO RETURN REFLECTED ENERGY SUBSEQUENTLY RETURNING TO THE FILTER AT AN INCREMENTAL ANGLE.....	68
FIGURE 3-6: USING A LINEAR VARIABLE FILTER TO GET THE PROPER AMOUNT OF WAVELENGTH SHIFTS OUT OF EACH SPECTRAL IMAGE. ....	70
FIGURE 3-7: DISCRETE FILTER APPROACH FOR EFFECTIVE FILTER SEPARATION.....	70
FIGURE 3-8: PARAXIAL LENS DESIGN FOR THE FOURTH REFLECTED RAY THROUGH THE INTERFERENCE FILTER.....	73

## LIST OF FIGURES (Continued)

FIGURE 3-9: PARAXIAL LENS DESIGN FOR THE THIRD REFLECTED RAY THROUGH THE INTERFERENCE FILTER .....	73
FIGURE 3-10: PARAXIAL LENS DESIGN FOR THE SECOND REFLECTED RAY THROUGH THE INTERFERENCE FILTER .....	74
FIGURE 3-11: PARAXIAL LENS DESIGN FOR THE FIRST REFLECTED RAY THROUGH THE INTERFERENCE FILTER .....	74
FIGURE 3-12: LENS DESIGN FOR THE FOURTH REFLECTED RAY THROUGH THE INTERFERENCE FILTER .....	76
FIGURE 4-1: HIGH SPEED PYROMETER CAMERA CONFIGURATION. THE LENS ASSEMBLY IS AT A SLIGHT ANGLE FROM THE FRONT FACE OF THE CAMERA, WHICH IS DONE TO INCORPORATE THE UNIQUE LENS DESIGN.....	80
FIGURE 4-2: DISCONNECTION OF FILTER ASSEMBLY FROM MAIN CAMERA BODY. THE ASSEMBLY IS HELD TO THE FRONT FACE OF THE CAMERA VIA FOUR MOUNTING BOLTS. THE IMAGING LENS FITS IN THE STANDARD AMBER MOUNT IN THE FRONT OF THE CAMERA. BOTH THE OBJECTIVE AND IMAGING LENSES WERE MANUFACTURED BY DIOP. ....	81
FIGURE 4-3: INTERFERENCE FILTER AND MIRROR. THE MIRROR THAT FOLDS THE MULTIPLE BEAMS BACK TOWARDS THE INTERFERENCE FILTERS CAN BE SEEN THROUGH THE SMALL HOLE DIRECTLY ABOVE THE FILTERS. ON THE OTHER SIDE OF THIS ASSEMBLY ARE THE COLLIMATING LENS AND THE FIELD STOP. ....	82
FIGURE 4-4: FIELD-STOP AND COLLIMATING LENS. THE COLLIMATING LENS IS BETWEEN THE INTERFERENCE FILTERS AND THE FIELD-STOP AND CONSEQUENTLY CANNOT BE SEEN IN EITHER VIEW. THE FIELD-STOP IS MADE FROM TWO RAZOR BLADES.....	83
FIGURE 4-5: EXPERIMENTAL TEST ITEM AND BLACK BODY USED IN SYSTEM CALIBRATION .....	84
FIGURE 4-6: CALIBRATION SETUP .....	85

## List of Figures (Continued)

FIGURE 4-7: ERROR OF MONOCHROMATOR FROM CALIBRATION RUN TO CALIBRATION RUN. THIS DATA WAS TAKEN DURING NORMAL WORKING HOURS AND WITH THE MANUFACTURE'S POWER SUPPLY. ....	87
FIGURE 4-8: ERROR OF MONOCHROMATOR FROM CALIBRATION RUN TO CALIBRATION RUN. THIS DATA WAS TAKEN AFTER NORMAL WORKING HOURS AND WITH A POWER ONE INC., F15-15-A POWER SUPPLY. ....	88
FIGURE 4-9: DETECTOR MASKING APPROACH TO REMOVE THE AFFECT OF THERMAL VARIATION CAUSED BY AIR-CONDITIONING IN LABORATORY. THESE FLUCTUATIONS WERE AS MUCH AS 2% OVER A SINGLE CALIBRATION RUN.....	89
FIGURE 4-10: THE FILTER BANDPASS RESPONSE FOR EACH OF THE FOUR FILTERS. THE FIRST PASS CORRESPONDS TO THE FIRST FILTER ON THE LEFT, THE SECOND PASS IS THE SECOND FILTER. AND SO FORTH. NOTICE THAT EACH OF THE FILTERS PEAK RESPONSE IS GRADUALLY DECREASING. THIS CORRESPONDS PRIMARILY, TO OUT-OF-BAND ABSORPTION. ....	89
FIGURE 4-11: TEST AND CALIBRATION SETUP .....	90
FIGURE 4-12: PROVIEW ELECTRONICS PACKAGE .....	91
FIGURE 4-13: THE AGEMA THERMOLVISION IR CAMERA USED FOR VALIDATION.....	92
FIGURE 4-14: PLOT OF THE EMISSIVITY OF A HEATED PIECE OF ALUMINUM AT VARIOUS TEMPERATURES. THE SURFACE OF THE SAMPLE WAS PREPARED USING 200 GRIT SANDPAPER. ....	94
FIGURE 4-15: PLOT OF THE EMISSIVITY OF A HEATED PIECE OF COPPER AT VARIOUS TEMPERATURES. THE SURFACE OF THE SAMPLE WAS PREPARED USING 200 GRIT SANDPAPER. ....	94
FIGURE 4-16: PLOT OF THE EMISSIVITY OF A HEATED PIECE OF STEEL AT VARIOUS TEMPERATURES. THE SURFACE OF THE SAMPLE WAS PREPARED USING 200 GRIT SANDPAPER. ....	95

## Abstract

Munition development has always been driven by the necessity of delivering enough explosives to a targeted object to destroy it. Targets that are protected by steel reinforced concrete housings have become increasingly more difficult to destroy. Improvements must be made in munitions engineering design to either deliver more payload to the target or to make the weapon more potent. In most cases, due to aircraft weight limitations, the delivery of more payload is not an option. Therefore, improving the destructive power of a weapon of a given payload requires the use of more powerful explosives. However, when the potency of an explosive is increased, its sensitivity to premature detonation also increases.

The characteristics of the metal casing containing the explosive contribute significantly to the weapon's detonation sensitivity. The casing experiences significant heating during weapon penetration. This dynamic heating can cause the weapon to detonate before it reaches its target location. In the past, computer codes used to model detonating weapons have not heating into account in their performance predictions. Consequently, the theoretical models and the actual field tests are not in agreement. New models, that include temperature information, are currently being developed which are based on work done in the area of computational fluid dynamics.

In this research, a remotely located, high-speed, infrared (IR) camera is used to obtain detailed measurements of the passive radiation from an object in an energetic environment. This radiation information is used to determine both the emissivity and the temperature of the surface of an object. However, before the temperature or emissivity was determined, the functional form of the emissivity was assumed to be an  $M^{th}$  degree polynomial with respect to wavelength dependence. Using a commercial Fourier transform spectrometer, this functional form was verified to accuracy's on the order of 0.1%, to be a polynomial of the second degree.

With the advent of large (greater than 128 X 128 pixels), high-speed, IR detector arrays, it has now become possible to realize IR imaging spectrometers that have very high spatial resolution. The IR spectrometer system developed in this research utilized a large detector array to allow multiple spectral images to be formed simultaneously on the image plane, with the information from each spectral image being concurrently collected. In conjunction with the

correct emissivity model, this imaging IR spectrometer can determine the temperature of the surface of an object within an energetic environment to within  $\pm 5$  degrees Celsius. These experimentally verified temperature/emissivity maps can then be integrated into the newly developed computer models. This additional information will result in more accurate computer codes for modeling the energetic environment. In turn, this will allow the weapon designer to accurately optimize weapon performance with respect to different materials, geometries and kinetics.

## Introduction

In munition development there has been a great need to accurately characterize the materials found in exploding and deflagrating reactions to determine when a weapon may fail. The primary area of concern within munition development is penetrator and explosively formed projectile type weapons. With explosively formed projectiles, the first concern is to understand how the projectile material (typically a copper alloy) responds to the explosive charge. After formation, the concern is to understand how the projectile will propagate toward the target. Finally, understanding how the projectile interacts with the target is critical for effective weapon design. The operational scenario of the explosively formed projectile is shown in Fig. 1-1.

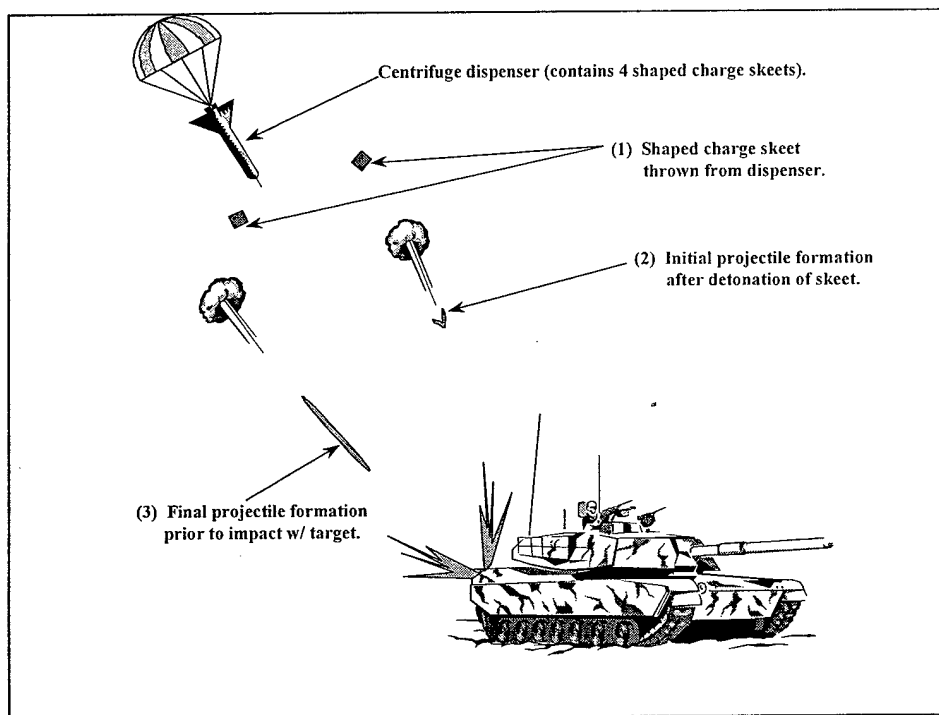


**Figure 1-1:** Operational scenario for explosively formed projectiles.

Determining the temperatures for each of the three stages in the scenario can become quite involved. However, the factors that largely determine instrumentation needs are; time of event, image resolution, and the number of spectral images needed for accurate temperature reconstruction.

For penetrators, the primary concern is understanding how the casing material (typically an iron alloy) responds to the stresses of penetrating a hardened target as shown in Fig. 1-2.

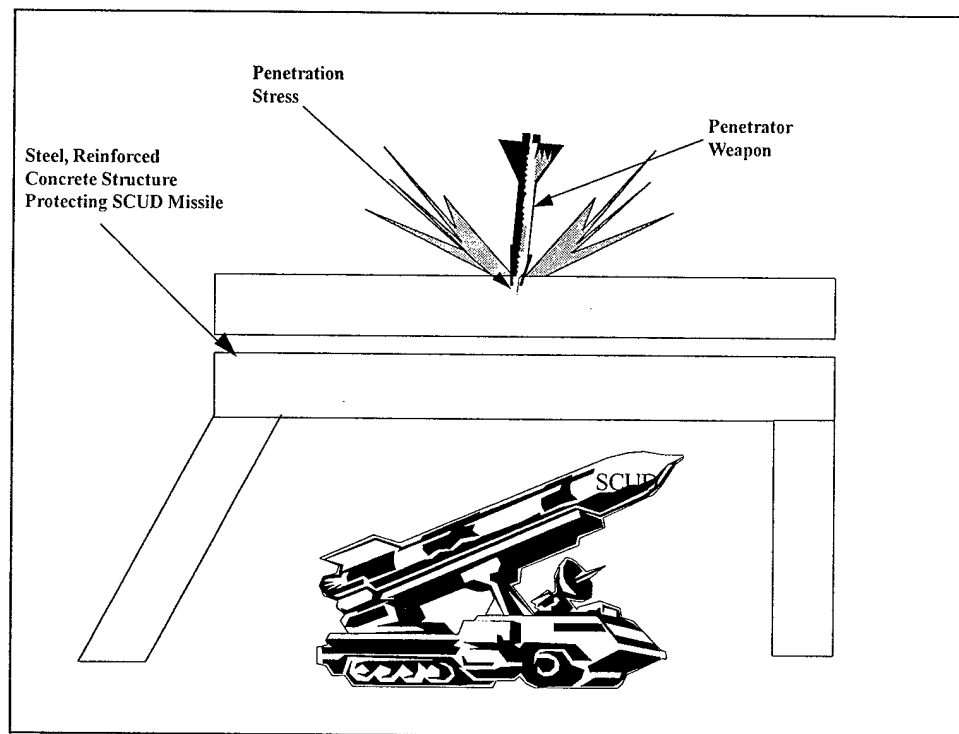


**Figure 1-2:** In penetrating a hard target, the weapon experiences stress induced by the multi layers of steel and concrete.

During hard-target penetration, excessive heating of the weapon casing can cause massive warping and/or premature detonation of the bomb. Thus, there is a need to characterize how the explosives inside the casing are affected by these temperature changes. This is an important aspect of understanding if the bomb will hold together until it reaches its target and subsequently detonates in the designed manner. Determination of the dynamically changing temperature of a

weapon's casing material is essential to characterizing its plastic deformation characteristics and failure points.

Computer code simulations have been developed as input to munition design and development. In recent years, the munitions community has recognized that the inclusion of temperature effects in these high-speed deformation models is becoming more critical. The code developers have shown that when temperature characterizations are included in their models, significantly more accurate predictions are made. However, for the accurate temperature analysis of the next generation of weapons, the development of new innovative pyrometry instrumentation is required. There are two main forces that drive the level of difficulty associated with making temperature measurements in an energetic environment. Measuring temperature in these environments is difficult due to high rates of object motion (on the order of 300 meters per second or Mach 1.0) and the unknown emissivity. In addition, the temperature may also be changing at rates that are on the order of hundreds of degrees per millisecond. To develop the proper hardware that can optically measure temperature it is important to break down the overall requirement into its fundamental instrumentation needs. The temporal and spatial resolution factors of the instrument design are somewhat straightforward and easy to determine from basic radiometry. Conversely, before a pyrometer is designed, the number of necessary spectral images needed for accurate temperature prediction must be determined. Here the functional form of the target's IR spectrum, in terms of its emissivity and temperature, will determine the necessary number of wavelengths or spectral bandwidths.

IR radiative characteristics can be separated into an emissivity contribution and a temperature contribution. A material's spectral emissivity is defined as the wavelength dependent coefficient that characterizes the optical radiation of a surface. To find the emissivity of a material measurement of the material's radiant power at each discrete wavelength and a blackbody's radiant power at the same discrete wavelength are obtained. Temperature, area, and solid angle of emission are kept constant during these measurements. The emissivity for each wavelength is then found by taking the ratio of these two values.<sup>1</sup> The functional dependence of the resulting emissivity curve can often be accurately modeled as an  $M^{th}$ -degree polynomial. The degree of this polynomial, and the functional form of the temperature contribution (typically

following the Planck's radiation law), directly dictate the number of wavelengths required to accurately determine temperature.

This research discusses the design, development and test of a four-color, IR, high-speed, imaging spectrometer. This spectrometer, in conjunction with accurate emissivity models and temperature radiation model, is used to produce an optical pyrometer system that solves some of the temperature measurement needs of the munition development community. Specifically, the characterization of dynamic temperature changes of casing materials is investigated.

The goal of this research is to develop an accurate theoretical model for emissivity to be used with the four-color, IR, high-speed, imaging spectrometer to determine temperature. This optical pyrometer significantly reduces the instrumentation inaccuracies found in previous systems. This research will first discuss a brief history of pyrometry, laying the foundation for the importance of this work. This will lead to a discussion of a temperature measurement solution to the problem of material deformation. In addition to highly accurate, high-speed instrumentation, the accurate measurement of temperature requires the determination of an accurate emissivity model. Thus, a theoretical model for emissivity of metals will be presented. The accuracy of this model will be verified using a commercial Fourier transform spectrometer. The details of the design and test of a high-speed, IR, imaging spectrometer will follow. Combining the emissivity model with this spectrometer produces an optical pyrometer system that is shown to be capable of measuring temperature to within accuracies of  $\pm 5\text{ }^{\circ}\text{C}$ .

## 1. Background

When small amounts of force are applied to a material, it undergoes elastic deformation, but will return to its original condition after the force is released. Applying more and more force to the material will eventually cause it to reach its "yield point," where it will first begin to plastically deform and eventually fracture. Beyond this yield point, irreversible structural deformation change occurs. During plastic deformation, changes occur to the material resulting in crystal realignment and the generation of heat energy. Most of the deformation related energy is converted into heat. This heat energy manifests itself as a change in the material's temperature. Using a correctly determined emissivity model and temperature radiation model for the casing material, a spectrometer can be used to determine the temperature within an energetic environment. This chapter will discuss how a heated object generates an IR spectrum and the manner in which the temperature of this object is determined.

### 1.1. Radiation Law and Emissivity Model

A certain level of temperature dependent molecular vibration is inherent in all objects that are at a temperature above absolute zero. For materials that are both in thermal equilibrium and are assumed to have a continuum of energy states, the statistics of these energy modes follow a Maxwell-Boltzman distribution.<sup>2</sup> Although the actual radiation of optical energy takes on this statistical functional form, Planck showed that energy states do not occur as a continuum, but rather, they occur in discrete, quantized levels. Using this knowledge, Planck derived the ideal radiant exitance (where emissivity is equal to 1 at all wavelengths). The form of this ideal radiation law for materials in thermal equilibrium is known as the Planck distribution law.<sup>3</sup> This distribution dictates the amount of energy a given material will radiate at a given wavelength. If the material is a perfect radiator, freely radiating and absorbing energy to and from free space without any losses, it is referred to as a blackbody. The actual Planck distribution is modified by the material's total absorption. The total absorption of a material combines the effects due to a

material's inherent bulk absorption with the losses due to the manner in which energy couples through the material's surface. In addition, if a material allows no light transmission and it is in thermal equilibrium, then the material's total absorption will equal its emission (emissivity).

Incorrect assumptions cause errors in optical pyrometers. Often the largest contributor to this error is uncertainty in the functional form of the emissivity. Emissivity can be characterized with a  $M^{th}$  degree polynomial in wavelength with

$$\varepsilon_{eff}(\lambda) = a_{M+1}\lambda^M + a_M\lambda^{M-1} + a_{M-1}\lambda^{M-2} + \dots + a_1, \quad (1-1)$$

where the  $a$ 's are unknown constants that describe emissivity behavior.<sup>4</sup> If, for example, a given material has an emissivity that does not change with wavelength (a graybody), we would only need to determine  $a_1$ , because all the other  $a$ 's would be zero. Consequently, only two spectral measurements would be necessary to form two equations for the two unknowns: the constant,  $a_1$ , and the temperature,  $T$ . If a  $M^{th}$ -degree polynomial provides an accurate fit to a given material's emissivity profile, there will be  $M$  coefficients,  $a_{M+1} \dots a_2$ , of wavelength that will be unknown. With the unknown constant emissivity coefficient,  $a_1$ , and the unknown temperature,  $T$ , a minimum of  $M+2$  spectral measurements are required.

However, prior to this research, instrumentation system errors have been shown to increase strongly as the number of spectral measurements,  $M$ , increased. This has made the practice of taking more than two or three spectral measurements ineffective.<sup>5</sup> These instrumentation errors are primarily attributable to using separate detector arrays, each with its own support electronics and optics, to collect the individual spectral images. In addition, as higher degree polynomial models are used, the error in calculating the  $M^{th}$ -coefficient is weighted by a successively larger and larger wavelength term (i.e.  $\lambda = 5\mu m$ :  $\lambda^3 = 125$ ,  $\lambda^4 = 625$ ,  $\lambda^5 = 3125$ ) causing a wavelength to the  $M^{th}$  error in the calculated emissivity.

In the past, there have been many different methods used in attempting to measure the spectral characteristics of emissivity and temperature for a variety of materials. Depending on the assumptions made, and a priori knowledge of the material's characteristics, various

temperature accuracies have been achieved. Historically the most widely used algorithms were initially developed for the use in metal processing and later were applied to the problem of casing material deformation. However, these algorithms were developed using various assumptions for emissivity that are invalid for deforming casing materials. These assumptions were made to limit the number of necessary spectral images to two. This was done for the same reasons stated earlier; i.e. prior to this research, instrumentation errors made additional spectral measurements ineffective. The theoretical results suggest that if the instrumentation was redesigned so that system errors affected each of the spectral images equally, more spectral measurements could be utilized and thus a highly accurate tool would be produced.

If a single detector array can be used to collect all of the spectral information the common set of optics and support electronics will allow all spectral images to vary with noise in the same manner. Consequently, most of this instrumentation error can be eliminated. While computer rounding errors can also cause a similar problem of weighting an erroneous coefficient with a larger and larger value, if the model used for the emissivity is less than a sixth degree polynomial, the round-off error will not be significant. This research will show that temperature emissivity separation can be performed accurately with a second degree polynomial model for the emissivity.

## **1.2. Separating Temperature and Emissivity from Radiant Power Measurements**

The main problem behind utilizing thermal radiation in making IR pyrometer measurements,<sup>6,7</sup> is in attaining accurate knowledge of: the spectral emissivity of the target, the effects of atmospheric absorption, the transmittance of the optics, and the spectral response of the

detector. Spurious signals, coming from other emitting bodies that lie out of the field of view of the detector, make the measurement even more difficult. The path radiance term is generally small and can thus be ignored. Including all these terms, the basic radiometric equation that maps power to a single detector element is:

$$\Phi = LA\Omega, \quad (1-2)$$

where L is the radiance of the object for a specific temperature, A is the area of the object, and  $\Omega$  is the solid angle subtended by the optics. Taking into account the transmission of the optics and the atmosphere the power on the detector equation can be rewritten in differential form as:

$$d\Phi(\lambda, T, T_s, \theta) = \left[ \frac{c_1}{\lambda^5 \left( e^{\frac{c_2}{\lambda T}} - 1 \right)} \varepsilon(\lambda, T, \theta) + \frac{c_1}{\lambda^5 \left( e^{\frac{c_2}{\lambda T_s}} - 1 \right)} (1 - \varepsilon(\lambda, T, \theta)) \varepsilon_s(\lambda, T_s, \theta) \right] \tau_a(\lambda) \tau_o(\lambda) A_0 d\theta d\lambda, \quad (1-3)$$

where:

$$c_1 = 1.28 \times 10^4 \text{ W } \mu^4 / \text{cm}^2$$

$$c_2 = 1.44 \times 10^4 \mu \text{ K}$$

$T$  = Temperature of target

$T_s$  = Equivalent temperature of the background

$\lambda$  = Wavelength in microns

$\varepsilon(\lambda, T, \theta)$  = Emissivity of target

$\varepsilon_s(\lambda, T_s, \theta)$  = Emissivity of background

$\tau_a$  = Transmission of atmosphere

$\tau_o$  = Transmission of optics

$d\theta$  = Differential solid angle

$d\lambda$  = Differential wavelength

$A_0$  = Area of the object

The second term inside the brackets is due to radiation coming from objects out of the field-of-view of the detector but reflecting off the object of interest. When care is taken in setting up an experiment and the object of interest is hot compared to other objects in the surrounding area, the reflected radiation will be very small and can be left out of the expression.<sup>8</sup> Further simplifying equation 1-3 can be done when emissivity variations across the solid angle are negligible.<sup>9</sup> The emissivity will vary as one minus the reflectivity and it is known that the reflectivity for metals will see very little variation over a wide angle,  $\theta$ .<sup>10</sup> The emissivity dependence with solid angle ( $\theta$ ) can, therefore, be dropped and equation 1-3 can be rewritten as:

$$d\Phi(\lambda, T) = \frac{c_1}{\lambda^5 \left( e^{\frac{c_2}{\lambda T}} - 1 \right)} \varepsilon(\lambda, T) \tau_a(\lambda) \tau_o(\lambda) A_o d\theta d\lambda. \quad (1-4)$$

After calibration, the transmission and detector response terms of equation 1-3 are known and the basic radiometric equation simplifies to two unknowns. The problem of determining the true temperature from passive IR radiation is now coupled only to the uncertainty in predicting emissivity. It is the attempt of this section to give some understanding of the models for emissivity that were developed in the past and substantiate their usage. The discussion will start with a simple model that uses only one color measurement and the section will conclude with a new model developed for the work of this dissertation.

### 1.2.1. Single-Color Pyrometry

The primary assumption behind single-color pyrometers is that the emissivity for the object must be known accurately within the bandwidth of the sensor. After the emissivity is known, the signal at a single detector for an object that fills the instantaneous field of view, can be represented by,

$$\Phi(\lambda, T) = \int_0^\infty \frac{c_1}{\lambda^5 \left( e^{\frac{c_2}{\lambda T}} - 1 \right)} \varepsilon \tau_a(\lambda) \tau_o(\lambda) A_o \Omega d\lambda. \quad (1-5)$$

The limits of the integral have been set to take into account all spectral energy. However, in reality the transmission term will allow only a certain number of spectral components to contribute to the power at a given detector. The temperature can be solved for after the power at a detector is known. First, Equation 1-5 needs some simplification. At high temperatures (above 100C°) the -1 of the denominator is small compared to the  $e^{\frac{c_2}{\lambda T}}$  term and can be dropped. The emissivity's dependence on temperature and wavelength has also been removed because this technique depends on an accurate model of emissivity at the temperature of the object and the wavelength of the pyrometer. Equation 1-5 can then be solved explicitly for T. Depending on the accuracy of measuring the other terms in equation 1-4, reasonably accurate solutions are found for temperature. Since temperature variations affect the incident power as an exponential and the other terms have more linear effects,<sup>11</sup> maximum sensitivity is obtained at the steepest slope of the blackbody distribution curve that is to the right of its peak. Additional sensitivity is obtained by separating the IR energy into two spectral regions and this is the topic to the next section.

### 1.2.2. Dual-Color Pyrometry

Dual-color pyrometers are used when emissivity is not known, but a known relationship exists between the emissivities at any two wavelengths (i.e.  $\varepsilon_{\lambda,1} = f(\varepsilon_{\lambda,2})$  or  $\ln(\varepsilon_{\lambda,1}) = f(\ln(\varepsilon_{\lambda,2}))$ ). Surface characteristics of emissivity vary with many factors (oxidation layer thickness, surface roughness, etc.) and two color pyrometers combine two spectral radiance measurements to arrive at a more accurate temperature estimation. The most commonly used two-wavelength algorithm today is the ratio temperature (RAT) method. The derivation of the RAT algorithm begins with solving for the emissivity at two points, i.e.,

$$\varepsilon_1 = \frac{M_1 \lambda_1^5 e^{\frac{c_2}{\lambda_1 T}}}{c_1}, \quad (1-6)$$

and

$$\varepsilon_2 = \frac{M_2 \lambda_2^5 e^{\frac{c_2}{\lambda_2 T}}}{c_1}, \quad (1-7)$$

Where the M's are the measured values for radiant exitance and the integral has been dropped for simplicity. Assuming the ratio of the two emissivities is a known constant,

$$\frac{\varepsilon_1}{\varepsilon_2} = \frac{c_1}{c_1} \frac{M_1 \lambda_1^5 e^{\frac{c_2}{\lambda_1 T}}}{M_2 \lambda_2^5 e^{\frac{c_2}{\lambda_2 T}}}, \quad (1-8)$$

or

$$\frac{\varepsilon_1}{\varepsilon_2} \frac{c_1}{c_1} \frac{M_2 \lambda_2^5}{M_1 \lambda_1^5} = e^{\frac{c_2}{\lambda_1 T} - \frac{c_2}{\lambda_2 T}}, \quad (1-9)$$

Taking the log of each side and rearranging terms, equation 1-9 becomes

$$\frac{c_2}{T} \left( \frac{1}{\lambda_1} - \frac{1}{\lambda_2} \right) = \ln \left( \frac{c_1}{c_1} \frac{M_2 \lambda_2^5}{M_1 \lambda_1^5} \right) + \ln \left( \frac{\varepsilon_1}{\varepsilon_2} \right), \quad (1-10)$$

or

$$\frac{1}{T} = \frac{\lambda_1 \lambda_2}{c_2 (\lambda_2 - \lambda_1)} \ln \left( \frac{c_1}{c_1} \frac{M_2 \lambda_2^5}{M_1 \lambda_1^5} \right) + \frac{\lambda_1 \lambda_2}{c_2 (\lambda_2 - \lambda_1)} \ln \left( \frac{\varepsilon_1}{\varepsilon_2} \right), \quad (1-11)$$

or

$$\frac{1}{T} = \frac{\lambda_1 \lambda_2}{c_2 (\lambda_2 - \lambda_1)} \left[ \ln \left( \frac{c_1}{M_1 \lambda_1^5} \right) - \ln \left( \frac{c_1}{M_2 \lambda_2^5} \right) \right] + \frac{\lambda_1 \lambda_2}{c_2 (\lambda_2 - \lambda_1)} \ln \left( \frac{\varepsilon_1}{\varepsilon_2} \right). \quad (1-12)$$

The RAT temperature equation is, finally,

$$\frac{1}{T} = \frac{1}{T_r} + \frac{\Lambda_r}{c_2} \ln(\varepsilon_r) . \quad (1-13)$$

where

$$\begin{aligned} \frac{1}{T_r} &= \Lambda_r \left[ \frac{1}{\lambda_1 T_{\lambda_1}} - \frac{1}{\lambda_2 T_{\lambda_2}} \right] \\ \Lambda_r &= \frac{\lambda_1 \lambda_2}{\lambda_2 - \lambda_1} , \\ \varepsilon_r &= \frac{\varepsilon_{\lambda_1}}{\varepsilon_{\lambda_2}} \end{aligned} \quad (1-14)$$

and  $T_{\lambda_1}$  and  $T_{\lambda_2}$  are the brightness temperatures that would be inferred if the emissivity for the target was 1.0. In practice, there are some errors in measurement and compensation must be made for calculated temperature. This relationship is

$$\frac{1}{T_r} = \frac{A}{T_{\lambda_1}} + \frac{B}{T_{\lambda_2}} + C , \quad (1-15)$$

where A and B are dependent on the specific algorithm used<sup>12</sup> and C represents the error term. For the RAT algorithm  $A = \Lambda_r / \lambda_1$  and  $B = -\Lambda_r / \lambda_2$ . This technique works well when the emissivity ratio is constant. When this is not the case, other algorithms are needed for accurate results.

There are two classifications for dual-wavelength algorithms. The first type can be referred to as the exact method. These algorithms require knowledge of how emissivity at one wavelength varies with the emissivity at the second wavelength. The RAT algorithm is an example of this technique. A set of two simultaneous equations, one for each measurement at a given wavelength, can be solved to produce an exact answer if the emissivity relationship, such as in equation 1-13, is known (given no measurement error). More generally

$$dM_{\lambda_1} = \frac{\varepsilon_{\lambda_1} c_1}{\lambda_1^5 \left( e^{c_2/\lambda_1 T} - 1 \right)} d\lambda_1, \quad (1-16)$$

and

$$dM_{\lambda_2} = \frac{\varepsilon_{\lambda_2} c_1}{\lambda_2^5 \left( e^{c_2/\lambda_2 T} - 1 \right)} d\lambda_2, \quad (1-17)$$

can be solved if the  $\varepsilon_{\lambda,1} = f(\varepsilon_{\lambda,2})$  relationship is known (i.e., two equations and two unknowns). If the relationship between the two emissivities is known but fluctuates over time then a second technique can be employed. A least-squares method implemented using multiple measurements over time to reduce the effects of noise. The following table 1-1 gives a listing of the commonly used dual-wavelength algorithms and the models/assumptions used for the emissivity. The models/assumptions have been made with a great deal of knowledge of the surface roughness.

In the measurement of the temperature of casing material the surface roughness of the material is changing due to deformation, changing the relationship between the two emissivities. Consequently, dual color algorithms do not predict temperature accurately. A new model needs to be developed for emissivity that is independent of surface roughness, and only needs wavelength information from an arbitrary metal surface.

Algorithm	Temperature Equation	Models
RAT	$\frac{1}{T} = \frac{1}{T_r} + \frac{\Lambda_r}{c_2} \ln\left(\frac{\varepsilon_1}{\varepsilon_2}\right)$	$\frac{\varepsilon_1}{\varepsilon_2} = \text{constant}$
CC	$\frac{1}{T} = \frac{1}{T_{cc}} + \frac{\Lambda_c}{c_2} \ln(\varepsilon_1 \varepsilon_2)$	$\varepsilon_1 \varepsilon_2 = \text{constant}$
MR	$\frac{1}{T} = \frac{1}{T_{mr}} + E_{mr}$	$\frac{\ln \varepsilon_1}{\ln \varepsilon_2} = \frac{1 - K_f \lambda_2}{1 - K_f \lambda_1}$
WAT	$\frac{1}{T} = \frac{1}{T_{watr}} + E_{watr}$	$\frac{\ln \varepsilon_1}{\ln \varepsilon_2} = \left(\frac{\lambda_1}{\lambda_2}\right)^2$
RWO	$T = T_r + E_{rwo}$	$\frac{\varepsilon_1}{\varepsilon_2} = \text{constant}$
LSR	$T = (1 - x_o)T_r + x_o T_{\lambda_2} + E_{lsr}$	$\frac{\ln \varepsilon_1}{\ln \varepsilon_2} = 1 - \frac{x_o}{1 - x_o} \frac{\lambda_2}{\Lambda_r} \frac{T_{\lambda_2}}{T_r}$
ISR	$\frac{1}{T} = \frac{(1 - y_o)}{T_r} + \frac{y_o}{T_{\lambda_2}} + E_{isr}$	$\frac{\ln \varepsilon_1}{\ln \varepsilon_2} = 1 - \frac{y_o}{1 - y_o} \frac{\lambda_2}{\Lambda_r}$
LAND	$\frac{1}{T} = \frac{1}{T_{\lambda_1}} + C \left( \frac{1}{T_{\lambda_1}} - \frac{1}{T_{\lambda_2}} \right) + E_{land}$	$\frac{\ln \varepsilon_1}{\ln \varepsilon_2} = \frac{C}{1 + c} \frac{\lambda_2}{\lambda_1} + \frac{E_{land} c_2}{(1 + C) \lambda_1}$
MCC	$\frac{1}{T} = \frac{1}{T_{mcc}} + E_{mcc}$	$\frac{\ln \varepsilon_1}{\ln \varepsilon_2} = \frac{1 - K_s \lambda_2}{1 - K_s \lambda_1}$
WWO	$T = T_{wat} + E_{wwo}$	$\frac{\ln \varepsilon_1}{\ln \varepsilon_2} = \left(\frac{\lambda_1}{\lambda_2}\right)^2$
ISS	$\frac{1}{T} = \frac{A}{T_{\lambda_1}} + \frac{B}{T_{\lambda_2}} + B_{iss}$	$\frac{\ln \varepsilon_1}{\ln \varepsilon_2} = \frac{B}{A} \frac{\lambda_2}{\lambda_1} + \frac{E_{iss} c_2}{A \lambda_1}$
HR1	$\frac{1}{T} = \frac{1}{T_{hr1}} + E_{hr1}$	$\frac{\ln \varepsilon_1}{\ln \varepsilon_2} = \frac{\ln(\lambda_1 / a^2 T)}{\ln(\lambda_2 / a^2 T)}$
IT1	$\frac{1}{T} = \frac{1}{T_{it1}} + E_{it1}$	$\frac{\ln \varepsilon_1}{\ln \varepsilon_2} = \frac{T_{\lambda_2}}{T_{\lambda_1}}$

**Table 1-1:** Temperature equations and compensation requirements<sup>13</sup>

### 1.2.3. Multi-Color Pyrometry

When the models for emissivity used to realize a two-color pyrometer are not accurate, a new model needs to be generated and this will require additional colors (spectral regions) to be collected by the IR instrumentation. Knowing the response of each of these spectral regions, a system of equations can be generated. Solving this system of equations will separate the coupled response of temperature and emissivity. A system of equations is constructed from the energy residing in each of the spectral regions of the pyrometer. These equations are,

$$\Phi_i = \int_0^{\infty} \frac{c_1}{\lambda^5 \left( e^{\frac{c_2}{\lambda T}} - 1 \right)} \varepsilon(\lambda) \tau_a(\lambda) \tau_o(\lambda) A_o \Omega d\lambda, \quad \text{for } i=1 \text{ to } n, \quad (1-18)$$

where  $n$  is the number of spectral regions. The area of the object and solid angle is known quantities after system calibration, and can be represented as a single function,  $R_i(\lambda)$ . In addition, after calibration, the transmission terms of equation 1-17 can also be incorporated into the this same function, further simplifying the expression. The power on the detector Equation (1-17) can be rewritten as

$$\Phi_i = \int_0^{\infty} \frac{c_1}{\lambda^5 \left( e^{\frac{c_2}{\lambda T}} - 1 \right)} \varepsilon(\lambda_i) R_i(\lambda) d\lambda, \quad \text{for } i=1 \text{ to } n. \quad (1-19)$$

The first equation ( $i=1$ ) has two unknowns, temperature and emissivity. Each additional equation added for each of the spectral regions,  $i=2,3,\dots$ , introduces one more unknown emissivity with temperature remaining the same in all equations. Consequently the system of equations is always under determined (more unknowns than equations) and some assumptions need to be made about the behavior of emissivity. The typical assumption is that the emissivity follows a  $M^{th}$  degree polynomial with wavelength,

$$\varepsilon(\lambda) = a_{M+1}\lambda^M + a_M\lambda^{M-1} + a_{M-1}\lambda^{M-2} + \dots + a_1. \quad (1-20)$$

There are  $M+1$  unknown coefficients of  $\lambda$  and with the temperature undefined leaves  $M+2$  unknown. Consequently, information regarding the amount of optical energy in  $M+2$  spectral regions is needed to form  $M+2$  equations. There are a number of mathematical techniques that can be used to solve a system of equations where the number of equations is equal to or greater than the number of unknowns. Several techniques will be compared in chapter 2, Emissivity Model Development, Test and Analysis.

### 1.3. Prior Pyrometer Instrumentation

Up to this point, the discussion has been limited to the models/algorithms used to separate temperature effects from emissivity. Now the instrumentation used in the past to collect the spectral data will be detailed. These types of instrumentation, in addition to being inaccurate, are unable to acquire the required spectral information quickly enough to meet the needs of energetic materials pyrometry. In the past several years there have been many attempts to develop fast imaging spectrometers.<sup>14, 15, 16</sup> While each technique has had its strengths, none showed promise to meet the requirements of munition development. Consequently, a large part of this dissertation will discuss the development of a new imaging spectrometer with no moving parts.

Spectrometers requiring moving parts range from a rotating filter wheel to the displacement of a mirror in an interferometer. Most of these systems are not fast enough to be used in actual munition testing, but can be used to validate high-speed instrumentation, as well as a variety of lower speed applications. It is important to understand these systems in order to substantiate the need for alternative instrumentation. There are three techniques used in moving part spectrometers: (1) Moving a series of filters in front of a fixed detector (moving filter wheel); (2) Moving the image over a series of detectors each with its own filter; and (3) Changing the optical path difference of an interferometer. These three techniques will be

discussed to justify why a new technology needed to be developed to meet the requirements in munition testing.

The moving filter wheel spectrometer is probably the most basic and easiest to implement of all of the spectrometer systems.<sup>17</sup> The idea is that a filter can be placed in front of a detector or detector array for which the image of some object is formed. After data is collected for the one filter, a second filter takes its place. Eventually, enough spectral information is collected to characterize a given event. The strength of this approach, as mentioned, is ease of implementation. In addition, the filter responses can be characterized providing accurate filter calibration that does not change over time. This is a good system to use for general characterization for slowly changing events. However, it suffers from the mechanical limitations of rotating a filter wheel or some other mechanical device. After a given detector integration, the filter needs to accelerate and then stop so that the detector can accomplish subsequent integrations. This can take a substantial amount of time, and when the spectral radiance of the event is changing, the instantaneous radiant exitance characteristics can't be evaluated.

Some of this limitation can be reduced by replacing the discrete filter wheel by a circular variable filter wheel and rotating with a constant angular velocity<sup>18</sup>. If the filter is in collimated space, then the overall shift of the pass band will move a reasonable amount between each subsequent detector readout. The limitation changes from how fast the filter wheel can be rotated, stopped, rotated, stopped, to a limitation in the speed of the readout for the detector. This can mean substantial increase to the overall speed of the system and, consequently, the speed of collection of multiple spectral regions. If the spectral separation is not significant then the system of equations will be highly singular mandating the collection of more spectral regions than the system of equations indicates (i.e.,  $M+2$  equations  $M+2$  unknowns). Inherently, in these types of systems the uncertainty in the variable filter wheel position, and consequently, the filter pass band, creates an uncertainty in the amount of collected optical energy. In high-speed events this uncertainty becomes unreasonable for the accurate reconstruction of the temperature of the subject event. Even with a moderately accurate emissivity model, the reconstruction of temperature inevitably becomes a limitation of the instrumentation collecting the spectral energy. Hence, the filter wheel approach is not the instrumentation of choice for high speed events.

Instead of moving the filter as described above, the image may be moved across a series of detectors, each with its own fixed pass band, support electronics and imaging optics. This system is typically referred to as a framing camera.<sup>19</sup> The approach invariably requires the use of a rotating mirror in a pupil plane of the optical system. Scanning in the pupil plane avoids the overlap of spectral energy from detector array to detector array and singularity of the system of equations can be circumvented. This type of device is inherently faster than the aforementioned technique because the scanning mechanism is lighter and can be rotated faster. While this system is faster than the rotating filter approach, the geometrical setup (separation between elements) limits the effective  $F/\#$  to a minimum of about 20 or higher. With the knowledge that the radiometry follows a dependence proportional to  $\frac{1}{F/\#^2}$  it can be seen that the efficiency of this type of system is at least two orders of magnitude less than a typical  $F/2$  system that could be implemented in a single color pyrometer. Consequently, in order to get the same amount of optical energy onto the detector array as for the single color system, the integration time for the framing camera must be increased by two orders of magnitude. This makes the system too slow for use in the energetic environment.

Instead of moving the filter or the image across a series of detector arrays, a Fabry-Perot can be scanned through wavelength. A Fabry-Perot type spectrometer uses two reflective surfaces to form a resonator cavity<sup>20</sup>. Frequencies of light that are tuned to that cavity are allowed to pass more freely due to interference losses (at each of the two surfaces) from the multiple reflections of a common beam of light. When the frequency of light experiences an even number of wavelengths in the cavity, the losses will be minimized. The pass band of the cavity can be scanned by moving one of the mirrors. A detector is then used to obtain the spectra for the light entering the system. However, either this type of system is still slowed by the readout of the detector or the scan of the mirror since the radiance information for each of the spectral regions is not collected concurrently.

Instead of using an interferometer to pass only a small portion of the wavefront, one may choose to delay a portion of the optical energy and interfere it with the original signal<sup>21</sup>. With no optical path difference between the two arms of an interferometer, an unaltered signal would be acquired at the detector. As one of the mirrors is scanned, the detector will respond in

accordance to the partial coherence of the incoming light. After scan of the mirror, the Van Cittert-Zernike<sup>22</sup> theorem can be employed to reconstruct spectral content. Simply stated, the detector data will be a Fourier transform of the spectrum. This technique is referred to as a Fourier transform spectrometer (FTS).<sup>23</sup> The strength of this method is that it has high spectral resolution. However, FTS suffers from the same problem as the Fabry-Perot interferometer taking a significant amount of time to move the scan mirror or readout the detector.

Since the energetic environment requires the acquisition of data in a few microseconds the above techniques are all too slow to be used. It becomes apparent that a snapshot spectrometer is required. There are two ways to construct an imaging snapshot spectrometer. The image can be separated into multiple images on a focal plane, each at a different color, or the image can be diffracted over the focal plane. The multiple diffractive orders can be used to reconstruct the image at some later point.<sup>24</sup> While both of these techniques have shown promise to solve the energetic materials pyrometry problem, the reconstruction algorithm needed when the image is diffracted over the focal plane is computationally cumbersome, and takes tremendous amounts of time to process even small images (10 pixels by 10 pixels). In addition, since the diffracted orders will not fill the detector array evenly the focal plane between the diffractive orders is wasted. Consequently, the method of choice is to separate spectral energy into multiple images on a focal plane concurrently. After looking at the types of systems that separate images onto a single detector array, or multiple arrays, it quickly became obvious that advantages in new focal plane technology could be exploited. A new instrument was developed for use on the casing material's found in munition testing.

## **2. Emissivity Model development, Test and Analysis**

This chapter will discuss the development of a model for emissivity of metals that depends only on the spectral form of IR radiation. This model will be validated for accuracy using special FTS instrumentation. In addition, the algorithms used to find the temperature and emissivity from multi-spectral measurements will be discussed. However, before the model for emissivity is developed, the thermal equilibrium assumption needs to be validated to show that even if the temperature is changing, the spectral behavior for the radiation will still follow a blackbody distribution.

### **2.1. Validation of Thermal Equilibrium Assumption**

Light emitted from solids under conditions of thermal equilibrium and without any other external sources, is known as thermal light.<sup>25</sup> The Planck blackbody radiation law uses thermal equilibrium statistics to derive the ideal wavelength dependent IR spectrum. However, the surface temperature of energetic materials may be highly dynamic and the assumption of thermal equilibrium may not be correct. An evaluation is needed to show how much the temperature can change during a given time interval before the IR radiation spectrum deviates from the ideal blackbody radiation law. This evaluation can start by analyzing a material that has two energy states.

Consider a cavity of unit volume whose walls contain many atoms of two energy states separated by an energy difference,  $h\nu$ . The cavity will support broadband radiation<sup>26</sup>. Now let  $N_1$  and  $N_2$  represent the number of atoms, per unit volume, occupying energy levels one and two. Spontaneous emission creates radiation in the cavity, assuming that at least one atom is at energy level two. Subsequently, absorption and stimulated emission can occur. These three processes exist in equilibrium when steady state is reached. This derivation will first consider the spontaneous emission rate and then move on to absorption and stimulated emission.

The probability that an atom in the upper energy state undergoes spontaneous emission into any of the modes within the time interval  $\Delta t$  is  $P_{sp} \Delta t = \Delta t / t_{sp}$ , where  $t_{sp}$  is the spontaneous emission time. There are  $N_2$  such atoms and the average number of photons emitted in  $\Delta t$  seconds is therefore  $N_2 \Delta t / t_{sp}$ . This is also the number of atoms that leave level 2 during the time interval. Consequently, the rate that atoms increase in level 2, due to spontaneous emission, is given by,

$$\frac{dN_2}{dt} = -\frac{N_2}{t_{sp}}. \quad (2-1)$$

The solution of this differential equation is an exponential decaying function and a function of initial state  $N_{0_2}$  at time zero;

$$N_2 = N_{0_2} e^{\left(\frac{-t}{t_{sp}}\right)}. \quad (2-2)$$

In the presence of radiation, absorption and stimulated emission will occur. This changes the populations of  $N_1$  and  $N_2$ . Since there are  $N_1$  atoms in level one capable of absorbing, the rate of increase of the population of atoms in the upper level, due to absorption, is,

$$\frac{dN_2}{dt} = \frac{N_1 \bar{n}}{t_{sp}}, \quad (2-3)$$

where  $\bar{n}$  is the average number of photons per radiation mode. In a similar way, the stimulated emission can be written as,

$$\frac{dN_2}{dt} = -\frac{N_2 \bar{n}}{t_{sp}}. \quad (2-4)$$

Equation 2-4 shows that the absorption and spontaneous emission rates are proportional to the average number of photons in each mode. Summing the three processes we can now write the rate equation for the overall process as,

$$\frac{dN_2}{dt} = -\frac{N_2}{t_{sp}} + \frac{N_1 \bar{n}}{t_{sp}} - \frac{N_2 \bar{n}}{t_{sp}}. \quad (2-5)$$

Notice that equation 2-5 does not include transitions to other than the two levels. However, adding more levels is a trivial extension when the system is in thermal equilibrium.<sup>27</sup> Thermal equilibrium will first be assumed and then the temperature will be allowed to change to determine if the results change. In steady state, the rate of change between the levels will be zero,  $\frac{dN_2}{dt} = 0$ . Consequently, the ratio of the populations of the two states is

$$\frac{N_2}{N_1} = \frac{\bar{n}}{1 + \bar{n}} = \frac{1}{\frac{1}{\bar{n}} + 1}. \quad (2-6)$$

If the system is in thermal equilibrium, the populations obey a Boltzman distribution, i.e.,

$$\frac{N_2}{N_1} = e^{-\left(\frac{h\nu}{k_B T}\right)}, \quad (2-7)$$

and the radiation mode distribution is

$$\bar{n} = \frac{1}{e^{\left(\frac{h\nu}{k_B T}\right)} - 1}. \quad (2-8)$$

The relation above was derived under the assumption of thermal equilibrium, but is this assumption a good one? If the temperature changes from  $T_1$  to  $T_2$  during the time interval,  $\Delta t$ , the change in the populations will be related as:

$$\Delta N_2 = -\Delta N_1. \quad (2-9)$$

If ten atoms move to level two, then, as a consequence, level one loses ten atoms. The change in the populations can also be written as:

$$\Delta N_2 = \left[ \frac{1}{\frac{1}{\bar{n}} + 1} N_1 \right]_{T_2} - \left[ \frac{1}{\frac{1}{\bar{n}} + 1} N_1 \right]_{T_1}. \quad (2-10)$$

$\bar{n}$  is much smaller than one and the one in the denominator can, therefore, be dropped. Equation 2-10 can be rewritten as:

$$\Delta N_2 \approx [\bar{n} N_1]_{T=600} - [\bar{n} N_1]_{T=500}. \quad (2-11)$$

Equation 2-11 cannot be solved without knowledge of the population of level one; however, an approximation for  $\Delta N_2$  can be made. In equation 2-11 the first term is much larger than the second term and they are both positive. Dropping the second term,

$$\Delta N_2 \approx [\bar{n} N_1]_{T=600} \approx 3 \times 10^{-4} N_1. \quad (2-12)$$

We can also write the population of level two in terms of level one as

$$N_2 \approx [\bar{n} N_1]_{T=500} \approx 5 \times 10^{-5} N_1,$$

and

$$\Delta N_2 \approx 10 N_2. \quad (2-13)$$

Consequently, if the observation time is one microsecond and the relaxation time is  $10^{-14}$  seconds then the  $dN_2/dt$  term is negligible, i.e.,

$$\frac{dN_2}{dt} = \frac{\Delta N_2}{\Delta t} = \frac{10N_2}{\Delta t} \approx 10^7 N_2. \quad (2-14)$$

Equation 2-5 can be rewritten in terms of the ratio of the two populations as:

$$\frac{N_2}{N_1} = \frac{\bar{n}}{t_{sp} 10^7 + 1 + \bar{n}}. \quad (2-15)$$

The  $t_{sp} 10^7$  term is associated with the changing population term and is very small compared to 1.

Therefore,

$$\frac{dN_2}{dt} \approx 0, \quad (2-16)$$

and the steady state assumption holds true even when temperature is changing. It appears that the blackbody radiation law will provide a good model for the temperature dependent spectral radiation until the integration time approaches the relaxation time, at least for the given 100° temperature change.

## 2.2. Emissivity Behavior For Ideal Metal

The manner by which that an ideal solid generates an IR spectrum has been discussed and now attention is diverted to the characterization of a metal's absorption spectrum and, its ideal emissivity. The phenomenon of the bulk material's IR absorption and emission spectra needs more detail. This is done by modeling the metal as an electron plasma with characteristic relaxation time and effective mass. The next step will be to consider how the surface affects radiation into free space. The surface will alter the total amount of energy at a given wavelength that is allowed to escape from the bulk material. Contributing to this effect is Fresnel reflection, surface roughness causing diffraction, surface roughness altering refraction and oxidation or other surface deposits. The free electron model will be discussed first.



### 2.2.1. Free Electron Model

When in equilibrium, according to Kirchoff's law, the absorption of a material is equivalent to the emissivity. Consequently, if absorption characteristics of a material can be determined, the emissivity characteristics will be known. Since much of the munition application is considering the optical properties of heated metals, the derivation will start with obtaining the absorption relationship for a simple metal.

The earliest attempts to predict the optical properties of metals were made by Lorentz and Drude.<sup>28</sup> They assumed the metal to contain electrons that were essentially free to move under the influence of the electric field induced by the incident electromagnetic wave. These free electrons are the valence electrons in the outer shell of the atoms constituting the metal. When an electromagnetic wave is incident upon its surface, an oscillating electric field of angular frequency  $\omega$  is induced parallel to the surface in the metal. The free electrons will oscillate under the influence of this field at the frequency of the incident wave. Since the electrons are moved by the electric field they must absorb some of its energy. The absorption of a material can be derived from its dielectric function. In turn, the dielectric function can be derived from a material's polarization defined by the density of dipole moments. To derive the dipole moment of the free electrons it is first assumed that the electrons respond to an electric field,  $E(t)$ , polarized in the x direction. The equations of motion for each electron in the field, using Newton's second law, are written as

$$m_e \frac{d^2 x(t)}{dt^2} + \frac{m_e}{\tau} \frac{dx(t)}{dt} = -eE(t), \quad (2-17)$$

where,  $x(t)$  is the electron displacement from equilibrium,  $\tau$  is the electron relaxation time and  $m_e$  is the effective mass of an electron. Note that the motion of the nucleus has been neglected in Equation 2-17. This is known as the dipole approximation<sup>29</sup>. The second term of equation 2-17

represents the damping due to collisions with ions. Note that, because the electrons in a metal are free to conduct, there is no restoring force in Equation 2-17.

Assuming a single wavelength interacting at frequency  $\omega$ , the time dependent field is

$$E(t) \cong E_0 e^{-i\omega t} \quad (2-18)$$

Accordingly, the position of the electron will follow the field oscillation and can be written as:

$$x(t) \cong x_0 e^{-i\omega t} \quad (2-19)$$

Substituting Eq. 2-18 and Eq. 2-19 into Eq. 2-17 and dividing both sides by  $e^{-i\omega t}$ , the equation of motion becomes

$$-m_e \omega^2 x_0 - m_e \frac{i\omega}{\tau} x_0 = -e E_0 \quad (2-20)$$

or

$$x_0 = \frac{e\tau}{m_e \omega} E_0 \frac{\omega\tau - i}{\omega^2 \tau^2 + 1} \quad (2-21)$$

This is the solution to the differential equation of motion. The polarization density,  $P_c$ , of the conducting electrons is the dipole moment,  $-ex(t)$ , multiplied by the electron density,  $n_e$ , and is given by

$$P_c = -n_e ex(t) = -\frac{ne^2\tau}{m_e \omega} E(t) \frac{\omega\tau - i}{\omega^2 \tau^2 + 1} \quad (2-22)$$

The polarization due to the electrons is accompanied by the polarization induced by the applied electric field,  $P_b$ , which can be thought of as the background polarization.  $P_b$  is due to the motion of bound particles, such as inner-shell electrons about their equilibrium position. The total polarization is the summation of the electronic and background terms, or,

$$P = P_c + P_b. \quad (2-23)$$

The optical susceptibility of a material is defined as,

$$\chi(\omega) = \frac{P(\omega)}{E(\omega)}. \quad (2-24)$$

The displacement field, D, can be written in terms of the electric field and the susceptibility,

$$D = E + 4\pi P = E[1 + 4\pi\chi(\omega)] . \quad (2-25)$$

In addition, the relationship between the displacement electric field and the dielectric function,

$$D = \epsilon(\omega)E, \quad (2-26)$$

can be used to obtain the relationship between susceptibility and dielectric function,

$$\epsilon(\omega) = 1 + 4\pi\chi(\omega). \quad (2-27)$$

Thus, the dielectric function can be represented in terms of polarization density and electric field:

$$\begin{aligned} \epsilon(\omega) &= 1 + 4\pi \frac{P_b}{E} + 4\pi \frac{P_c}{E} \\ &= 1 + 4\pi \frac{P_b}{E} - \frac{4\pi n e^2 \tau}{m_e \omega} \frac{\omega \tau - i}{\omega^2 \tau^2 + 1} \end{aligned} \quad (2-28)$$

$$= \epsilon'(\omega) + i \epsilon''(\omega).$$

The imaginary and real parts will be used to compute the index of refraction and absorption respectively. At high frequencies, the last term containing  $P_c$  is negligible<sup>30</sup> and the remaining terms fold into the high frequency term,  $\epsilon_\infty$ . Equation 2-28 can be rewritten as

$$\epsilon(\omega) = \epsilon_\infty - \frac{4\pi n e^2 \tau}{m_e \omega} \frac{\omega \tau - i}{\omega^2 \tau^2 + 1}. \quad (2-29)$$

This formula is known as the Drude oscillator model for the dielectric function and can also be written as

$$\epsilon(\omega) = \epsilon'_\infty + \epsilon''_\infty - \frac{4\pi n e^2 \tau^2}{m_e} \frac{1}{\omega^2 \tau^2 + 1} + i \frac{4\pi n e^2 \tau}{m_e \omega} \frac{1}{\omega^2 \tau^2 + 1}. \quad (2-30)$$

Now the coefficient for absorption in terms of dielectric function can be solved. This relationship is derived in many texts<sup>31</sup> and is

$$\alpha(\omega) = \frac{\omega}{c n(\omega)} \epsilon''(\omega), \quad (2-31)$$

where

$$n(\omega) = \sqrt{\frac{1}{2} \left[ \epsilon' + \sqrt{(\epsilon')^2 + (\epsilon'')^2} \right]}. \quad (2-32)$$

and  $c$  is the speed of light in a vacuum. Substituting equations 2-30 and 2-32 into equation 2-31 and arranging terms we have

$$\alpha(\omega) = \frac{\sqrt{2} \omega \epsilon''_\infty - \frac{\sqrt{2} \omega 4\pi n e^2 \tau}{m_e \omega} \frac{1}{\omega^2 \tau^2 + 1}}{c \sqrt{\epsilon_\infty - \frac{4\pi n e^2 \tau^2}{m_e} \frac{1}{\omega^2 \tau^2 + 1} + \left( \epsilon'_\infty - \frac{4\pi n e^2 \tau^2}{m_e} \frac{1}{\omega^2 \tau^2 + 1} \right)^2 + \left( \epsilon''_\infty - \frac{4\pi n e^2 \tau}{m_e \omega} \frac{1}{\omega^2 \tau^2 + 1} \right)^2}}. \quad (2-33)$$

Given this complex equation it seems rather a formidable task to solve for the absorption. There are several material contestants that, in all likelihood, will be unknown. There are five unknown constants in the system: . Since emissivity is equal to absorption, an optical pyrometer will be required to resolve six spectral regions. As was discussed in the last chapter a system of equations can then be solved to determine the five unknown constants and temperature.

The six equations made by the six-color pyrometer are nonlinear and require a nonlinear optimization technique, such as that proposed by Levenberg and Marquardt. These types of algorithms tend to take a long time to optimize and often become caught in local minimums and the global solution is not always found. However, some simplifications can be made for our application. The  $\epsilon_\infty$  term is due to the displacement of bound electrons, and for metals, can be assumed to be unity. Therefore,

$$\alpha(\omega) = \frac{\frac{\sqrt{2}\omega 4\pi n e^2 \tau}{m_e \omega} \frac{1}{\omega^2 \tau^2 + 1}}{c \sqrt{1 - \frac{4\pi n e^2 \tau^2}{m_e} \frac{1}{\omega^2 \tau^2 + 1} + \sqrt{\left(1 - \frac{4\pi n e^2 \tau^2}{m_e} \frac{1}{\omega^2 \tau^2 + 1}\right)^2 + \left(\frac{4\pi n e^2 \tau}{m_e \omega} \frac{1}{\omega^2 \tau^2 + 1}\right)^2}}}, \quad (2-34)$$

where the  $\frac{4\pi n e^2}{m_e}$  term is known as the plasma frequency. Equation 2-34 takes the form

$$\alpha(\omega) = \frac{\frac{\sqrt{2}}{c\tau} A}{\sqrt{1 - A + \sqrt{(1 - A)^2 + \left(\frac{A}{\omega\tau}\right)^2}}}, \quad (2-35)$$

where

$$A = \frac{4\pi n e^2 \tau^2}{m_e} \frac{1}{\omega^2 \tau^2 + 1}. \quad (2-36)$$

Conductivity measurements have shown that the relaxation time for metals is on the order of  $10^{-14}$  seconds<sup>32</sup>. Because our sensor is operating between 3 and 5  $\mu\text{m}$ ,  $\tau^2 \omega^2 \geq 36$  and  $\left(\frac{A}{\omega\tau}\right)^2$  is

small, as compared to the  $(1-A)^2$  term, and can be left out of the expression. Equation 2-35 becomes

$$\alpha(\omega) = \frac{\frac{1}{c\tau} A}{\sqrt{1-A}}. \quad (2-37)$$

If the denominator is expanded as a binomial series, equation 2-37 becomes

$$\alpha(\omega) = \frac{1}{c\tau} A \left[ \frac{1}{\sqrt{A}} - \frac{1}{2} \frac{1}{\sqrt[3]{A}} - \frac{3}{8} \frac{1}{\sqrt[5]{A}} \dots \right]. \quad (2-38)$$

For metals, the magnitude of the refractive index in the denominator is large. As a consequence, the higher-order terms are small and can be left out of Equation 2-38. The equation simplifies to

$$\alpha(\omega) = \frac{\frac{1}{c\tau} A}{\sqrt{A}} = \frac{1}{c\tau} \sqrt{A}. \quad (2-39)$$

If, for instance, the refractive index were to have a value of 5,  $A=26$ . This would yield a value for the approximated absorption of  $\frac{1}{c\tau} 5.1$ , which is within 2% of the unapproximated value of  $\frac{1}{c\tau} 5.2$ . Using the fact that  $\omega^2 \tau^2$  is large compared to 1, equation 2-39 can be rewritten as

$$\alpha(\omega) = \sqrt{\frac{4\pi m e^2}{c^2 \tau^3 m_e}} \frac{1}{\omega} = \sqrt{\frac{\omega_p^2}{c^2 \tau^3}} \frac{1}{\omega} = \sqrt{\frac{\omega_p^2}{c^2 \tau^3}} \frac{\lambda}{2\pi c}. \quad (2-40)$$

Therefore, a first-degree polynomial should provide a good model for our calculations in temperature emissivity decoupling. There are no constant or squared terms in equation 2-40 and experimental results in the past have shown emissivity will depend on more than just the linear

wavelength term.<sup>33</sup> This additional wavelength dependency is shown when the surface is included in the evaluation of how a material generates an IR spectrum.

### **2.2.2. Effects of Surface on Emissivity**

If a piece of polished aluminum, or any metal, is roughened with sand paper the reflectivity decreases; consequently, emissivity increases. In addition, other surface features, such as oxidation or oily residue left behind during processing can also affect spectral emissions. In this section, the contribution of the surface effect will be discussed, and the emissivity model will be modified to incorporate these considerations.

#### **2.2.2.1. Fresnel Reflection at Surface Boundary**

The characteristic energy modes that are available for radiation are known from the Planck radiation law and the method by which energy is reflected back into the bulk material by the boundary needs to be defined. The three fields of concern are the incident field,  $E_i$ , the reflected field,  $E_r$ , and the transmitted field,  $E_t$ , represented in Figure 3.1.

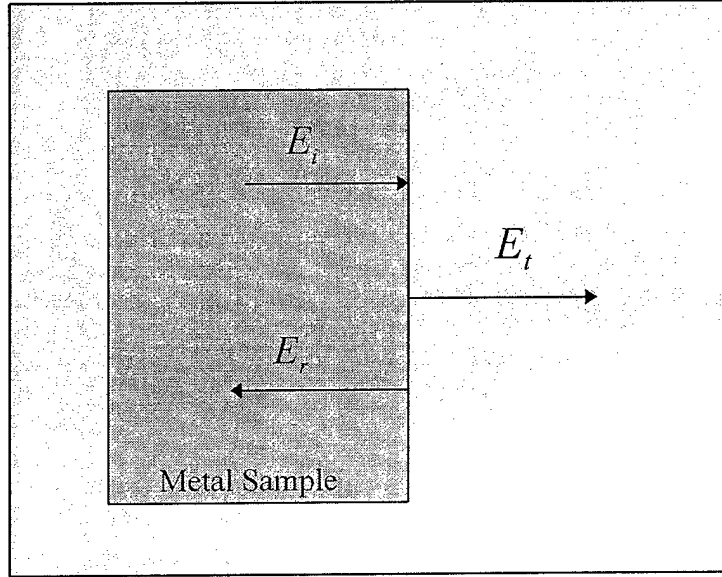


**Figure 2-1:** Surface fields of a metal sample

The E and H fields for the system are<sup>34</sup>:

$$\begin{aligned}
 E_i &= E_{i_0} e^{i\omega \left( \frac{\sqrt{\epsilon}}{c} z - t \right) \hat{x}}, & H_i &= H_{i_0} e^{i\omega \left( \frac{\sqrt{\epsilon}}{c} z - t \right) \hat{y}} \\
 E_r &= E_{r_0} e^{i\omega \left( \frac{\sqrt{\epsilon}}{c} z + t \right) \hat{x}}, & H_r &= H_{r_0} e^{i\omega \left( \frac{\sqrt{\epsilon}}{c} z + t \right) \hat{y}} \\
 E_t &= E_{t_0} e^{i\omega \left( \frac{\sqrt{\epsilon}}{c} z - t \right) \hat{x}}, & H_t &= H_{t_0} e^{i\omega \left( \frac{\sqrt{\epsilon}}{c} z - t \right) \hat{y}}
 \end{aligned} \tag{2-41}$$

Maxwell's third equation can now be used to write

$$\begin{aligned}
 \bar{\nabla} \times \bar{E} &= \left( \frac{dE_z}{dy} - \frac{dE_y}{dz} \right) \hat{x} + \left( \frac{dE_x}{dz} - \frac{dE_z}{dx} \right) \hat{y} + \left( \frac{dE_y}{dx} - \frac{dE_x}{dy} \right) \hat{z} = \\
 -\frac{1}{c} \frac{d\bar{H}}{dt} &= H_{i_0} i\omega e^{i\omega \left( \frac{\sqrt{\epsilon}}{c} z - t \right) \hat{y}}, \text{ or } H_{t_0} i\omega e^{i\omega \left( \frac{\sqrt{\epsilon}}{c} z - t \right) \hat{y}}, \text{ or } H_{r_0} i\omega e^{i\omega \left( \frac{\sqrt{\epsilon}}{c} z + t \right) \hat{y}}.
 \end{aligned} \tag{2-42}$$

Canceling the terms that are zero, Equation 2-42 becomes

$$E_{i_0 \text{ or } t_0} \frac{i\omega}{c} \sqrt{\epsilon} e^{i\omega \left( \frac{\sqrt{\epsilon}}{c} z - t \right) \hat{x}} = H_{i_0 \text{ or } t_0} i\omega e^{i\omega \left( \frac{\sqrt{\epsilon}}{c} z - t \right) \hat{y}}, \quad (2-43)$$

hence,

$$H_{i_0 \text{ or } t_0} = \frac{\sqrt{\epsilon}}{c} E_{i_0 \text{ or } t_0}. \quad (2-44)$$

For the reflection component, from Equation 2-45, there is a sign change on  $t$ , consequently,

$$H_r = -\frac{\sqrt{\epsilon}}{c} E_r. \quad (2-45)$$

Now the boundary conditions need to be incorporated. The tangential component will be continuous at the boundary, e.g.,

$$E_{i0} + E_{r0} = E_{t0} \quad \text{and} \quad H_{i0} + H_{r0} = H_{t0}, \quad (2-46)$$

$$\frac{\sqrt{\epsilon}}{c} E_{i0} + \frac{\sqrt{\epsilon}}{c} E_{r0} = \frac{\sqrt{\epsilon_0}}{c} E_{t0}, \quad (2-47)$$

$$\frac{\sqrt{\epsilon}}{c} (E_{i0} - E_{r0}) = \frac{\sqrt{\epsilon_0}}{c} (E_{t0} + E_{r0}), \quad (2-48)$$

the transmitted wave is in free space, therefore  $\epsilon_0 = 1$  and Eq. 2-52 becomes

$$E_{r0} (\sqrt{\epsilon} - 1) = E_{i0} (\sqrt{\epsilon} + 1), \quad (2-49)$$

or

$$\frac{E_r}{E_i} = \frac{\sqrt{\epsilon} - 1}{\sqrt{\epsilon} + 1}, \quad (2-50)$$

where

$$\epsilon = \epsilon' + i \epsilon''. \quad (2-51)$$

However, since  $\tau^2 \omega^2 \geq 36$ , the thermal energy lies in the high frequency regime. Consequently, the imaginary part of the dielectric function is small compared to the real part and can be neglected<sup>35</sup>. The reflectivity can now be written as

$$r = \frac{E_{r0}}{E_{i0}} = \frac{\sqrt{\epsilon'} - 1}{\sqrt{\epsilon'} + 1} = \frac{1 - \frac{1}{\sqrt{\epsilon'}}}{1 + \frac{1}{\sqrt{\epsilon'}}}, \quad (2-52)$$

where

$$\sqrt{\epsilon'} = \sqrt{1 - \frac{\omega_p^2}{\omega^2}} = \sqrt{-\frac{\omega_p^2}{\omega^2}} = \frac{\omega_p}{\omega}. \quad (2-53)$$

Equation 2-57 can also be written in terms of the transmission of the surface. The transmission defines the amount of energy that escapes the surface and radiates into free space.

$$t = 1 - \frac{E_{r0}}{E_{i0}} = \frac{1 + \frac{1}{\sqrt{\epsilon'}}}{1 + \frac{1}{\sqrt{\epsilon'}}} - \frac{1 - \frac{1}{\sqrt{\epsilon'}}}{1 + \frac{1}{\sqrt{\epsilon'}}} = \frac{2}{1 + \frac{1}{\sqrt{\epsilon'}}}. \quad (2-54)$$

The  $\omega_p$  refers to the plasma frequency introduced earlier. The plasma frequency is typical in the ultraviolet<sup>36</sup>; consequently, for IR radiation the real part of the dielectric function is negative. Since the IR frequencies of interest are well below the plasma frequency the binomial approximation can be used to simplify Equation 2-58.

$$t = \frac{2}{\sqrt{\epsilon'}} \left( 1 - \frac{1}{\sqrt{\epsilon'}} \right) = \frac{2}{\sqrt{\epsilon'}} - \frac{2}{\epsilon'}. \quad (2-55)$$

The second term of this expression can be dropped because it is very small compared to the first. The transmission then becomes

$$t(\omega) = \frac{2}{\sqrt{1 - \frac{\omega_p^2}{\omega^2}}} \approx 2 \frac{\omega}{\omega_p}, \quad (2-56)$$

where

$$\frac{\omega_p}{\omega} > 1 \text{ and } \frac{\omega_p^2}{\omega^2} \gg 1. \quad (2-57)$$

Transmission is the square of transmissivity, hence

$$T(\omega) = t^2 = 4 \frac{\omega^2}{\omega_p^2}. \quad (2-58)$$

Rewriting in terms of wavelength

$$T(\lambda) = \frac{16\pi^2 c^2}{\omega_p \lambda^2}. \quad (2-59)$$

This model needs to be taken one step further in the evaluation of other surface effects. For the model to be accurate, the effects of scratches and grain structure of the material need to be included.

#### **2.2.2.2.Surface Topography**

The published literature on the emissivity of metal surfaces largely ignores the wavelength dependent effects of diffraction or scatter. Diffraction is caused, in part, by surface topography errors that are induced by the manner in which the surface was fabricated or prepared. Surface topography, as well as the inherent crystalline grain boundary structure of the metal surface, causes emitted energy to diffract through the surface of a material. For many years, the published literature on the diffraction theory of scatter has treated surface errors by representing them as a

summation of sinusoidal gratings of varying spatial frequencies. Each component sinusoidal grating causes a single wavelength to diffract into an angle that is not predicted by Snell's Law or the Fresnel equations. This angular dependence, however, can be predicted by using the grating equation:

$$\sin \theta - \sin \theta_i = \frac{m\lambda}{d} \quad (2-60)$$

When using an optical system to measure emissivity, the solid angle subtended by the optical system dictates which diffracted angles can be collected. Since the desired result is emissivity as a function of wavelength, and not as function of angle, it is more appropriate to use the grating equation to see what wavelengths will be collected for a fixed range of scattering angles. Thus, the angular dependence of the diffracted energy can be rewritten with a wavelength dependency.

It has been shown by DeWitt<sup>37</sup> that when a metal surface is systematically roughened with sandpaper, the spectral characteristics of its measured emissivity will change. This emissivity change is a direct representation of the change in the nature of the energy that escapes from the body of the material and into free-space. One possible explanation for this spectral change in emissivity can be attributed to the characteristics of the surface, where optical energy is coupling through the surface by diffraction. The results of Dewitt's wavelength dependent emissivity can be fit by a multiple order polynomial:

$$\varepsilon(\lambda) = A\lambda^M + B\lambda^{M-1} + C\lambda^{M-2} + \dots \quad (2-61)$$

With a detailed analysis of the features present on the surface of the material, the polynomial coefficients ( $A, B, C, \dots$ ) can be found.

A detailed analysis of the diffraction related emissivity is beyond the scope of this dissertation. However, the general approach should be outlined. First, the statistics of the surface topography must be determined. The topography can then be broken down into its fundamental sinusoidal components. Each of the components can then be treated separately as a single

diffraction grating, and the effects of all the sinusoidal gratings can then be summed to determine the total diffraction related emissivity. This effect can then be added to the Fresnel and bulk-material effects to determine the total emissivity.

### **2.2.2.3.Surface Chemistry**

As mentioned earlier, a real metal surface unavoidably carries some film of one type or another, and this affects how the IR energy escapes the bulk material. In the machining of an aluminum part, for instance, oils and other deposits are left behind. Often, the deposits are oxides of the base material, and the characterization is difficult. The layer is a mixture of several different chemical species (metal atoms, oxygen ions, and one or more metal ions), making the interface of the base metal rough. In addition, oxides form on the surface in accordance with the atmospheric conditions, surface topography, temperature, and grain structure. The growth of oxides on a surface is not fully understood, however; the general scenario is a roughening of the surface, the effect of which was presented in the last section. The assumption made here is that the bound states associated with the oxides do not contribute significantly to IR radiation.<sup>38</sup> This is a good assumption as long as the bound electrons are held tightly, as in high-energy interactions.

The coatings of oxide films as well as other material films can have a significant effect on the thermal emissions from a surface. If the consideration can be restricted to oxides, the evaluation becomes simplified to a changing in the roughness of the surface. The objects used in the testing of the above theoretical results were prepared carefully to limit the surface chemistry to only oxidation formed on the surface. In this way the effects of emissivity could be validated and tied directly to the free electrons, Fresnel reflections, and surface topography of the test object.

### 2.3. The Overall Emissivity Model

It has been shown that the bulk material and Fresnel reflections at the boundary have a wavelength dependent effect on the emissivity. However, the true behavior of emissivity can only be theoretically determined if the surface features causing diffraction are known. The total emissivity is a compilation of Equations 2-40, 2-59 and 2-60. Multiplying these three equations we have.

$$\varepsilon(\lambda) = \sqrt{\frac{\omega_p^2}{c^2 \tau_e^3}} \frac{\lambda}{2\pi c} \frac{16\pi^2 c^2}{\omega_p \lambda^2} (A\lambda^M + B\lambda^{M-1} + C\lambda^{M-2} + \dots), \quad (2-62)$$

If the emissivity model for diffraction follows a second order polynomial we have

$$\varepsilon(\lambda) = \sqrt{\frac{\omega_p^2}{c^2 \tau_e^3}} \frac{\lambda}{2\pi c} \frac{16C\pi^2 c^2}{\omega_p} \lambda^{-1} + \sqrt{\frac{\omega_p^2}{c^2 \tau_e^3}} \frac{\lambda}{2\pi c} \frac{16A\pi^2 c^2}{\omega_p} \lambda + \sqrt{\frac{\omega_p^2}{c^2 \tau_e^3}} \frac{\lambda}{2\pi c} \frac{16B\pi^2 c^2}{\omega_p}, \quad (2-63)$$

which is in the form of

$$\varepsilon(\lambda) = D\lambda^{-1} + E\lambda + F. \quad (2-64)$$

The  $\lambda^{-1}$  can be represented as a polynomial by using a Taylor expansion. Expanding around  $\lambda=4$  microns we have

$$\begin{aligned} \lambda^{-1} &= \frac{1}{4} - (\lambda - 4) \frac{1}{16} + (\lambda - 4)^2 \frac{1}{64} - (\lambda - 4)^3 \frac{1}{256} \dots \\ &\approx 0.754 - 0.19\lambda + 0.016\lambda^2 - 6.1 \times 10^{-5} \lambda^3 \end{aligned} \quad (2-65)$$

The terms larger than the  $\lambda^2$  term are small and can be ignored; thus, Eq. 2-63 the model becomes,

$$\varepsilon(\lambda) = D0.016\lambda^2 + (DE - D0.19)\lambda + DF0.754. \quad (2-66)$$

We are left with a second order polynomial as the fit for the emissivity profile.

While the explicit diffraction effects have not been included in this analysis, the general approach has been discussed. The second order polynomial in equation 2-64 has, in the past, provided a good characterization of the emissivity profiles for metals<sup>39</sup>. Consequently, the next section will determine the emissivity model using real data.

## 2.4. Verification Of Model

To validate the emissivity model proposed in this dissertation, an experiment was set up using heated plates of aluminum and copper. The samples were sanded to remove any oxidation, attached to an extended blackbody, and heated to various temperatures from 100 to 250 K. A Fourier-transform IR spectrometer manufactured by Bomem, Inc., was used to collect spectral information, and a system of equations was constructed. As shown in Equation 2-1, the emissivity for a material can be expanded to as many orders as there are spectral regions in our spectrometer. However, due to computational rounding errors, the calculations of coefficients beyond the seventh-order are erroneous. Consequently, the experiment gathered only seven spectral values. This was sufficient for the validation, because the series, in our model, should converge after the third term. The seven coefficients for the emissivity model were calculated using experimental data collected for aluminum and copper samples. The system of equations was set up as follows:

$$ADU_{\lambda_i} = \int_{\lambda_{i_{min}}}^{\lambda_{i_{max}}} \frac{c_1(a_1\lambda^6 + a_2\lambda^5 + a_3\lambda^4 + a_4\lambda^3 + a_5\lambda^2 + a_6\lambda + a_7)}{\lambda^5 \left( e^{\frac{c_2}{\lambda T}} - 1 \right)} R_i(\lambda) d\lambda, \text{ for } i=1,2,\dots,7, \quad (2-67)$$

where:

$ADU_{\lambda_i}$  = The number of Analog Digital Units (ADU) output for each detector

$T$  = Temperature of target

$\lambda$  = Wavelength in microns

$R_i(\lambda)$  = Response of detector/filter and transmission of optics in each of the spectral regions (ADU/Watt)

$d\lambda$  = Differential wavelength

The  $R_i(\lambda)$  term defines the limits of the integral. Note that detector gain, offset, solid angle, and atmospheric transmission terms have been left out of equation 2-67. The system did not have a direct means to calibrate out these effects and, consequently, the unknown constant terms were lumped into the unknown constants for emissivity,  $a_1$  through  $a_7$ . Rearranging the terms, equation 2-77 becomes

$$\begin{aligned}
 ADU_{\lambda} = & a_1 \int_{\lambda_{min}}^{\lambda_{max}} \frac{c_1 R_1(\lambda) d\lambda}{\lambda^4 \left( e^{\frac{c_2}{\lambda T}} - 1 \right)} + a_2 \int_{\lambda_{min}}^{\lambda_{max}} \frac{c_1 R_2(\lambda) d\lambda}{\lambda^4 \left( e^{\frac{c_2}{\lambda T}} - 1 \right)} + a_3 \int_{\lambda_{min}}^{\lambda_{max}} \frac{c_1 R_3(\lambda) d\lambda}{\lambda^4 \left( e^{\frac{c_2}{\lambda T}} - 1 \right)} + a_4 \int_{\lambda_{min}}^{\lambda_{max}} \frac{c_1 R_4(\lambda) d\lambda}{\lambda^4 \left( e^{\frac{c_2}{\lambda T}} - 1 \right)} \\
 & \text{for } i=1,2,\dots,7. \quad (2-68) \\
 & + a_5 \int_{\lambda_{min}}^{\lambda_{max}} \frac{c_1 R_5(\lambda) d\lambda}{\lambda^4 \left( e^{\frac{c_2}{\lambda T}} - 1 \right)} + a_6 \int_{\lambda_{min}}^{\lambda_{max}} \frac{c_1 R_6(\lambda) d\lambda}{\lambda^4 \left( e^{\frac{c_2}{\lambda T}} - 1 \right)} + a_7 \int_{\lambda_{min}}^{\lambda_{max}} \frac{c_1 R_7(\lambda) d\lambda}{\lambda^4 \left( e^{\frac{c_2}{\lambda T}} - 1 \right)}
 \end{aligned}$$

The system of equations is non-linear, but, when the temperature is known (as for the validation experiment) Equation 2-68 becomes linear. The -1 in the denominator is small compared to the first term,  $e^{\frac{c_2}{\lambda T}}$ , and can be left out of the expression. The temperature dependent constants,  $e^{\frac{c_2}{\lambda_i T}}$ , as well as other constants of the system, are lumped into an overall temperature dependent constant,  $c_n(T)$ . The equations can be rewritten as:

$$\begin{aligned}
ADU_{\lambda} = & a_1 \int_{\lambda_{\min}}^{\lambda_{\max}} c_1(T) \frac{R(\lambda) d\lambda}{\lambda^1} + a_2 \int_{\lambda_{\min}}^{\lambda_{\max}} c_2(T) \frac{R(\lambda) d\lambda}{\lambda} + a_3 \int_{\lambda_{\min}}^{\lambda_{\max}} c_3(T) \frac{R(\lambda) d\lambda}{\lambda} \\
& + a_4 \int_{\lambda_{\min}}^{\lambda_{\max}} c_3(T) \frac{R(\lambda) d\lambda}{\lambda^2} + a_5 \int_{\lambda_{\min}}^{\lambda_{\max}} c_1(T) \frac{R(\lambda) d\lambda}{\lambda^2} + a_6 \int_{\lambda_{\min}}^{\lambda_{\max}} c_2(T) \frac{R(\lambda) d\lambda}{\lambda^2} \quad \text{for } i=1,2,\dots,7. \quad (2-69) \\
& + a_7 \int_{\lambda_{\min}}^{\lambda_{\max}} c_3(T) \frac{R(\lambda) d\lambda}{\lambda}
\end{aligned}$$

Each of the integrals can be evaluated. Rewriting, Eq. 2-66 becomes

$$\begin{aligned}
ADU_{\lambda_i} = & a_1 I_{1_i}(T) + a_2 I_{2_i}(T) + a_3 I_{3_i}(T) \\
& + a_4 I_{4_i}(T) + a_5 I_{5_i}(T) + a_6 I_{6_i}(T) + a_7 I_{7_i}(T), \quad \text{for } i=1,2,\dots,7 \quad (2-70)
\end{aligned}$$

or can be rewritten in linear algebra form as

$$\begin{bmatrix} ADU_{\lambda_1} \\ ADU_{\lambda_2} \\ ADU_{\lambda_3} \\ ADU_{\lambda_4} \\ ADU_{\lambda_5} \\ ADU_{\lambda_6} \\ ADU_{\lambda_7} \end{bmatrix} = \begin{bmatrix} I_{1_1}(T) & I_{2_1}(T) & I_{3_1}(T) & I_{4_1}(T) & I_{5_1}(T) & I_{6_1}(T) & I_{7_1}(T) \\ I_{1_2}(T) & I_{2_2}(T) & I_{3_2}(T) & I_{4_2}(T) & I_{5_2}(T) & I_{6_2}(T) & I_{7_2}(T) \\ I_{1_3}(T) & I_{2_3}(T) & I_{3_3}(T) & I_{4_3}(T) & I_{5_3}(T) & I_{6_3}(T) & I_{7_3}(T) \\ I_{1_4}(T) & I_{2_4}(T) & I_{3_4}(T) & I_{4_4}(T) & I_{5_4}(T) & I_{6_4}(T) & I_{7_4}(T) \\ I_{1_5}(T) & I_{2_5}(T) & I_{3_5}(T) & I_{4_5}(T) & I_{5_5}(T) & I_{6_5}(T) & I_{7_5}(T) \\ I_{1_6}(T) & I_{2_6}(T) & I_{3_6}(T) & I_{4_6}(T) & I_{5_6}(T) & I_{6_6}(T) & I_{7_6}(T) \\ I_{1_7}(T) & I_{2_7}(T) & I_{3_7}(T) & I_{4_7}(T) & I_{5_7}(T) & I_{6_7}(T) & I_{7_7}(T) \end{bmatrix} \cdot \begin{bmatrix} a_1 \\ a_2 \\ a_3 \\ a_4 \\ a_5 \\ a_6 \\ a_7 \end{bmatrix}. \quad (2-71)$$

The solution for the unknown coefficients  $a_1, a_2, a_3, \dots$  is

$$\begin{bmatrix} a_1 \\ a_2 \\ a_3 \\ a_4 \\ a_5 \\ a_6 \\ a_7 \end{bmatrix} = \begin{bmatrix} I_{1_1}(T) & I_{2_1}(T) & I_{3_1}(T) & I_{4_1}(T) & I_{5_1}(T) & I_{6_1}(T) & I_{7_1}(T) \\ I_{1_2}(T) & I_{2_2}(T) & I_{3_2}(T) & I_{4_2}(T) & I_{5_2}(T) & I_{6_2}(T) & I_{7_2}(T) \\ I_{1_3}(T) & I_{2_3}(T) & I_{3_3}(T) & I_{4_3}(T) & I_{5_3}(T) & I_{6_3}(T) & I_{7_3}(T) \\ I_{1_4}(T) & I_{2_4}(T) & I_{3_4}(T) & I_{4_4}(T) & I_{5_4}(T) & I_{6_4}(T) & I_{7_4}(T) \\ I_{1_5}(T) & I_{2_5}(T) & I_{3_5}(T) & I_{4_5}(T) & I_{5_5}(T) & I_{6_5}(T) & I_{7_5}(T) \\ I_{1_6}(T) & I_{2_6}(T) & I_{3_6}(T) & I_{4_6}(T) & I_{5_6}(T) & I_{6_6}(T) & I_{7_6}(T) \\ I_{1_7}(T) & I_{2_7}(T) & I_{3_7}(T) & I_{4_7}(T) & I_{5_7}(T) & I_{6_7}(T) & I_{7_7}(T) \end{bmatrix}^{-1} \cdot \begin{bmatrix} ADU_{\lambda_1} \\ ADU_{\lambda_2} \\ ADU_{\lambda_3} \\ ADU_{\lambda_4} \\ ADU_{\lambda_5} \\ ADU_{\lambda_6} \\ ADU_{\lambda_7} \end{bmatrix}. \quad (2-72)$$

The data from the spectrometer were substituted into equation 2-72 and the solution attained. The terms are higher than second order were effectively zero. Consequently, these terms are omitted. Since there were no calibrated emissivity plots for the aluminum and copper test items only the general trend in data could be calculated. The general setup for the test is shown in Figure 2-2.

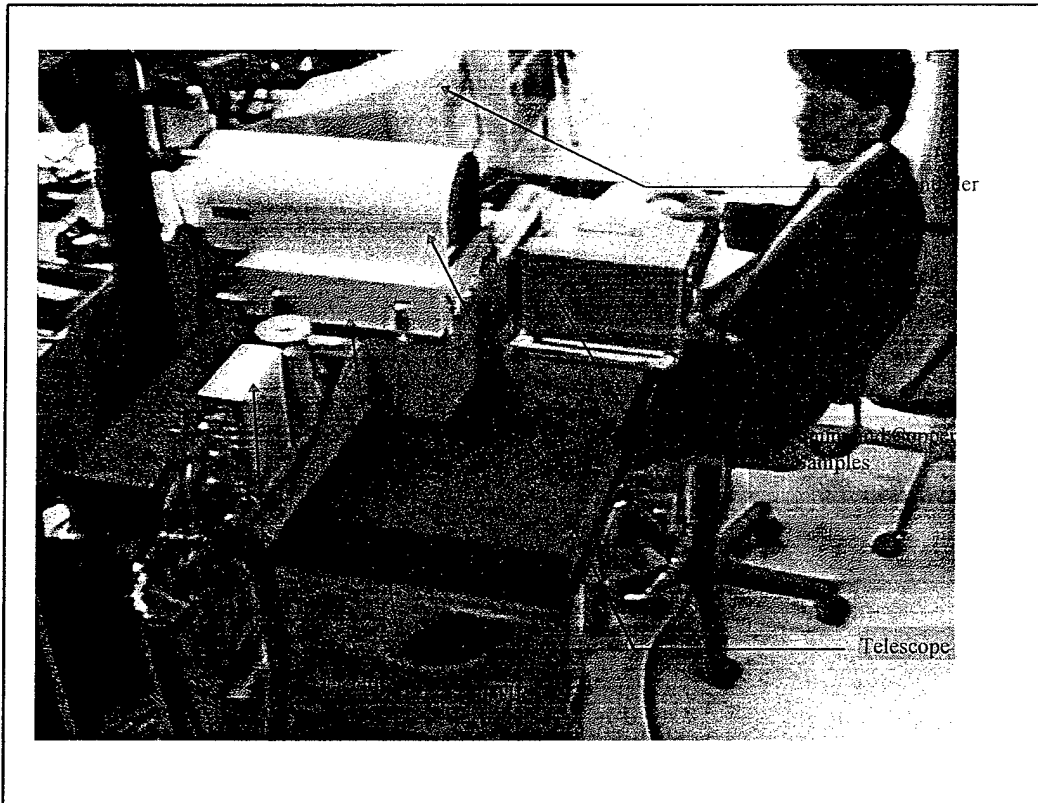


**Figure 2-2:** Validation experiment. The components for this experiment were delivered on a contract from the government to Bomem, Inc.

This experiment did show that the emissivity for the two metals was modeled very well by a second-degree polynomial. Figures 2-3 and 2-4 show a plots of the fit for emissivity. As higher order fits were accomplished, no additional accuracy was gained.

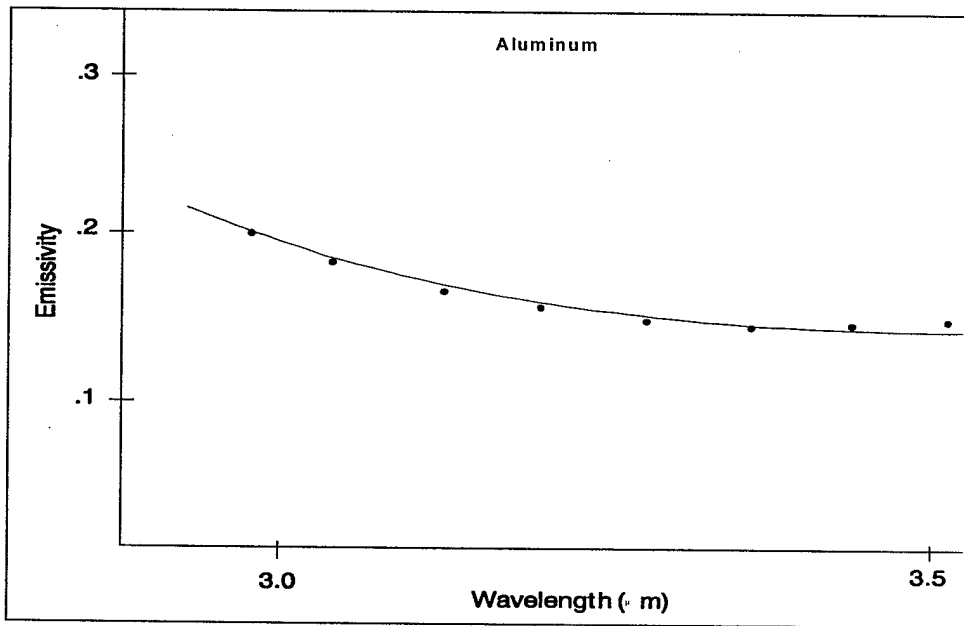


Figure 2-3: Plot of aluminum emissivity profile. The solid line represents a second-degree polynomial.

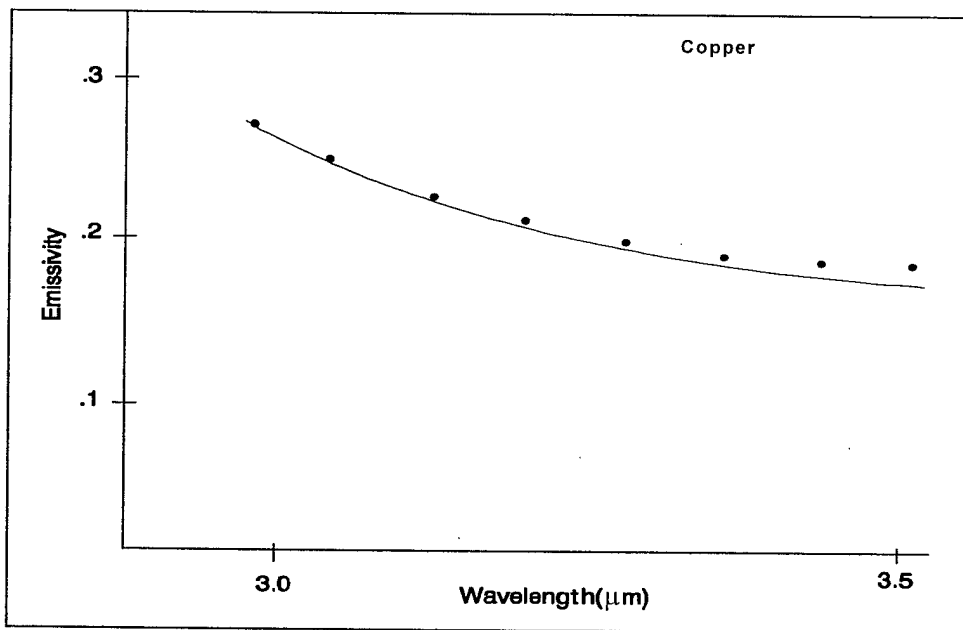


Figure 2-4: Plot of copper emissivity profile. The solid line represents second degree polynomial.

This validation experiment gave credence to the approach of building a four-color pyrometer. Before moving on to the technical discussion of this new instrumentation the algorithms used to

reconstruct the validation experiment data should be detailed. These algorithms were also used in the four-color pyrometer system.

## **2.5. Algorithm design**

As mentioned earlier, the system of equations generated from the multi-spectral measurements is nonlinear due to the terms associated with the Planck distribution; consequently, a nonlinear regression would be required to attain a solution. These equations can be made linear by holding the temperature constant. After a solution is attained, an error function establishes the accuracy of the predicted temperature. A regression through temperature will find the true temperature at the minimum error function. In this section, two approaches to finding the linear solution will be presented, and the section will conclude with a nonlinear technique.

In the last section it was shown that a second order polynomial provides a accurate fit for the emissivity profile. Consequently, only spectral information is needed about four regions of the emissivity profile. Simulated multi-spectral data was used to check each algorithm for performance against varying emissivity profiles and amounts of noise in the system. All three techniques were used to reconstruct the temperature using the new imaging pyrometer, and a comparison is presented in the results section.

### **2.5.1. Algorithm Design And Simulation (Gaussian Elimination)**

The first linear solution technique uses Gaussian elimination as the basis to find a solution to the system of four equations constructed from four spectral measurements. With a second degree polynomial as the model for emissivity the four equations setup by the four color pyrometer are

$$ADU_{\lambda_i} = \int_{\lambda_{i\min}}^{\lambda_{i\max}} \frac{c_1(a_1\lambda^2 + a_2\lambda + a_3)}{\lambda^5 \left( e^{\frac{c_2}{\lambda T}} - 1 \right)} R_i(\lambda) d\lambda \quad \text{for } i=1, 2, 3 \text{ \& } 4 \quad (2-73)$$

Rearranging the terms, equation 2-73 becomes

$$ADU_{\lambda_i} = a_1 \int_{\lambda_{i\min}}^{\lambda_{i\max}} \frac{c_1 R_i(\lambda) d\lambda}{\lambda^5 \left( e^{\frac{c_2}{\lambda T}} - 1 \right)} + a_2 \int_{\lambda_{i\min}}^{\lambda_{i\max}} \frac{c_1 R_i(\lambda) d\lambda}{\lambda^4 \left( e^{\frac{c_2}{\lambda T}} - 1 \right)} + a_3 \int_{\lambda_{i\min}}^{\lambda_{i\max}} \frac{c_1 R_i(\lambda) d\lambda}{\lambda^3 \left( e^{\frac{c_2}{\lambda T}} - 1 \right)} \quad \text{for } i=1, 2, 3 \text{ \& } 4 \quad (2-74)$$

If the temperature is held constant, then any three of the four equations has a linear solution. The first three equations can be written as

$$ADU_{\lambda_i} = a_1 \int_{\lambda_{i\min}}^{\lambda_{i\max}} c_1(T) \frac{R_i(\lambda) d\lambda}{\lambda^3} + a_2 \int_{\lambda_{i\min}}^{\lambda_{i\max}} c_2(T) \frac{R_i(\lambda) d\lambda}{\lambda^2} + a_3 \int_{\lambda_{i\min}}^{\lambda_{i\max}} c_3(T) \frac{R_i(\lambda) d\lambda}{\lambda} \quad \text{for } i=1, 2, \text{ \& } 3 \quad (2-75)$$

Each of the integrals can be evaluated,

$$ADU_{\lambda_i} = a_1 I_{1_i}(T) + a_2 I_{2_i}(T) + a_3 I_{3_i}(T) \quad \text{for } i=1, 2, \text{ \& } 3, \quad (2-76)$$

or can be rewritten in linear algebra form as

$$\begin{bmatrix} ADU_{\lambda_1} \\ ADU_{\lambda_2} \\ ADU_{\lambda_3} \end{bmatrix} = \begin{bmatrix} I_{1_1}(T) & I_{2_1}(T) & I_{3_1}(T) \\ I_{1_2}(T) & I_{2_2}(T) & I_{3_2}(T) \\ I_{1_3}(T) & I_{2_3}(T) & I_{3_3}(T) \end{bmatrix} \cdot \begin{bmatrix} a_1 \\ a_2 \\ a_3 \end{bmatrix} \quad (2-77)$$

The solution for the unknown coefficients  $a_1$ ,  $a_2$ , &  $a_3$  is

$$\begin{bmatrix} a_1 \\ a_2 \\ a_3 \end{bmatrix} = \begin{bmatrix} I_{1_1}(T) & I_{2_1}(T) & I_{3_1}(T) \\ I_{1_2}(T) & I_{2_2}(T) & I_{3_2}(T) \\ I_{1_3}(T) & I_{2_3}(T) & I_{3_3}(T) \end{bmatrix}^{-1} \cdot \begin{bmatrix} ADU_{\lambda_1} \\ ADU_{\lambda_2} \\ ADU_{\lambda_3} \end{bmatrix} \quad (2-78)$$

There many techniques for inverting a matrix and their usage depends on the specific application. The Gaussian elimination method was chosen because it provides the greatest versatility and it is easily implemented. The code implementing matrix inversion was taken from Numerical Recipes<sup>40</sup> and is documented in appendix A.

In addition, in appendix A is an algorithm that was used to analyze the viability of the linear solution discussed above. The first step is to simulate real data. Figure 3.5 shows the emissivity profile that was generated in the VARCAL subroutine by fitting a second-degree polynomial to three points, chosen arbitrarily. The emissivity was used with the spectral filter characteristic to simulate the energy seen at each of the four detectors in the DATUM subroutine. This generated the simulated detector responses for the imaging spectrometer. The filter characteristics, also plotted, were generated in the FILTERS subroutine. A Gaussian filter shape was used for simplicity. In the real system the filter shapes were replaced with the actual filter characteristics and a solution for temperature found in the same way as for the simulation.

To find the solution for temperature, the coefficients generated from Gaussian elimination are used in the fourth equation. If there is an error in this fourth equation, the assumed temperature is increased or decreased, and the above process repeated. In addition, a random error ( $\text{RND}(1) * \text{ER}$ ) was added to simulate noise. The FITDATUM subroutine finds the coefficients to the polynomial data fit, where temperature is constant, and uses the fourth equation to calculate the error in that fit. The main routine loops through all values of temperature and the error is output to the screen for each temperature. The solution for temperature is found when the error in the fourth equation is minimized.

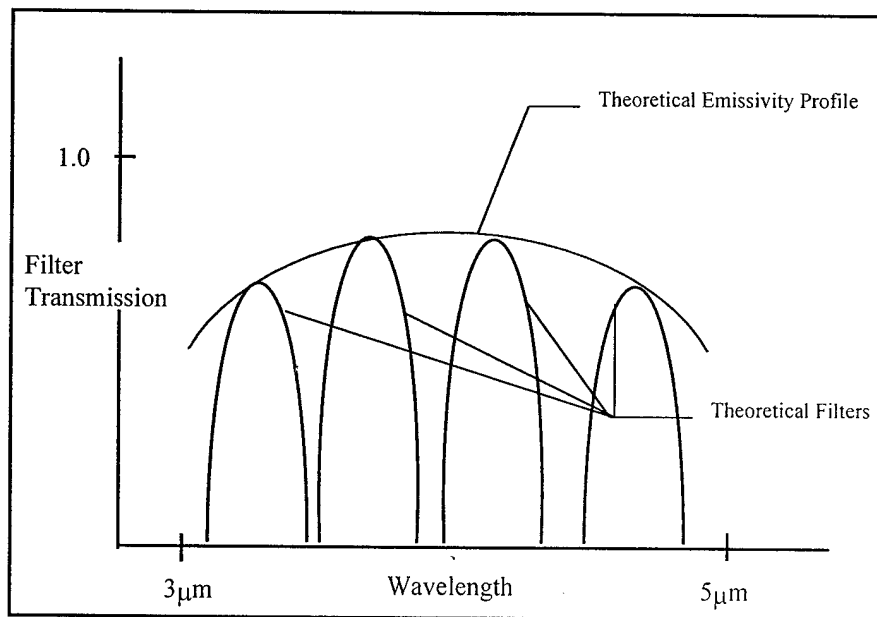


**Figure 2-5:** Simulated filters and emissivity to test algorithm performance

This algorithm has performed quite well on the simulated data. With no noise added to the data (i.e.,  $ER=0$ ), the error at the correct temperature is essentially zero when neglecting computational rounding errors (eighth decimal place, or so). As error is added, the algorithm deviates from the ideal. However, if the noises are within the Poisson photon noise limited, seen in a low noise detector system, then the system will be able to attain much better than one-degree accuracy.

### 2.5.2. Singular Value Decomposition

In the last subsection, a straight forward solution to the system of equations was presented, where a simple matrix inversion was utilized. If this matrix was either singular or numerically close to singular, inversion using Gaussian elimination would fail due to computational rounding errors. However, Singular Value Decomposition (SVD) can be successfully used to invert such a matrix. In addition, SVD is a powerful method for solving

most linear least-squares problems. For the imaging spectrometer of this dissertation the nature of singularity will only be experienced when the images have significant overlap between the adjacent spectral regions. Overlap can be essentially eliminated with careful design and, consequently, SVD will be used as a method to accomplish a least-squares fit of the data.

SVD methods are based on the following theorem of linear algebra, the proof of which is beyond the scope of this dissertation: Any matrix  $A$  whose number of rows  $M$  is greater than or equal to its number of columns  $N$ , can be written as the product of an  $M \times N$  column-orthogonal matrix,  $U$ , an  $N \times N$  diagonal matrix,  $W$ , with positive or zero elements (the singular values), and the transpose of the  $N \times N$  orthogonal matrix,  $V$ .

$$\begin{pmatrix} A \end{pmatrix} = \begin{pmatrix} U \end{pmatrix} \cdot \begin{pmatrix} w_1 \\ w_2 \\ \vdots \\ w_N \end{pmatrix} \cdot \begin{pmatrix} V^T \end{pmatrix} \quad (2-79)$$

The matrices  $U$  and  $V$  are each orthogonal in the sense that their columns are orthonormal.

$$\begin{pmatrix} U^T \end{pmatrix} \cdot \begin{pmatrix} U \end{pmatrix} = \begin{pmatrix} V^T \end{pmatrix} \cdot \begin{pmatrix} V \end{pmatrix} \quad (2-80)$$

$$= \begin{pmatrix} 1 \end{pmatrix}$$

Since  $V$  is square, it is also row-orthogonal,  $V \cdot V^T = 1$ .

The intent of this method is to solve the same system of equations as was solved for in the last section. Again these equations are non-linear but can be made linear by assuming a temperature. This will give us four equations, one from each of the four colors of the imaging

spectrometer, and three unknowns for the coefficients of emissivity. This is represented in linear algebra form in equation 2-91 and 2-92.

$$\begin{bmatrix} a_1 \\ a_2 \\ a_3 \end{bmatrix} = \begin{bmatrix} I_{1_1}(T) & I_{2_1}(T) & I_{3_1}(T) \\ I_{1_2}(T) & I_{2_2}(T) & I_{3_2}(T) \\ I_{1_3}(T) & I_{2_3}(T) & I_{3_3}(T) \\ I_{1_4}(T) & I_{2_4}(T) & I_{3_4}(T) \end{bmatrix}^{-1} \begin{bmatrix} ADU_{\lambda_1} \\ ADU_{\lambda_2} \\ ADU_{\lambda_3} \\ ADU_{\lambda_4} \end{bmatrix} \quad (2-81)$$

or

$$\begin{bmatrix} a_1 \\ a_2 \\ a_3 \end{bmatrix} = \begin{bmatrix} A \end{bmatrix}^{-1} \begin{bmatrix} ADU_{\lambda_1} \\ ADU_{\lambda_2} \\ ADU_{\lambda_3} \\ ADU_{\lambda_4} \end{bmatrix} \quad (2-82)$$

Writing in the form of the decomposed matrix, we have

$$\begin{bmatrix} a_1 \\ a_2 \\ a_3 \end{bmatrix} = \begin{bmatrix} V \end{bmatrix} \begin{bmatrix} diag(1/w_j) \end{bmatrix} \begin{bmatrix} U^T \end{bmatrix} \begin{bmatrix} ADU_{\lambda_1} \\ ADU_{\lambda_2} \\ ADU_{\lambda_3} \\ ADU_{\lambda_4} \end{bmatrix} \quad (2-83)$$

After the SVD calculates the coefficients for emissivity they can be substituted back into the four equations and an error calculated for each. The temperature can then be incremented and, as for the Gaussian elimination technique, the solution for temperature is reached when this error is minimized.

The implementation of an SVD algorithm developed in Numerical Recipes provided a solution to equation 2-93 and is also listed in the appendix A.<sup>41</sup> A function call from the main program to the SVD subroutines is made in the same manner as was done for the Gaussian elimination regression techniques. This algorithm uses the same simulated data (emissivity profile, filter responses, error, etc.) to verify the accuracy of the fit to the data in the presence of noise. While this application of multi-spectral pyrometry generates a matrix that is non-singular,

the SVD does provide a least-squares fit of the data that is accurate, and nearly as accurate as the Gaussian elimination technique.

### 2.5.3. Levenberg Marquardt Nonlinear Optimization

The previous two techniques took advantage of the fact that only one non-linear term, temperature, is associated with the system of equations. While holding the temperature constant and solving the residual linear set of equations is a valid mathematical technique, if more terms were associated with the non-linearity then the solution to the system of equations would almost surely require a non-linear approach. Modeling emissivity as a second-degree polynomial is one method. However, if bound surface states or other material properties become more significant in the overall IR spectral radiation, the likelihood of a second-degree polynomial serving as a good fit for emissivity is diminished. Although higher-degree polynomials would provide adequate fits. However, instrumentation inaccuracies increase strongly as the number of required wavelengths increase. Consequently, there is a high degree of likelihood that a non-linear system of equations would result in the best fitting of the emissivity.

The Levenberg-Marquardt is an elegant method to accomplish a nonlinear least-squares fit of the data to the model. This technique can be used when the merit function varies smoothly between extremes of the inverse Hessian method.<sup>42</sup> The Hessian method defines the direction of the optimization profile (curvature). When the Hessian method nears the solution the steepest ascent method is used to find the global solution. The Levenberg-Marquardt method reduces the merit function of a fit between a set of data points  $x(1...ndata)$ ,  $y(1...ndata)$  with individual standard deviations. The emissivity coefficients and temperature require seeding before the algorithm can find a solution. If the estimate of the magnitude is too far from the true coefficients or if the model is inaccurate, there is a high probability that the algorithm will become trapped in a local minimum.

The simulation showed that for some emissivity profiles this algorithm found solutions for emissivity and temperature that were far off the simulated values even with little as no noise added to the system. For most of emissivity profiles that would be realistically encountered from

metals, the algorithm performed fairly well but not nearly as well as the two linear techniques. As for the two linear methods, the algorithm to accomplish the Levenberg-Marquardt was obtained from Numerical Recipes. The implementation of this algorithm was a function call to subroutines from the main program implementing the three regression techniques and this code is again documented in appendix A.

## 2.6. Noise Contribution to Temperature Error

The contribution of noise to the system accuracy can be determined through an analysis of the extreme data points. In other words, if there are two equations each with a  $\pm$  error, then the maximum error will occur in one of four the fits to the two erroneous data values. For the system of four equations there will be error in optical power collected for each of the spectral regions. The matrix below describes the error associated with our system if the noise is limited by the background and the read noise.

$$\begin{bmatrix} a_1 \\ a_2 \\ a_3 \end{bmatrix} = \begin{bmatrix} I_{1_1}(T) & I_{2_1}(T) & I_{3_1}(T) \\ I_{1_2}(T) & I_{2_2}(T) & I_{3_2}(T) \\ I_{1_3}(T) & I_{2_3}(T) & I_{3_3}(T) \end{bmatrix}^{-1} \cdot \begin{bmatrix} \Phi q_{\lambda_1} \pm \sqrt{\Phi q_{\lambda_1} + \sigma_{read}^2} \\ \Phi q_{\lambda_2} \pm \sqrt{\Phi q_{\lambda_2} + \sigma_{read}^2} \\ \Phi q_{\lambda_3} \pm \sqrt{\Phi q_{\lambda_3} + \sigma_{read}^2} \end{bmatrix} \quad (2-84)$$

In the calculation of the argument coefficients,  $a_n$ 's, one combination of the six error values, associated with the  $\pm$  error of the noise will be the maximum error in the calculated temperature. The algorithm in appendix A calculates the temperature error associated with a given percentage error in the collected optical energy. It was found during the simulation portion of this research that when using either of the linear techniques, an error of less than 5% (S/N of 20) would contribute no more than a  $\pm 5^\circ \text{C}$  to the error in predicting temperature. To determine

the accuracy of the system different emissivity profiles were simulated for various temperatures. The following two figures document the simulation results.

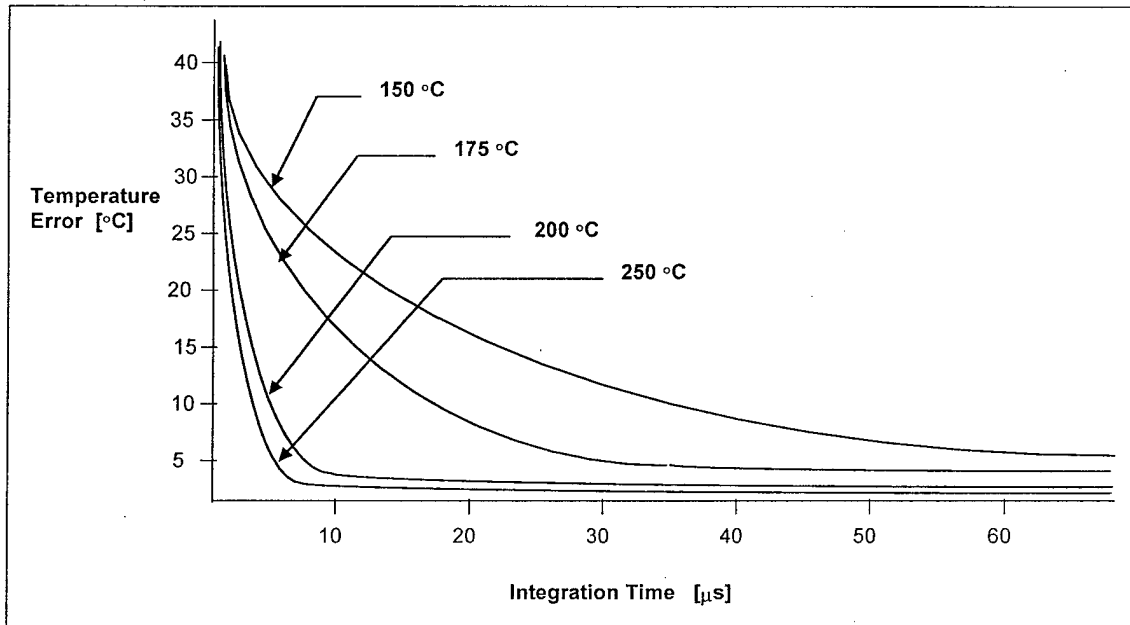
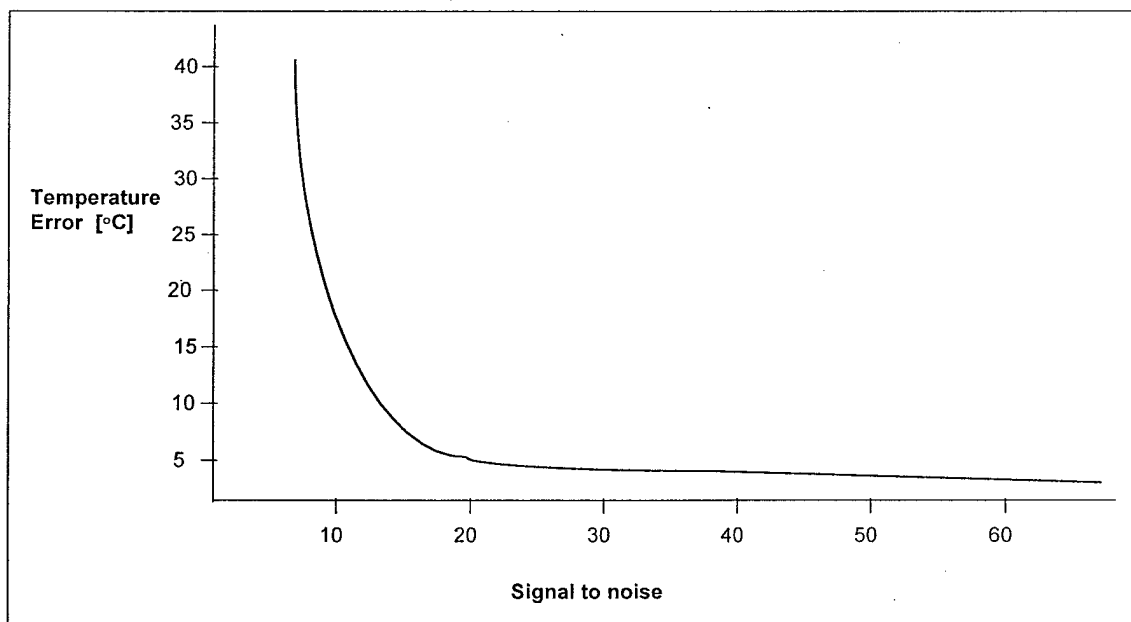


**Figure 2-6:** System temperature accuracy versus detector integration time.



**2-7:** System temperature accuracy versus signal to noise.

**Figure**

The Levenberg-Marquardt technique did not perform as well for all emissivity profiles but nearly as well for some, approximately  $\pm 30\text{ C}^\circ$ . Since the signal to noise ratio will not exceed an error of then 5%, as will be discussed in the radiometry section of this dissertation, the true limitation of this technique lies in the model for emissivity and calibration procedure for the electronics. These topics will be detailed in the technical portion of this dissertation.

### 3. Imaging Pyrometer Design

As mentioned earlier, multi-spectral imaging pyrometers of the past have been largely inaccurate. The primary problem here is keeping good calibration as the number of spectral regions increases. More than two or three spectral measurements have been shown to be useless. Accurate temperature prediction for high-speed deformation application requires four spectral measurements in the same IFOV. It is possible to form these four spectral images onto a single focal plane (Figure 3-1) and the common set of optics and electronics will substantially reduce system noise.

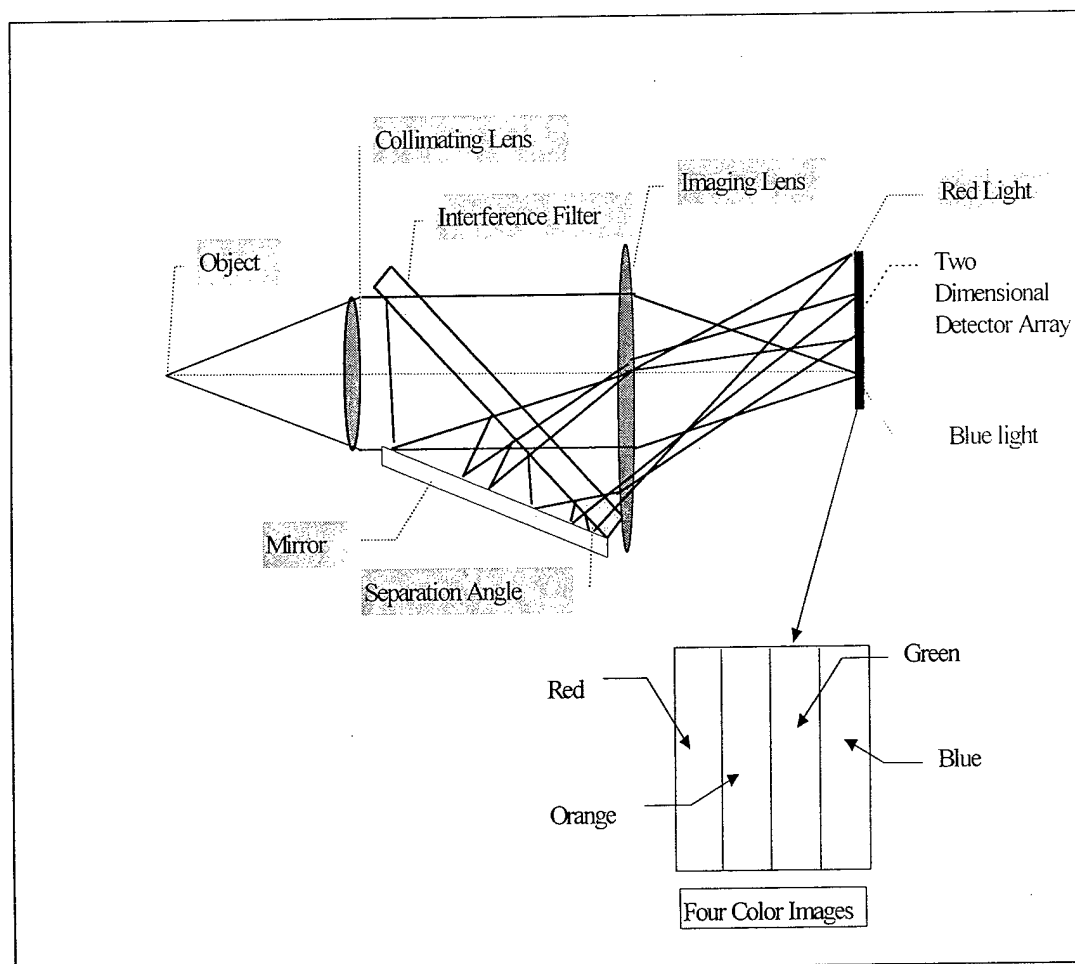


**Figure 3-1: Imaging Pyrometer**

One set of optics is used for a single detector array and a snapshot camera gathers all four images simultaneously. In addition, all components are stationary and, consequently, the system calibrates very accurately and remains calibrated for long periods of time. The general design of the components of the system will be detailed in this chapter. Discussion will then move on to the lens and interference filter designs. A general optical design is first covered in a step by step manner to show the evolution of the high speed imaging pyrometer produced from this dissertation.

### 3.1. General Design

The optics consist of a single interference filter that is used with a single mirror to separate a single beam of light into four spectral regions. The concept of the interference filter is that it changes its transmission characteristics with the angle of the incident optical energy. Figure 4.2 illustrates this filter process.

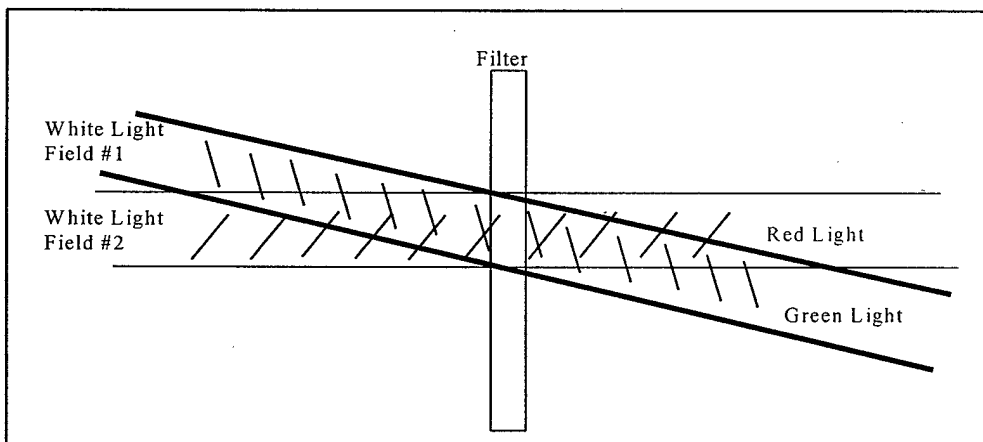


**Figure 3-2:** The property of an interference filter changing its pass band as the angle of incidence on the filter changes

The spectral energy not in the transmission band of the filter will see a near 100 per-cent reflection at the surface of the filter. As the field moves to angles of higher incidence, the filter

responds to shorter wavelengths. Consequently, as the filter is tilted the light that is passed for each of the fields shifts to shorter wavelengths (Figure 3-3).

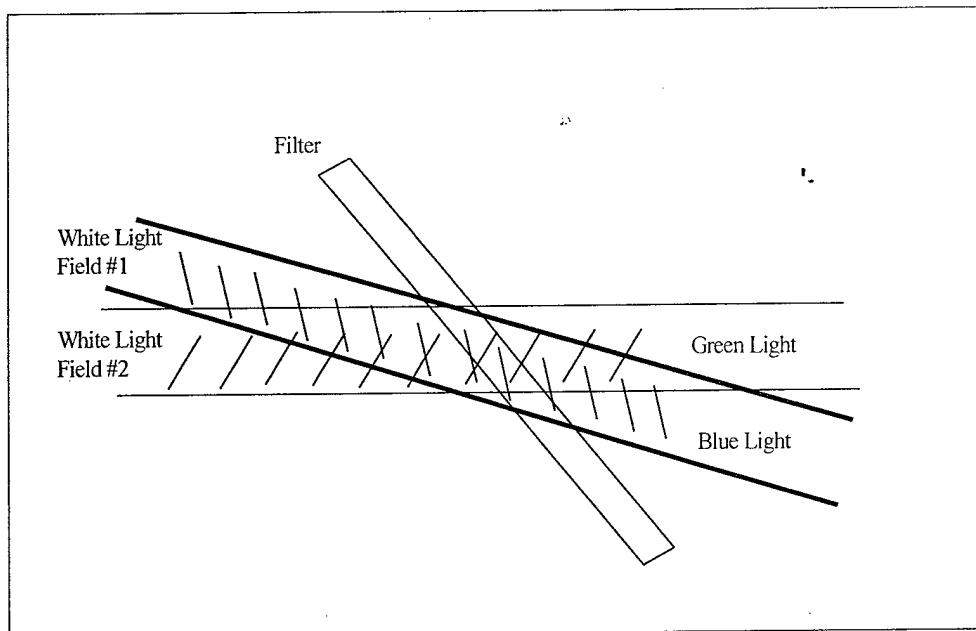


**Figure 3-3:** Interference filter behavior when tilted

It can be seen that the on-axis field moves to pass green light where the off-axis field moves to pass blue light. In an image forming system with the filter in a collimated space, the filter would respond as indicated Figure 3-4.

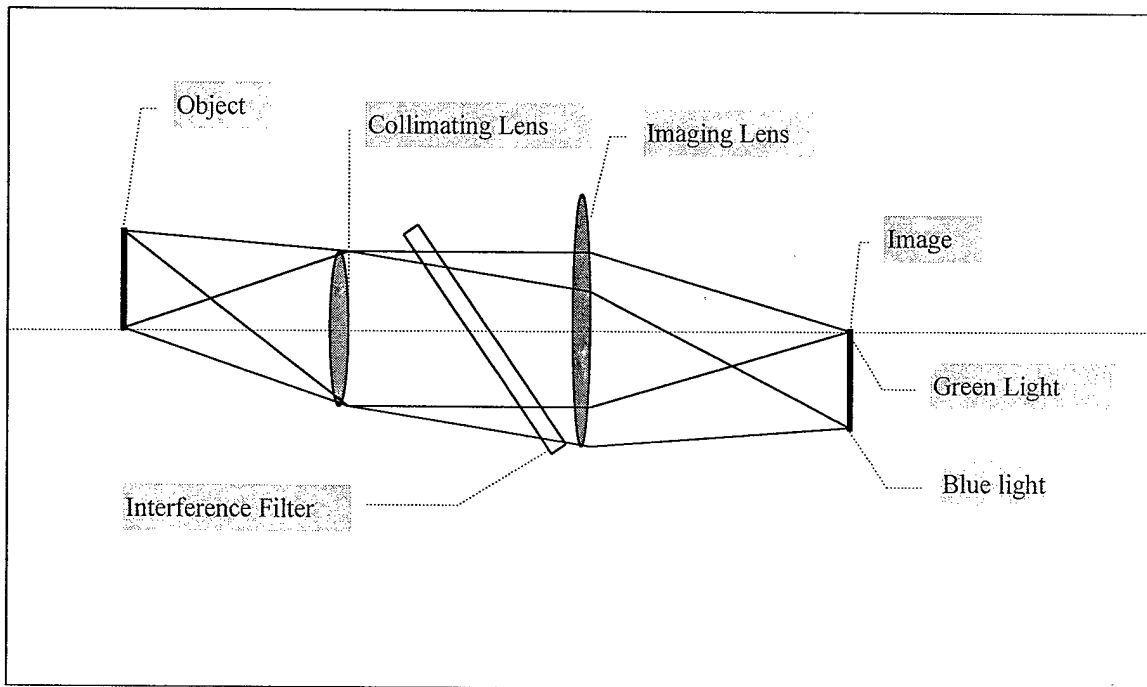


**Figure 3-4:** Lens configuration with untilted filter

If the object is a white light source, the image color will vary from long wavelength (green light) on axis, to shorter wavelengths (blue light) off axis. The next step is to create multiple images each with a unique spectral content. This can be done by adding a mirror to the setup to the left of the tilted interference filter, figure 3-5.

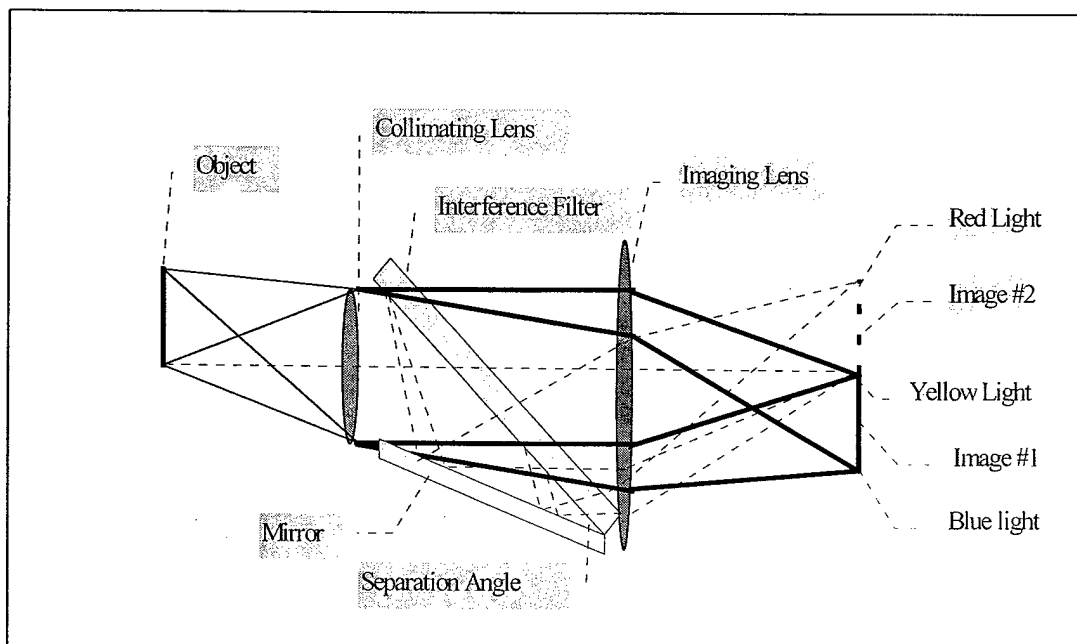


**Figure 3-5:** Lens Configuration with tilted filter and mirror to return reflected energy subsequently returning to the filter at an incremental angle

The solid lines correspond to the straight-through component of light. The light that is not passed through the filter is reflected at the filter surface, and this light is represented by the dashed lines. Subsequently, this reflected light experiences a second reflection at the mirror. The total deviation is twice the separation angle between the filter and the mirror. If this separation is done in collimated space, the angular change will alter the position that a field focuses onto a given focal plane without any defocus. To have contiguous images, the separation angle must be one half the maximum field angle subtended by the object. Additional images can be formed from additional reflections at the filter surface and each image will have a unique spectral content from passing through the interference filter at different angles. By taking advantage of these spectral transmission and reflection variations with incident angle, the need for multiple spectral filters is eliminated. In addition, multiple images are formed from the same beam of light making the spectrometer very fast.

In the past, imaging spectrometers have required significant time to scan the spectral energy onto a charge-coupled-device (CCD) or other readout device. This would take the form of a moving prism, diffraction grating or by moving filters in and out of the optical path. The application of predicting temperature for a ballistic projectile moving at 1000 meters per second or more with 1 mm resolution will require the spectrometer to gather all data in approximately one microsecond. The advantage of using this new technique is that the speed of the system is only limited by the integration time of the camera. Spectral energy is essentially picked off the optical path without losing the energy in adjacent spectral regions. This creates a system that is very light efficient which is extremely important for high speed applications. Now that the general high-speed instrument design has been detailed, the filter and lens components can be designed.

### **3.2. Interference Filter Design**

In classical optical systems, filters are designed to have small shifts in spectral characteristics with angle of incidence. The objective is to have all components of the cone of a focusing beam see the same pass band. The application in this dissertation takes advantage of shifting the band pass, therefore, the classical filter are not useful. The root of the design is in separating each of the images, spectrally, as much as possible. It is advantageous to separate the spectrum equally among the four filtered images so that irradiance remains somewhat constant across the array. To improve the interference filter, several phenomena can be taken advantage of in the design. The first design that was looked at involved changing the fundamental deposition of the multi-layer coatings. While classical designs attempt to minimize spectral shift, it is also feasible to maximize this shift. After accomplishing a few preliminary designs using the MACLEOD thin film design software and contacting filter vendors, it became apparent that the cost of manufacturing this interference filter was prohibitive.

The cost of the filter can be reduced by using a linear variable filter. Here, the shift in field position on the filter is used instead of relying solely on the angular shift to achieve all the spectral separation (Figure 3-6). The multiple optical paths traverse the interference plane in different locations and with the proper amount of shift (for this case somewhat non-linear) all the spectrum in the three to five micron band can be used. While this design worked well in simulation, it was still too expensive to manufacture and other, less expensive designs had to be considered.

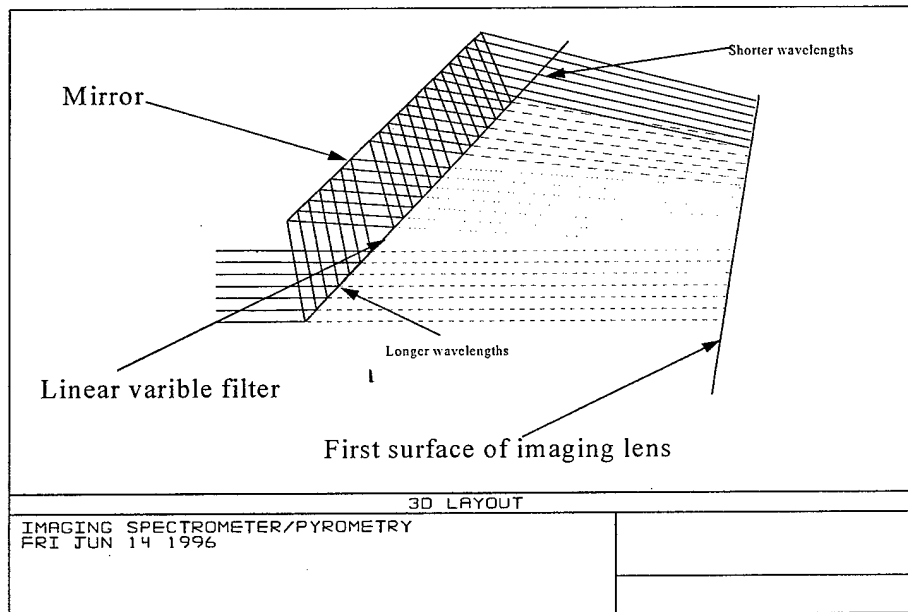


**Figure 3-6:** Using a linear variable filter to get the proper amount of wavelength shifts out of each spectral image.

The technique that was selected took advantage of optical path shift on the interference plane. Discrete filters at four locations of the plane were used to accomplish spectral separation. It can be seen in Figure 3-7 that each optical path is separated in the filter plane. This makes it easy to control the spectral content of each image on the focal plane.

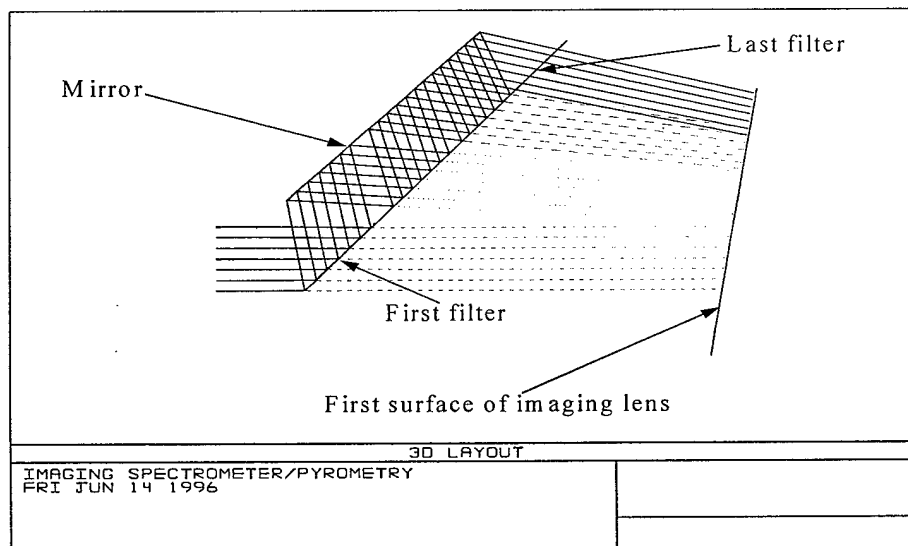


**Figure 3-7:** Discrete filter approach for effective filter separation

While it is desirable to manufacture all filters on the same substrate, again the manufacturing is cost prohibitive. Consequently, individual off-the-shelf filters were obtained from various vendors and adhered to a common substrate. Experimental results will be presented in the results section of this dissertation. Now that the interference filter has been designed the optical design can be completed.

### **3.3. Optical Lens Design**

The work on the lens design started with the paraxial characteristics of the system. Since the munition test setup is fairly compact the system was designed for finite conjugates with the nominal object distance at 0.5 meters. The order from left-to-right is the objective, collimation, and imaging lenses. The intermediate image, just after the objective lens, is the field stop, and the aperture stop is at the collimation lens.

The paraxial characteristics are driven by the field-of-view of the system and the number of spectral images designed to fall on the focal plane. In addition, since the interference filter design require the fields for the spectral images to be separated at the filter plane, the size of the imaging lens must to be larger. This problem will not be encountered when the filter is designed to spectrally separate the images using only angular shift. After this filter is manufactured the paraxial characteristics can be defined for the new system.

To start the design of the system of this dissertation the FOV first needed to be determined. The Amber focal plane is 8mm on a side and a 25mm focal length imaging lens was chosen so that the four images were separated by  $5^\circ$  on the focal plane. The objective and collimation lens combination is essentially a Keplerian telescope. There are two reasons for this design. First, the collimating lens needs to be reasonably small. If, for instance, the collimating lens were 25 mm in diameter, the separation between the filter and the mirror would be about 30mm for an initial incident angle of  $45^\circ$ . For no vignetting of the off-axis fields, the focal length of the imaging lens would need to be on the order of 25 mm. This drives the F/# of the

imaging lens to  $F/1$ . This is very fast and difficult to design. To increase the  $F/\#$ , the collimating lens was made smaller so that the image space ray bundle is more compact. In addition, the telescope allows a reduction in the field of view so that there is some stand off from the experiment. For the munition experiments that are performed, the objects are no larger than 25 mm. At the 500 mm object distance, makes the FOV, approximately  $1^\circ$  in object space. The collimating lens produces a  $5^\circ$  FOV making the magnification power 5. In addition, the telescope has an intermediate image plane, allowing the placement of a field stop. This will insure that there is no overlap of adjacent out-of-field spectral images.

The collimating lens was chosen to operate at  $F/2$  since an  $F/2$  system is reasonable to design. After running through a paraxial ray trace, it was found that, in order for the imaging lens to also operate at  $F/2$ , the collimating lens diameter needed to be approximately 5 mm. Now the paraxial characteristics can be computed.

focal length of objective = 50 mm

focal length of collocating lens = 10 mm

focal length of imaging lens = 25 mm

Lens design codes do not allow multiple transmissions through the single interference filter while keeping track of the reflected component. Consequently, this lens design was done in multiple configuration format. There are four configurations corresponding to the four passes through the filter. The reflected component from the filter is accomplished by molding the filter as a mirror. After the light has gone through the appropriate number of reflections the filter takes on its true characteristics. The figures below show a ray trace for the paraxial system discussed above.

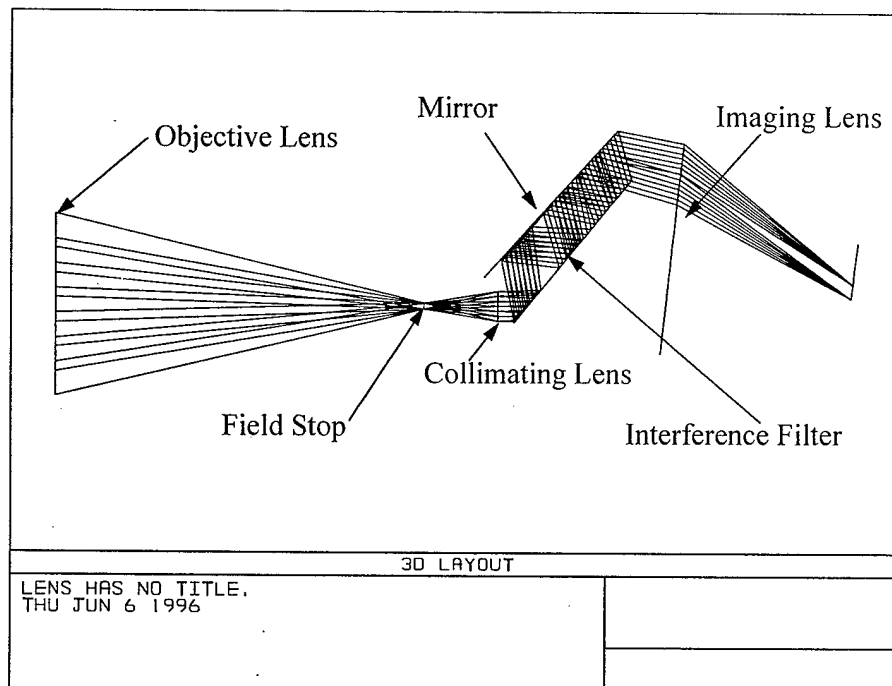


**Figure 3-8:** Paraxial lens design for the fourth reflected ray through the interference filter

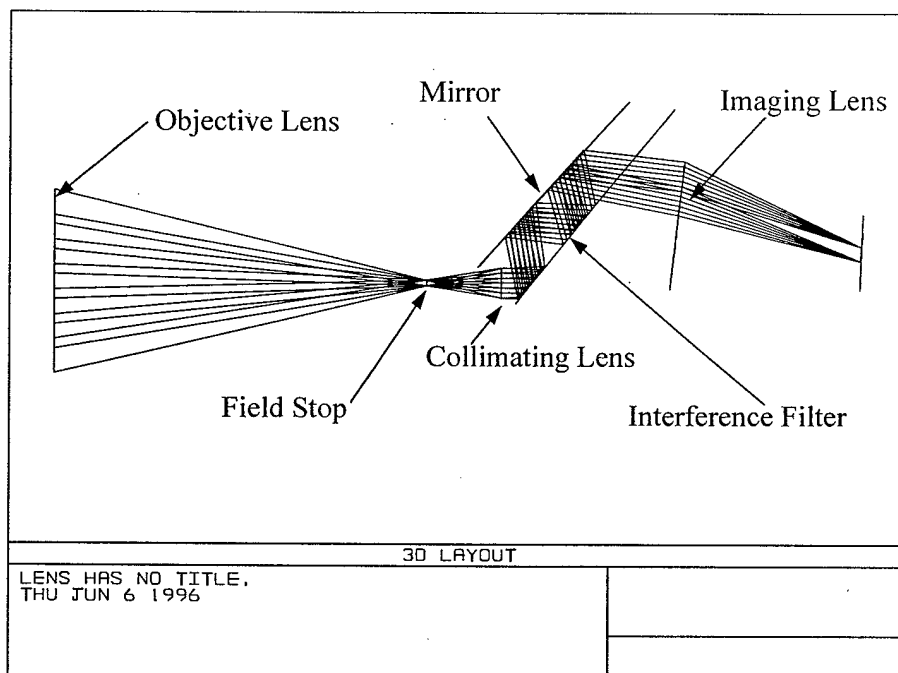


**Figure 3-9:** Paraxial lens design for the third reflected ray through the interference filter

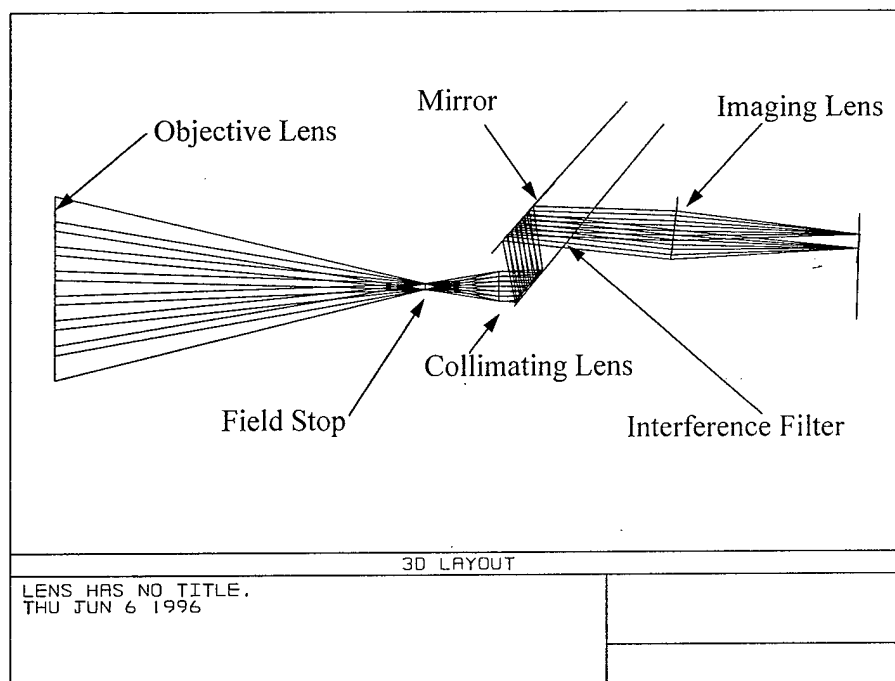


**Figure 3-10:** Paraxial lens design for the second reflected ray through the interference filter

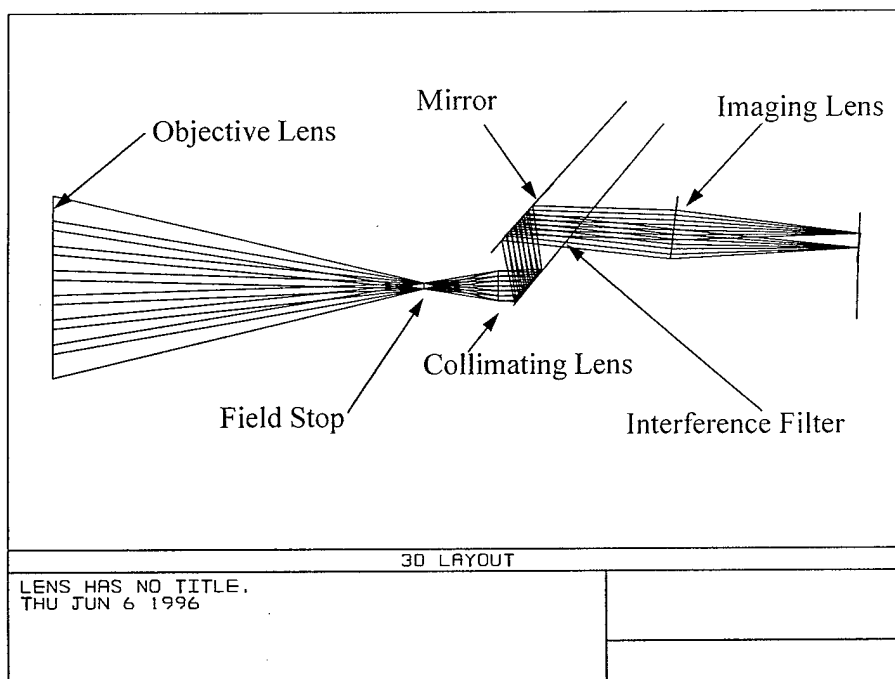


**Figure 3-11:** Paraxial lens design for the first reflected ray through the interference filter

After the paraxial characteristics of the system were defined, some real lenses could be put together. The analysis was started from an aberration point-of-view as to how each lens should be balanced. At this point, it was known that off-the-shelf lenses would be used. Consequently, the formal lens design was accomplished in order to determine the quality of each of the lens components. Another reason for completing this lens design is that, in general, the designs for off-the-self lenses are proprietary and are not easily obtained. The following design can be simplified somewhat if it was designed as a system. The cost of assembling these lens components for the prototype system, however, would be much higher than if off-the-shelf components were used.

For the objective lens, it is important that the image that occurs at the field stop be free from aberrations that shift the image location. The concern is whether or not the collimating lens truly collimates all of the fields. Each of the four images will experience different optical path lengths, causing the aberrations to vary at the imaging lens in a way not predicted by third-order or higher aberrations. At the very least, the collimating lens needs to compensate for objective aberrations. The objective lens was started with a single lens of germanium and best shape factor to minimize spherical aberration (sph3) for a 50mm focal length lens was found. Then, a second lens of lower index was added and balanced for sph3 and longitudinal color by varying only the surface curvatures. Subsequently, adding two more elements made a symmetric system /surface curvatures resulting in a near zero sph3, with color, coma, astigmatism aberrations, petzvall curvature, and distortion minimized. The lens optimized to the 50 mm focal length very well, however, the higher order aberrations degraded the spot diagram performance. The default merit function was used to optimize the RMS spot diagram performance. Less than 2-micron radius geometric precision was achieved.

The imaging lens was designed in the same way as the objective lens. Using these two designs the collimating lens design was started by first letting the surfaces of a triplet vary until a reasonable solution was attained. Again, the same procedure was followed as for the first two lenses, first taking care of the third order aberrations, and then using the default merit function to minimize the RMS spot size. All the surfaces and thickness of the system were allowed to vary

giving some reasonable bounds. A diffraction-limited system was reached, and tolerance and estimates from vendors were attained. The lens system is shown in Figure 3-12.

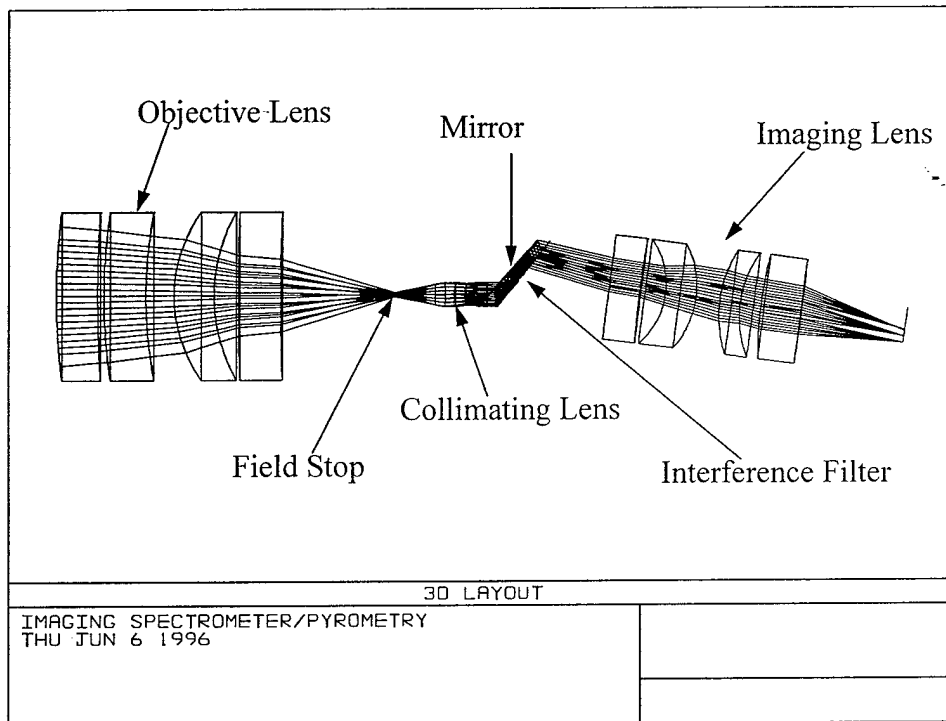


**Figure 3-12:** Lens design for the fourth reflected ray through the interference filter

As was mentioned earlier, to build these lenses from scratch would cost a great deal of money. Consequently, for this research, off-the-shelf components were used to accomplish the design. After this system is calibrated as discussed in the next chapter, the four colors are collected using an IR focal plane array. For high-speed applications, it is both important to use a sensitive detector as well as to get as much energy through the system as possible. For the detector, it is evident that an Indium Antinomite (InSb) snapshot infrared array would give the best performance for this application. The next step is to determine the available optical energy and analyze the limitations of radiometric detection of thermal energy for each filter.

### 3.4. Radiometry

To obtain the required scene information, the signal-to-noise-ratio must be determined. This can be done by looking at one filter at a time to estimate the accuracy of measuring the temperature with an assumed surface emissivity. After these signal characteristics are determined, the limitations of this system can be found. Starting with the assumption that the surface acts as a graybody, it will follow Planck's radiation law:

$$L_q = \frac{2\epsilon c_1}{\lambda^4 \pi (e^x - 1)} , \quad (3-1)$$

in photons/second·area·solid angle, where

$c$  = velocity of light =  $2.9979 \times 10^8$  m/s,

$\lambda$  = wavelength = 3.0 -3.4, 3.3-3.8, 3.8-4.2, 4.5-5.0  $\mu\text{m}$ ,

$x = hc/k_B \lambda T = 14388 \mu\text{m-K} / \lambda T$ ,

$h$  = Planck's constant =  $6.624 \times 10^{-34}$  Js,

$k_B$  = Boltzmann's constant =  $1.38 \times 10^{-23}$  J/K, and

$T$  = temperature = 525 K ( $\sim 250^\circ\text{C}$ ),

$\epsilon$  = emissivity = 0.2.

Given these parameters,  $L_q = 2.8 \times 10^{17}$  photons/sec·cm<sup>2</sup>·sr. The photon flux from the surface of emissivity,  $\epsilon$ , and area,  $A_p$ , to the collection optics of area,  $A_o$ , separated by distance,  $R$ , is

$$N_q = \frac{\epsilon L_q A_p A_o}{R^2} . \quad (3-2)$$

Since radiance is conserved, it is equivalent to write

$$N_q = \frac{\varepsilon L_q A_d A_0}{f^2} = \frac{\varepsilon \pi L_q A_d}{4 \left( \frac{f}{\#} \right)^2} \quad (3-3)$$

For the  $F/\# = 2.3$  system developed in this effort, with a detector area of  $.000009 \text{ cm}^2$  and a nominal emissivity<sup>43</sup> of 0.2 (assuming no wavelength-dependence),  $N_q = 3.3 \times 10^{11}$  photons/second. To calculate the total signal at the detector, a total system transmittance,  $t = 0.5$ , an integration time,  $t_{\text{int}} = 5 \text{ } \mu\text{s}$ , as well as a detector quantum efficiency of  $\eta = 0.80$ , (typical for our InSb detector) are included. This gives a total signal of  $6.6 \times 10^5 \text{ e}^-$  per InSb detector. As this situation is clearly background noise limited, the total noise in electrons will be the quadratic sum of the photon noise and the read noise ( $\sigma_{\text{read}}$  is taken here to be  $120 \text{ e}^-$ ):

$$\begin{aligned} \sigma_{\text{noise}} &= \sqrt{\sigma_{\text{shot}}^2 + \sigma_{\text{read}}^2} \\ &= \sqrt{8.44 \times 10^5 + 120^2} = 916 \text{ e}^- \end{aligned} \quad (3-4)$$

and the signal to noise ratio is  $6.6 \times 10^5 / 916 = 720$  or about 0.1%. This is a good result because the algorithm used to fit temperature remain accurate to a few degrees even if there is much larger amounts of noise. The high-speed pyrometer was built and tested for accuracy, the details of which is presented in the next chapter.

## **4. High Speed Pyrometer Fabrication**

The hardware discussed in the last chapter was assembled using primarily off-the-self components. In this chapter, the mechanical assembly for the high-speed instrumentation will be discussed. In addition, the experimental setup, calibration instrumentation, and test procedure will be detailed. The testing of this system consists low speed validation tests to characterize camera performance.

### **4.1. Multi-spectral Camera**

The first step to assembling the camera components was to select a focal plane. In the munition test environment, the objects that are being analyzed are moving at MOCH-one or greater and stop-motion resolution is required to about one-millimeter. Consequently, the requirement is that the camera shutter-down to one microsecond or better. After a survey of the IR cameras that could potentially meet this requirement, the Amber AE173 snapshot was selected. The optics for the front end of the camera was built as discussed in the previous chapter, and is shown in Figure 4-1.

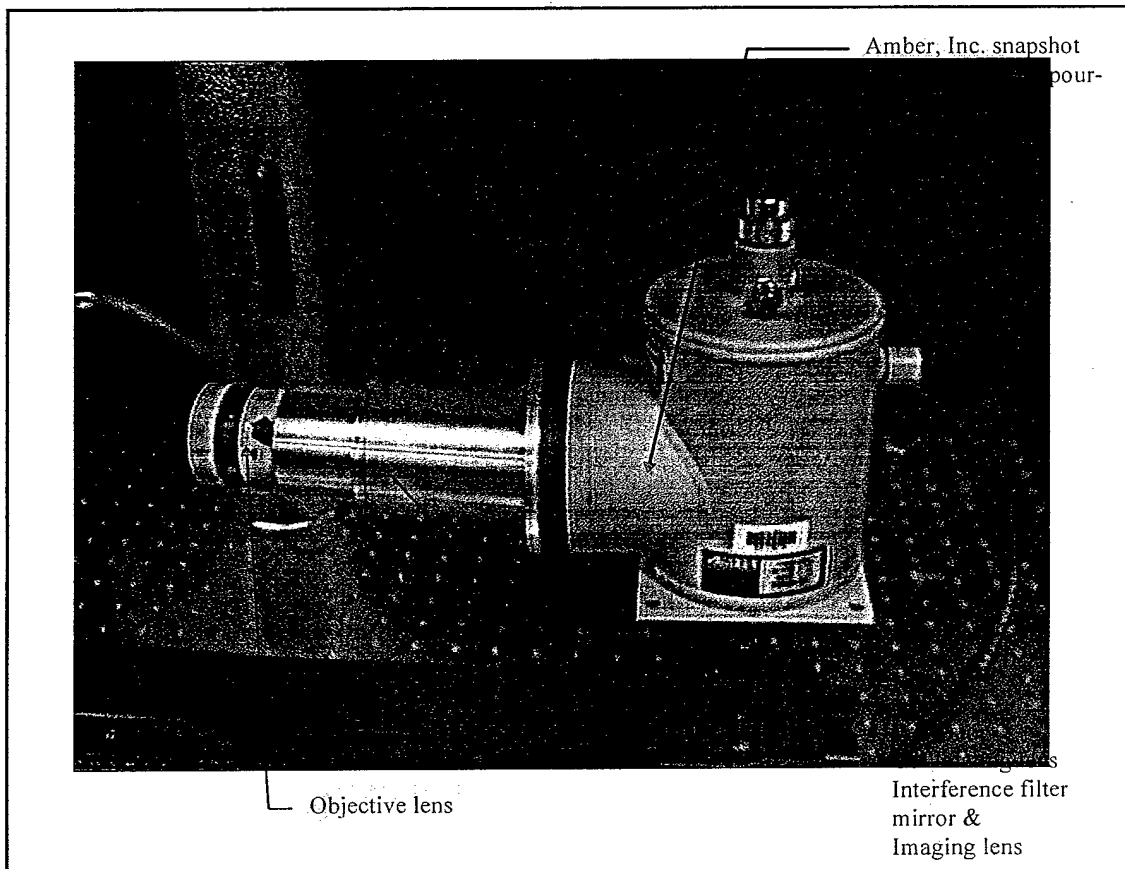


**Figure 4-1:** High speed pyrometer camera configuration. The lens assembly is at a slight angle from the front face of the camera, which is done to incorporate the unique lens design

The lens assembly is mounted to the Amber Camera with four bolts and can be removed easily for component inspection. All components hard mount and the only part that moves is the objective lens for focusing. The objective lens mounts in the same clamp as the front end of the Amber camera making it simple to interchange lenses for alternative applications. After detaching the filter assembly from the camera face, the imaging lens can be seen. Figure 4-2 shows how the imaging lens fits in the standard Amber front lens mount. The filter assembly mounts in existing lens mounting holes, thus avoiding modification of the camera.

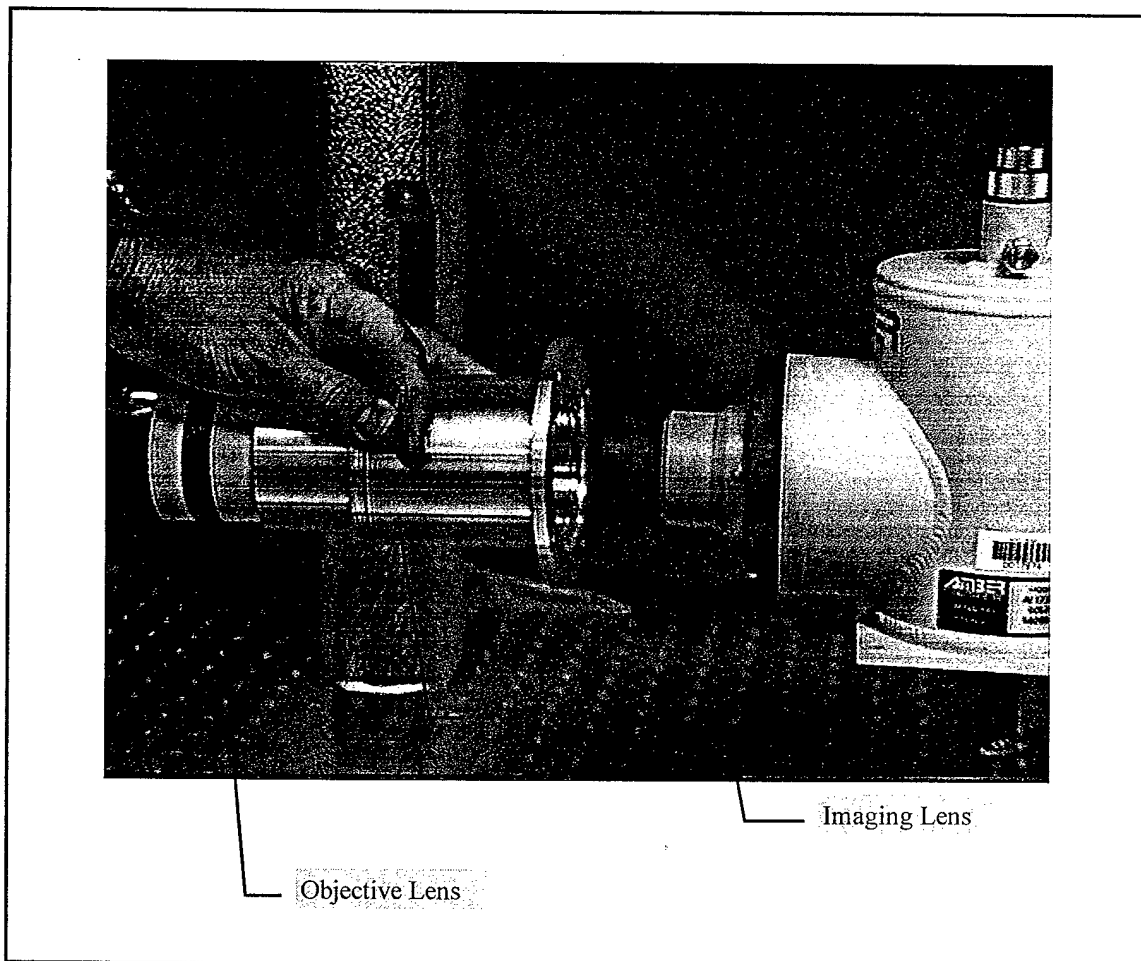


**Figure 4-2:** Disconnection of filter assembly from main camera body. The assembly is held to the front face of the camera via four mounting bolts. The imaging lens fits in the standard Amber mount in the front of the camera. Both the objective and imaging lenses were manufactured by DIOP.

After removing the filter assembly from the camera, inspection of the interference filters is made by looking through the back end. Just on the other side of the filters the mirror can also be inspected. The filter/mirror combination is secured to the tubular housing with two Phillips head screws. A picture of the back end view is shown in figure 4-3.

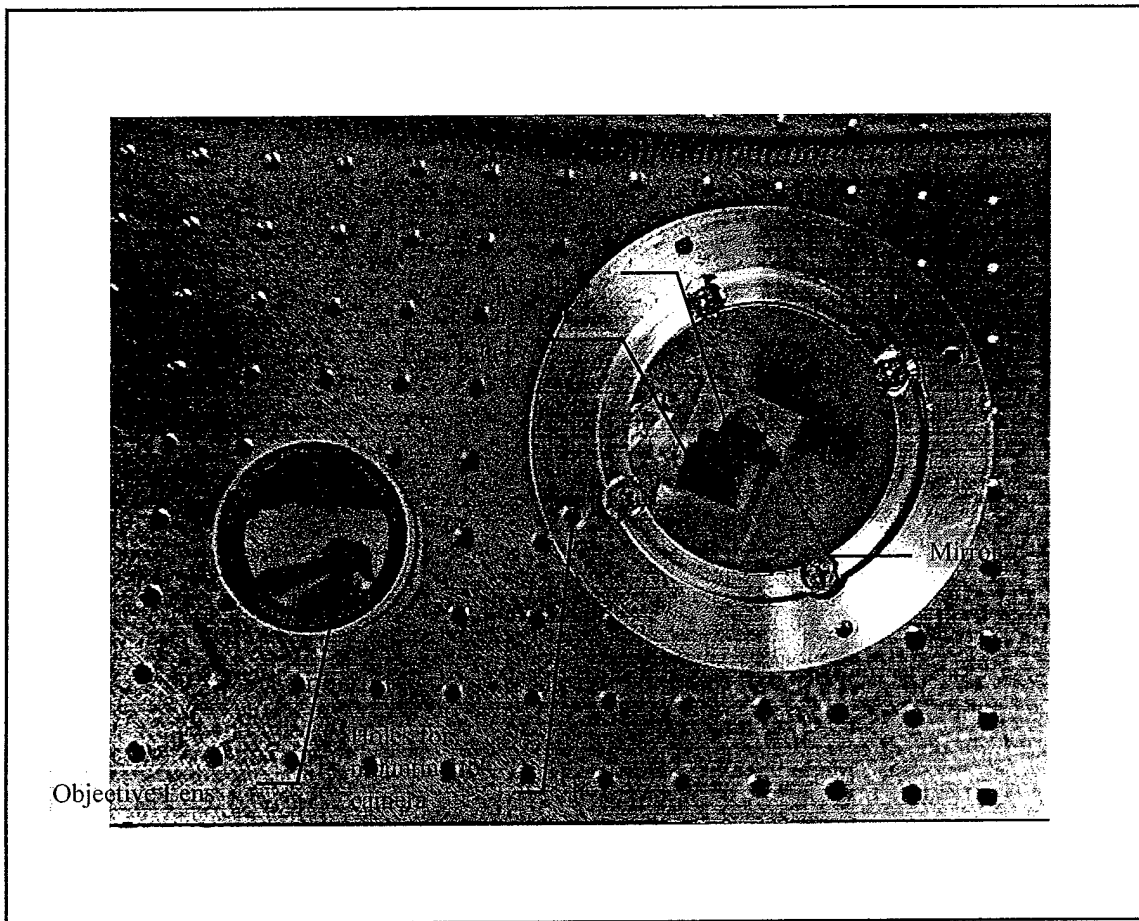


**Figure 4-3:** Interference filter and mirror. The mirror that folds the multiple beams back towards the interference filters can be seen through the small hole directly above the filters. On the other side of this assembly are the collimating lens and the field stop.

The field stop may be seen by turning the filter assembly around and detaching the objective lens. The field stop consists of two razor blades fashioned inside the front end of the filter tube (Figure 4-4). The objective lens connects to a mounting flange on the front of the filter tube so that an image will form on the field stop. Focusing for the entire system is done by way of the “built-in” focusing property of the objective lens.

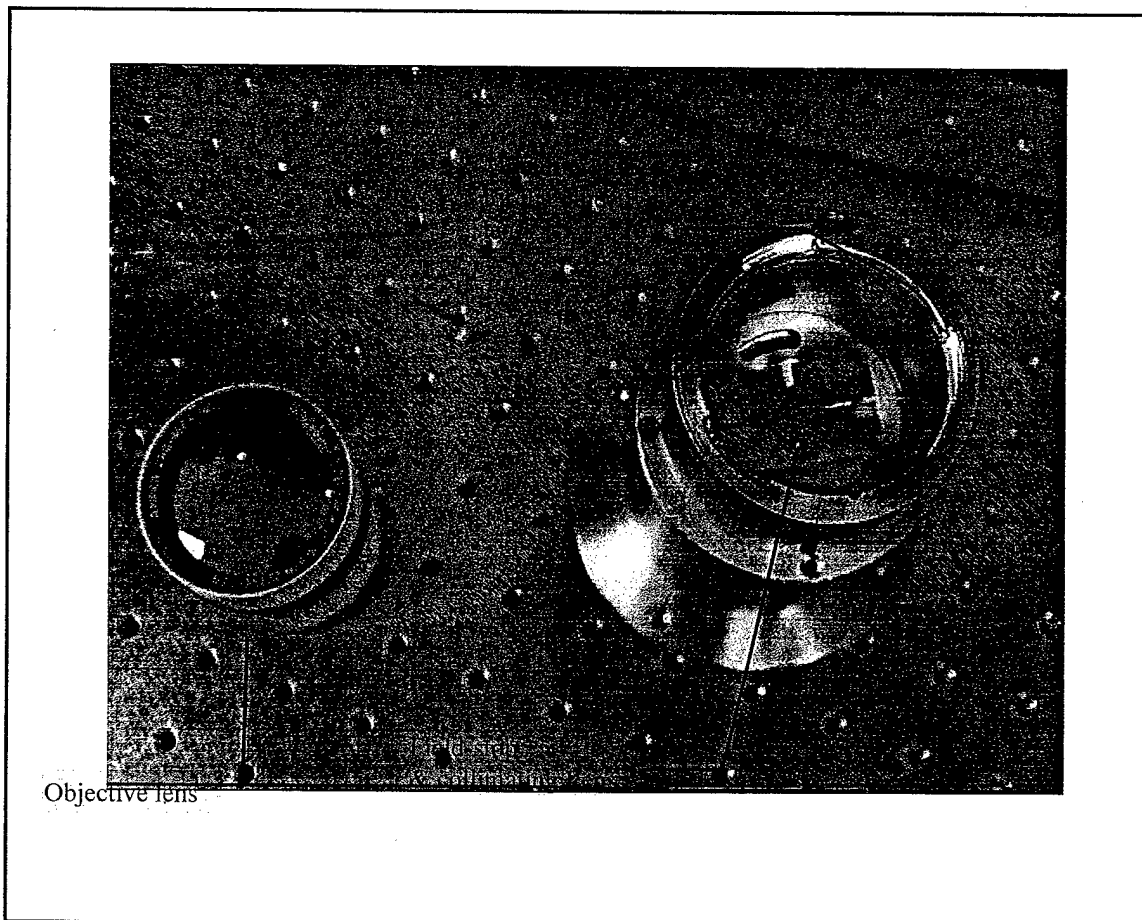


**Figure 4-4:** Field-stop and collimating lens. The collimating lens is between the interference filters and the field-stop and consequently cannot be seen in either view. The field-stop is made from two razor blades.

To validate the pyrometer performance fairly accurately, control was needed over the temperature of the test metal. This could not be done with any accuracy at high speeds, consequently, low speed validation was implemented. The temperature of the sheet metal was controlled by pasting the metal samples to an extended blackbody using heat sink compound. The arrangement is shown in Figure 4-5.

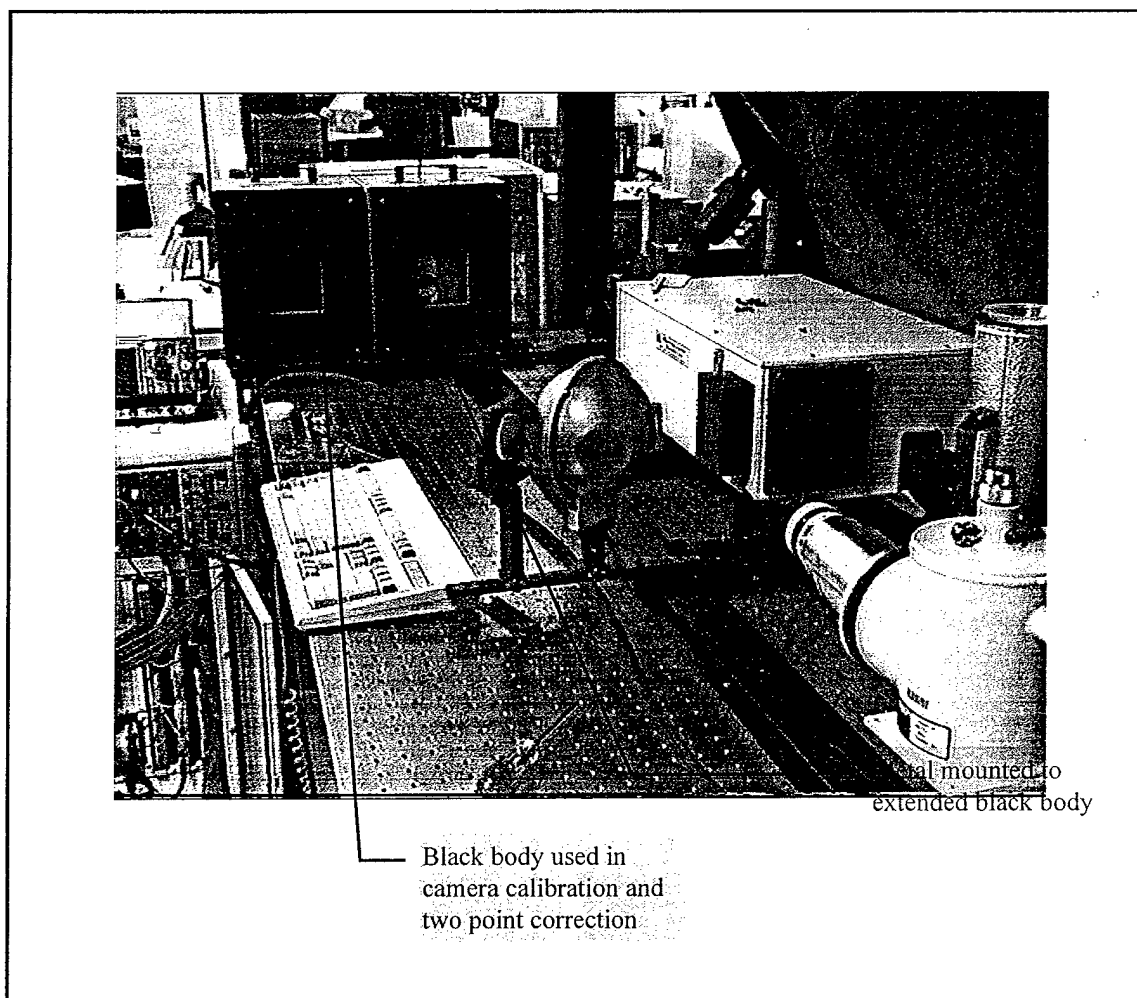


**Figure 4-5:** Experimental test item and black body used in system calibration

With temperature accurately known, the emissivity could be accurately determined. This setup was also used to predict temperature for the four spectral measurements. The temperature predicted was accurately compared to the true temperature reading of the blackbody controller. In addition, a thermocouple was mounted to the front surface of the metal sample so that there was an additional check for true temperature.

## 4.2. Calibration:

After the pyrometer camera components were assembled, the next step was to design a calibration procedure. The calibration is broken up into two parts: calibration of the spectral transmission of each of the four-color images and calibration of the gain and offset of the InSb detector. Several techniques for determining the filter transmission characteristics were examined including imaging an extended blackbody and gathering spectral data at many different temperatures. As in the problem of determining temperature from a system of equations generated from multiple spectral measurements, a system of equations from multiple temperature measurements can also be solved to give the spectral transmission for each of the filtered images. It turned out that the matrix describing the system of equations is highly singular and as a result predicting the filter transmission is not very accurate. Consequently, the brute force technique of sweeping a monochromator through wavelength was chosen. The setup is shown in Figure 4-6.

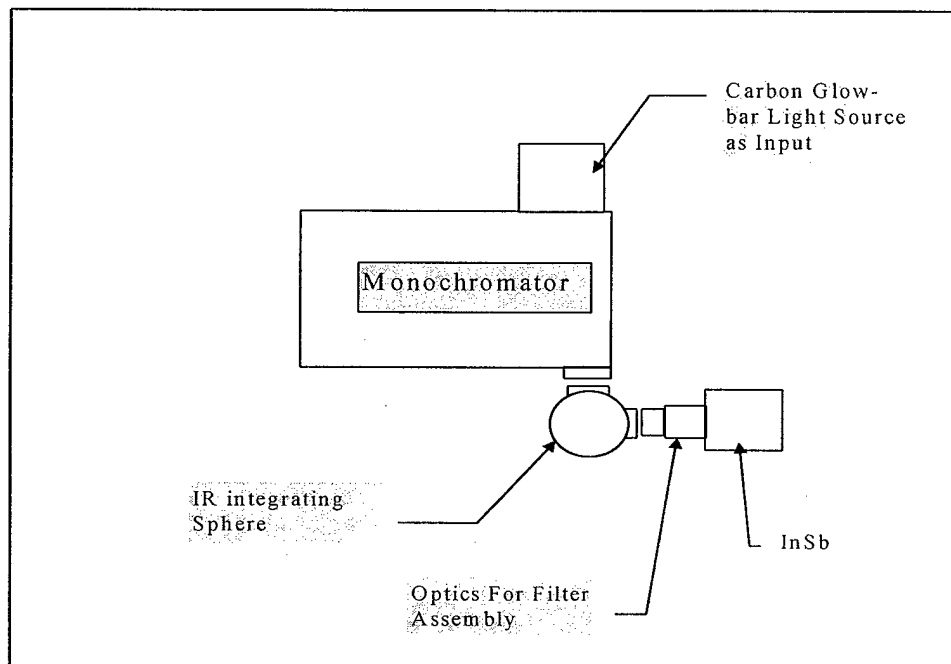


**Figure 4-6:** Calibration setup

An Acton Research Inc. SpectroPro 500 monochromator was controlled with the system computer and stepped through 500 values of wavelength from 2700 to 5200 nanometers in 5

nanometer increments. An integrating sphere was used at the output of the monochromator to flat field the detector. Using the monochromatic data and an extended blackbody the calibration of the system filters was done in two steps. The first step is to determine the spectral response (per-cent transmission) of each detector on the array. The detector responsivity, transmission of the optics, transmission of the filters, transmission of the integration sphere, transmission of the atmosphere, and the spectral characteristics of the monochromator all, affect the perceived optical energy, Eq. 4-1.

$$\Phi(\lambda) = \tau_{opt}(\lambda)\tau_{filters}(\lambda)\tau_{int\ sph}(\lambda)\tau_{atm}(\lambda)L_{mono}(\lambda)\Omega a_{det} \quad (4-1)$$

Determining each of the above system parameters is quite involved. However, since the filter transmission can be determine from the relative response for each of the four filters we only need to determine the relative signal amplitude before and after the filters are placed in the system. Equation 4-2 represents the percentage transmission for each of the spectral regions. To relate the energy on the detector to the IR energy leaving the metal surface the second step of calibration needs to be performed, gain and offset.

$$\frac{\Phi_{w/ filters}(\lambda)}{\Phi_{no/ filter}(\lambda)} = \frac{\tau_{opt}(\lambda)\tau_{filters}(\lambda)\tau_{int\ sph}(\lambda)\tau_{atm}(\lambda)L_{mono}(\lambda)\Omega a_{det}}{\tau_{opt}(\lambda)\tau_{int\ sph}(\lambda)\tau_{atm}(\lambda)L_{mono}(\lambda)\Omega a_{det}} = \tau_{filters}(\lambda) \quad (4-2)$$

In order to get the correct values for a material's radiant exitance, the gain and offset of the entire system needs to be determined. Since the data from each detector is digitized, the output is in analog digital units (ADU). Neglecting atmospheric transmission the equation is

$$ADU = OFFSET + \tau_{filter}(\lambda)L_{source}(\lambda)\Omega A_{det}\epsilon(\lambda)G. \quad (4-3)$$

where G is the gain in ADU's per watt. If the systems solid angle is folded into the gain there are only two unknown constants in the system, gain and offset. Collecting data for an extended blackbody at a high and a low temperature will form two equations and the gain and offset can be

calculated. Gain and offset can only be done after the filter transmission is characterized. Innately there was some problem in this calibration.

The manufacture's power supply for the monochromator light source proved to be too noisy to accomplish an accurate calibration. In addition, the power in the laboratory had as much as  $\pm 10$  volts fluctuation adding additional noise. To overcome these problems the power supply was replaced, and testing was done after normal duty hours, when the AC power was more predictable. Figures 4-7 and 4-8 show the fluctuation before and after the above correction were made.

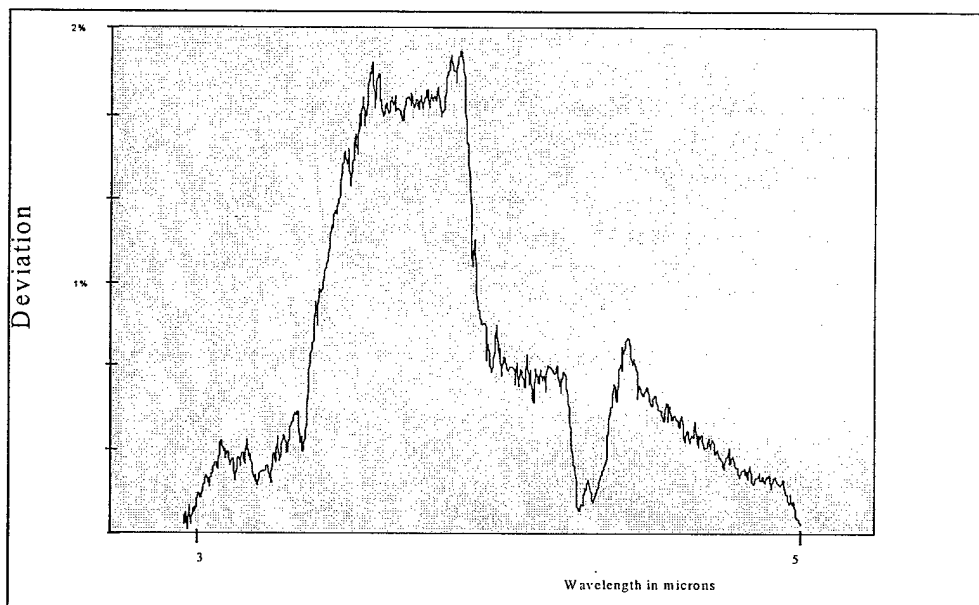


**Figure 4-7:** Error of monochromator from calibration run to calibration run. This data was taken during normal working hours and with the manufacture's power supply.

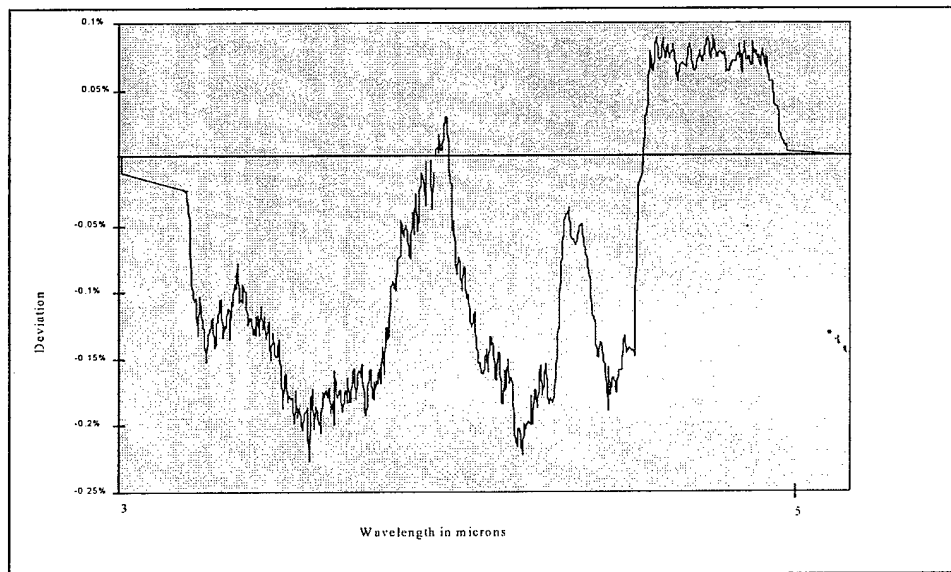


**Figure 4-8:** Error of monochromator from calibration run to calibration run. This data was taken after normal working hours and with a Power One Inc., F15-15-A power supply.

Along with the power fluctuations, the room temperature also fluctuated. This caused the temperature of the optics to fluctuate, and, consequently, the DC offset of the background signal to vary. This problem was overcome by masking off, at the field stop, one line of the array from external radiation (Figure 4-9). These detectors could only see the radiation of components to the right of the field stop. Since all detectors on the array will fluctuate in proportion to this background, the masked detectors were monitored to compensate for the thermal variation of the optics during calibration.

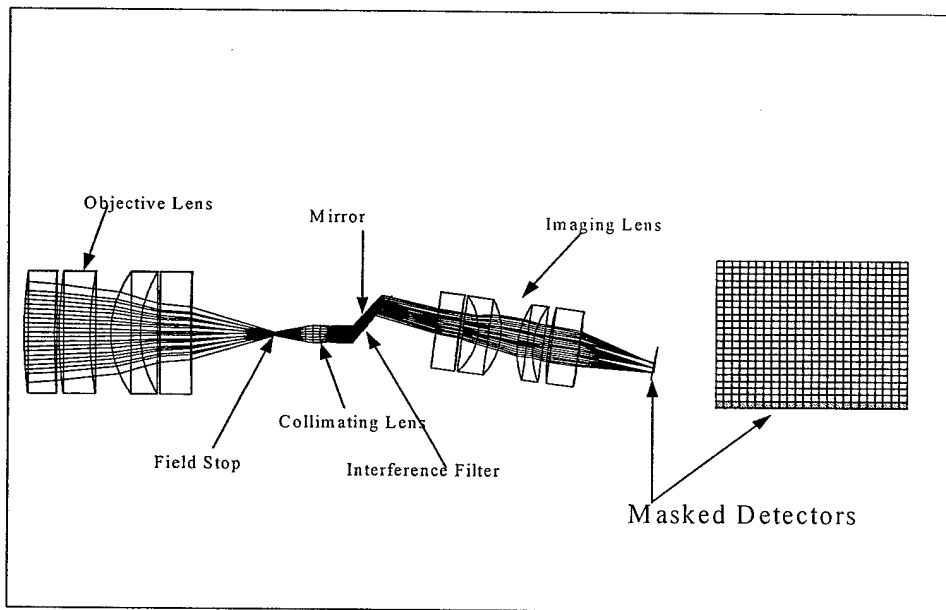


**Figure 4-9:** Detector masking approach to remove the affect of thermal variation caused by air-conditioning in laboratory. These fluctuations were as much as 2% over a single calibration run.

After the fluctuation in background was normalized the two calibration runs were made, one with the filters and one without. Using equation 4-2 the transmission for each of the images could be computed (figure 4-10).

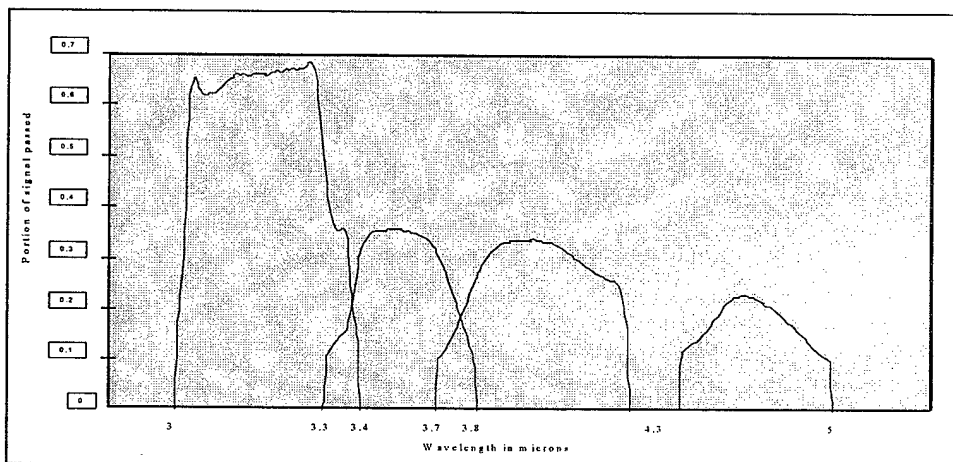


**Figure 4-10:** The filter bandpass response for each of the four filters. The first pass corresponds to the first filter on the left, the second pass is the second filter, and so forth. Notice that each of the filters peak response is gradually decreasing. This corresponds primarily, to out-of-band absorption.

In the design for the filter set above, the goal was to use as much of the overall 3 to 5 micron spectrum as possible while staying away from the  $CO_2$  notch. It can also be seen in figure 4-10 that for the transmission of images 2, 3, and 4 there is a degradation in the peak transmission. This is due to out of band absorption that can be removed with proper filter design.

### 4.3. Experimental Setup

After the pyrometer camera components were assembled and the filter transmission was characterized, the next step was to accomplish low speed validation testing to see if the theory agrees with reality. The setup is shown in Figure 4-11.

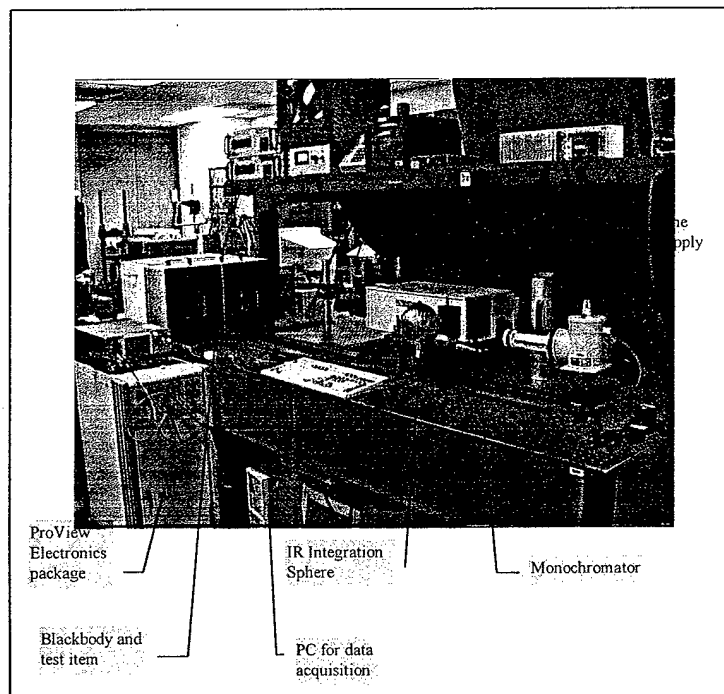


**Figure 4-11:** Test and calibration setup

The blackbody containing the test samples and the blackbody used for two point correction were mounted on a rail so that they may be slid in and out of the optical path quickly. Three types of metal samples were mounted to the extended blackbody: copper, aluminum and

steel. The camera system collected numerous temperature data points for each of the samples to insure repeatability, the results of which will be presented later. The support electronics to the Amber camera system is the general purpose ProView unit (Figure 4-12). The ProView electronics provided camera clocking and A/D conversion of the analog data. After the data is acquired, the ProView relays the image information to the system computer and to its hard drive. The ProView unit comes with its own language (TDF) that is used to set system parameters such as timing, gain, offset, etc. The code for which is located in appendix B.

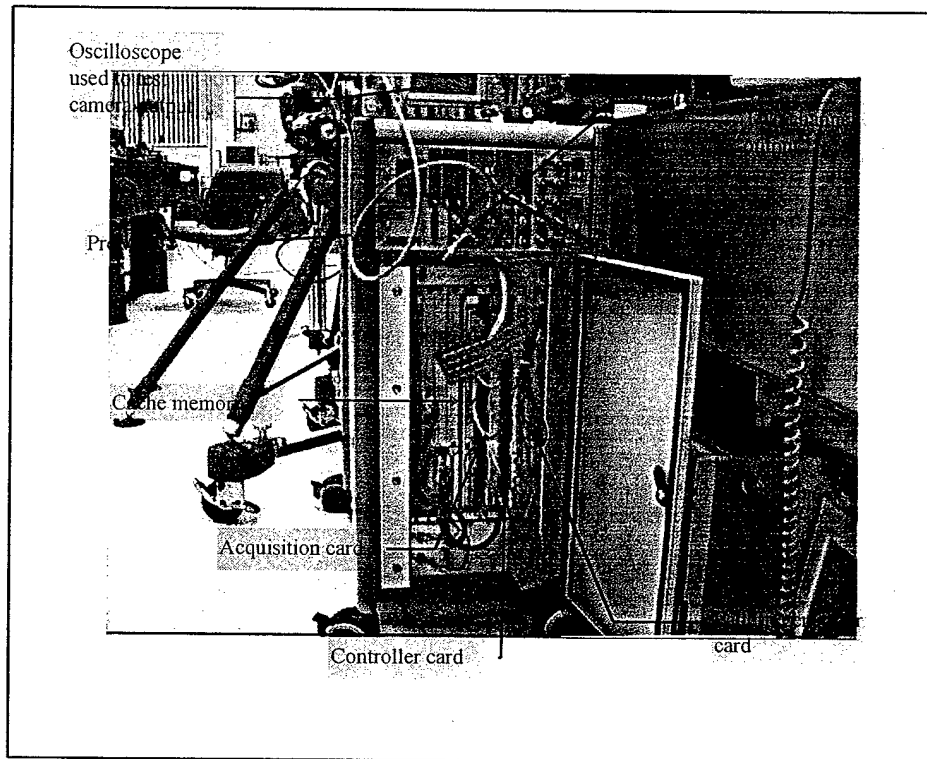


**Figure 4-12:** ProView electronics package

#### **4.4. Validation**

There were two means used to validate the calculated temperature. First the temperature of the sample on the blackbody was known (internal Thermocouple) from the control panel. This temperature was checked at the metal surface using an external thermocouple. In addition to the thermocouples, a commercial pyrometer manufactured by Agema Inc., was used to compare

results. This type of pyrometer uses the user input values for emissivity to compute temperature (picture shown in Figure 4-13). This camera was used primarily as a comparison of this new technology to a typical commercial product. When the emissivity calculated by the high-speed pyrometer was used in the AGEMA camera the temperature prediction was highly accurate. However this system relies on accurate prediction of an average emissivity over the 3 to 5 band.

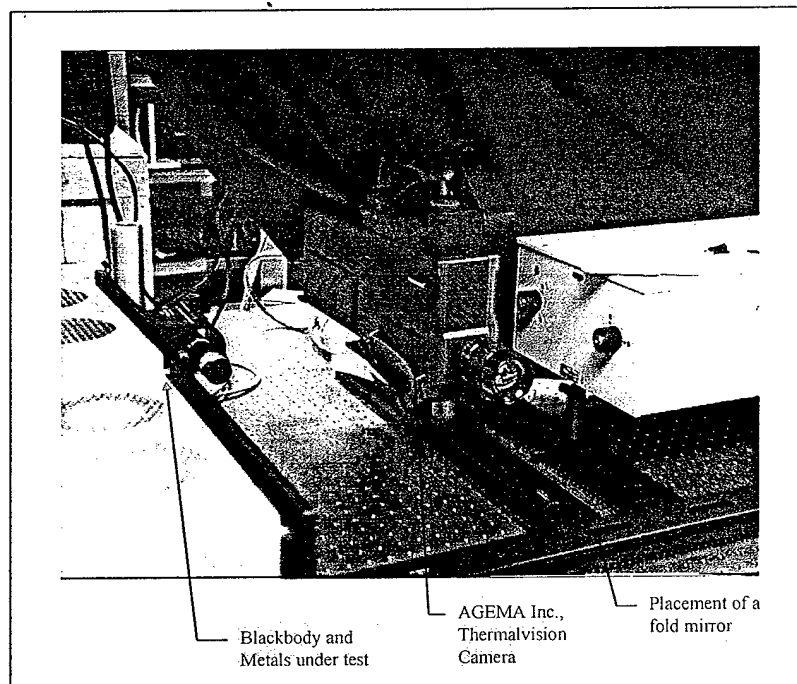


**Figure 4-13:** The AGEMA Thermo-vision IR camera used for validation.

The validation for the emissivity following a polynomial dependence was presented earlier and the purpose of the above instrumentation was to show that the system could predict temperature accurately. If the actual model for emissivity were different from a second-degree polynomial, the temperature prediction would have increasing error with increasing error between the two models.

#### 4.5. Results

After many measurements were made to insure repeatability, the results were plotted in Figure 4-14 through 4-17. It is interesting to note that all samples followed the same trend. As temperature was increased, the curvature for the emissivity profile flattened out, and the average emissivity rose. All the emissivity profiles were concave. The results for temperature prediction are shown in tables 4-1 through 4-4 for each of the metals.

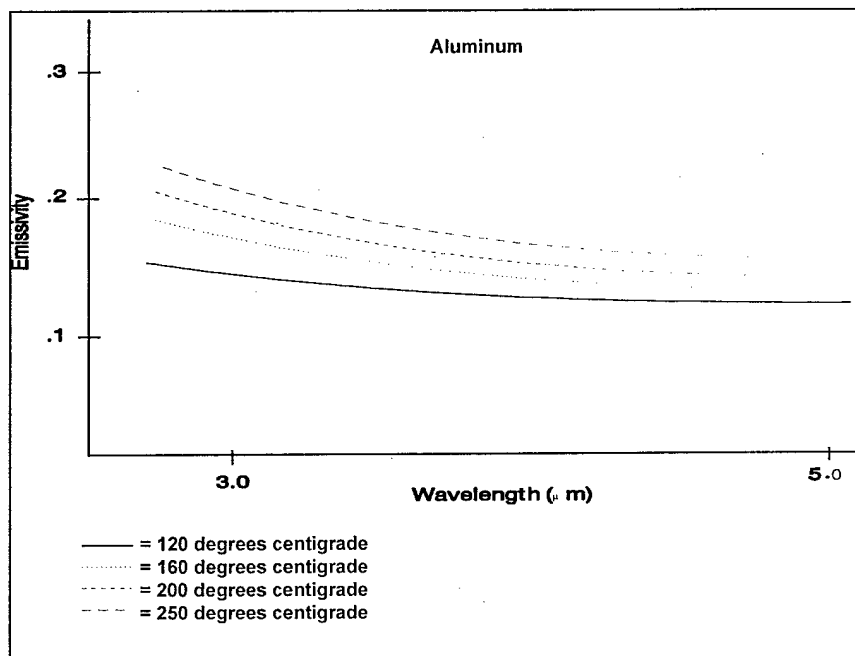


**Figure 4-14:** Plot of the emissivity of a heated piece of aluminum at various temperatures. The surface of the sample was prepared using 200 grit sandpaper.

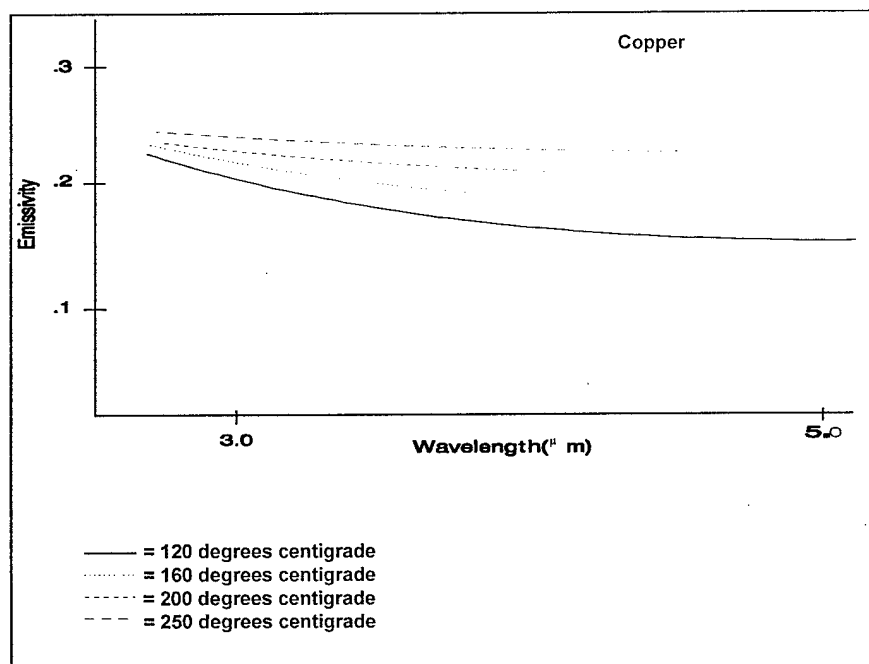


**Figure 4-15:** Plot of the emissivity of a heated piece of copper at various temperatures. The surface of the sample was prepared using 200 grit sandpaper.

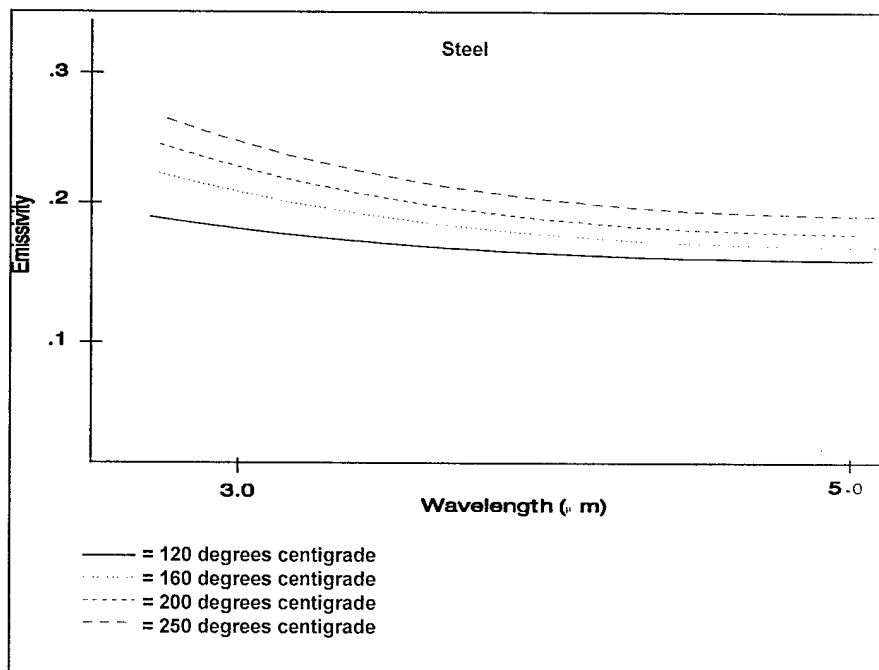


**Figure 4-16:** Plot of the emissivity of a heated piece of steel at various temperatures. The surface of the sample was prepared using 200 grit sandpaper.

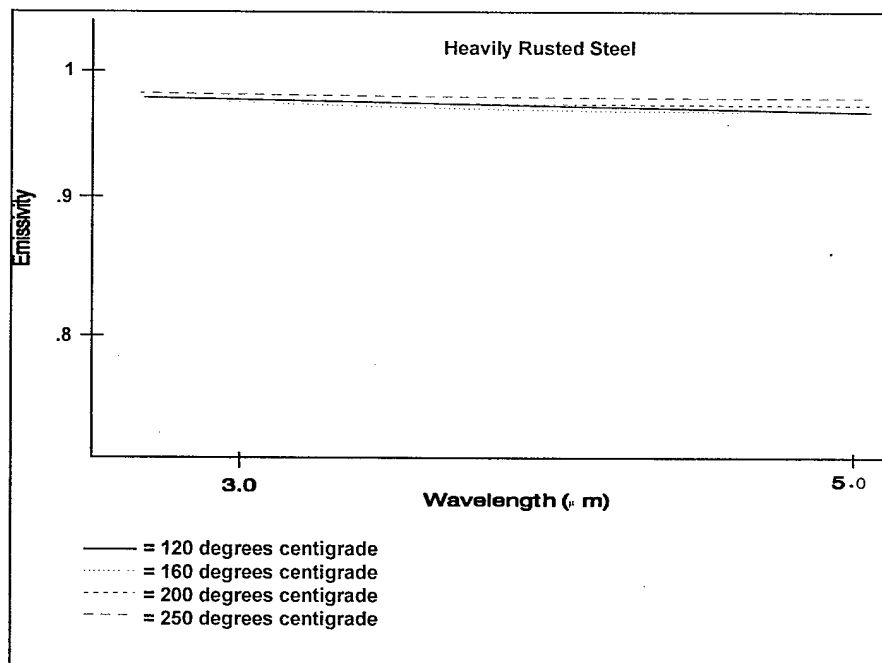


**Figure 4-17:** Plot of the emissivity of a heated piece of heavily oxidized steel at various temperatures.

True Temperature (°C)	Measured Temperature (°C)	Error (°C)
98.0	87	-11
102.2	102	-0.2
106.8	104	-4.8
109.9	107	-2.9
115.2	117	+1.8
118.6	119	+0.4
121.4	119	-2.4
125.0	125	0
129.2	132	+0.8
132.7	134	+1.3
132.8	134	+1.4
137.1	139	+1.9
141.2	136	-5.2
144.9	140	-4.9
148.7	145	-2.7
152.6	154	+1.4
155.1	158	+2.9
159.0	161	+2
163.4	164	+0.6
168.7	170	+1.3
172.1	168	-4.1
176.4	177	+0.6
181.2	180	-1.2
187.3	187	-.03
192.1	193	+1.1
195.6	197	+1.4
204.1	209	+4.9
212.5	220	+7.5
230.6	250	+19.4
250.1	270	+19.9

**Table 4-1:** Temperature error of Aluminum Sample

True Temperature (°C)	Measured Temperature (°C)	Error (°C)
102.0	98	-4
106.3	102	-4.3
107.1	103	-4.1
109.5	107	-2.5
112.5	110	-2.5
115.6	113	-2.6
119.8	119	-0.8
123.0	120	-3.0
128.4	127	-1.4
132.8	134	+1.2
136.0	134	-2.0
140.2	138	-2.2
144.6	143	-1.6
148.9	147	-1.9
152.0	151	-1.0
158.1	158	-0.1
166.1	167	+0.9
169.9	170	+0.1
172.1	174	+1.8
177.8	179	+2.2
182.3	180	-2.3
189.9	192	+2.1
192.7	195	+2.3
198.8	203	+4.2
204.0	207	+3.0
210.0	214	+4
225.5	227	+1.5
245.5	239	-6.5
255.0	265	+10
278.1	270	-8.1

**Table 4-2:** Temperature error of Copper Sample

True Temperature (°C)	Measured Temperature (°C)	Error (°C)
108.1	105	-3.1
116.4	114	-2.4
116.5	114	-2.5
119.1	115	-4.1
124.6	122	-2.6
127.8	126	-1.8
130.2	132	+1.8
135.8	133	-2.8
139.0	137	-2.0
143.2	142	-1.2
146.3	145	-1.3
147.2	147	-0.2
149.2	150	+0.8
151.8	154	+2.2
154.7	154	-0.7
158.3	158	-0.3
162.5	163	+0.5
164.9	162	-2.9
167.8	166	-1.8
169.2	172	+2.8
172.2	173	+0.8
174.4	176	+1.6
177.8	179	+1.2
180.2	184	+3.8
183.2	185	+1.8
185.6	185	+0.6
189.7	192	+2.3
193.2	197	+3.8
197.1	199	+2.9
204.5	207	+2.5

**Table 4-3:** Temperature Error of Steel

True Temperature (°C)	Measured Temperature (°C)	Error (°C)
108.2	108	-0.2
116.6	116	-0.6
116.8	117	+0.2
119.3	119	-0.3
124.7	125	+0.3
127.9	128	+0.1
130.4	130	-0.4
135.9	136	+0.1
139.2	140	+0.8
143.4	144	+0.6
146.6	146	-0.6
147.4	147	-0.4
149.4	149	-0.4
151.9	152	+0.1
154.8	154	-0.8
158.3	158	-0.3
162.6	163	+0.4
164.8	166	+1.2
167.8	167	-0.8
169.3	170	+0.7
172.6	172	-0.6
174.5	174	-0.5
177.9	178	+0.1
180.3	180	-0.3
183.4	184	+0.7
185.7	186	+0.3
189.9	191	+1.1
193.1	193	-0.1
197.1	198	+0.9
204.7	205	+0.3

**Table 4-4:** Temperature Error of Oxidized Steel

Nearly all the calculation errors were within  $\pm 5$  °C. At high temperatures there was a significant error. This was possibly due to the fact that the heat sink compound is not designed for use at temperatures in excess of 200 °C.

The singular value decomposition code was used to reconstruct temperature and essentially the same results were attained as for Gaussian elimination. There was, however, a slight degradation in predicting temperature, and the SVD method achieved an accuracy of about  $\pm 8$  °C. This additional error is most probably due to rounding errors associated with the more complex algorithm execution. I believe with some careful work, the code could be improved to attain the same accuracy as Gaussian elimination.

For the Levenberg and Marquardt nonlinear optimization, again, the accuracy was somewhat degraded from the Gaussian elimination method, seeing an accuracy of  $\pm 25$  degrees error. In addition, the error was highly subject to the accuracy of the seeding algorithm. It is possible that the code is becoming hung up in local minimums. Another problem is that with flat emissivity profiles, the algorithm does not work very well at all. This was seen for the heavily oxidized sample, where the error was several hundred °C.

## 5. Conclusions

The determination of the temperature of an object through the use of only passive radiation has, in the past, been met with ambiguous results. The primary problem is to separate the combined effects of emissivity and temperature on the spectral radiance. This research has shown that determining the temperature of metals is achieved with a model for emissivity as second order polynomial dependence with wavelength. This model was developed from a physics-based approach with the understanding that the free electrons, Fresnel surface reflections and surface topography have a combined contribution to emissivity. This model was validated and shown to be accurate for the metal found in weapon testing. This physical model allows a flexible way to determine a metal's emissivity, and as material parameters change, the new wavelength dependent model can be quickly determined.

It is both important to assume an accurate functional form for the emissivity, as well as develop instrumentation that can accurately acquire the radiance data. Since emissivity and temperature have functional dependencies on wavelength, the use of multi-spectral instrumentation is predicated. To measure emissivity and temperature to the required accuracies, a special high-speed IR imaging spectrometer was needed. Using the knowledge that the emissivity takes the form of a second degree polynomial, in addition to assuming that the object's temperature is in steady state and thus its temperature dependent spectral behavior follows the Planck distribution, an IR spectrometer capable of measuring four spectral regions was developed and tested. Utilizing a common set of optics and a single interference filter allowed efficient simultaneous collection of all spectral information extremely fast. This pyrometer was shown to remain calibrated for long periods of time, and having no moving parts, this system is very rugged and normal handling does not alter calibration. The pyrometer proved to be accurate within  $\pm 5$  degrees, for temperatures ranging from 100 to 200 degrees centigrade. Due to the laboratory experimental setup, it was not possible to test the system at higher temperatures; however, it is not anticipated that the system would degrade much, or even at all, until the material started to melt or burn.

Up to this point, experimental verification for munition models has only been performed for object deformation, crystal lattice realignment, and total heat energy conversion. Additional experimental measurements of object radiation profiles must be performed to accurately validate the manner in which temperature is incorporated into these new models. Specifically, point-to-point positions on an object must be mapped, first in terms of that object's radiance, and subsequently in terms of the object's emissivity and temperature. Specific characteristics of the energetic environment give rise to difficulties when attempting to deduce temperature and emissivity from measured radiance. These difficulties are due to the fast motion and high rate of temperature change of the objects. Temperature is typically changing on the order of hundreds of degrees per millisecond, while motion occurs at typical velocities of 1000 feet per second. The accuracy of the pyrometer of this dissertation will not suffer from the dynamic nature of the energetic environment and, consequently, is the perfect tool to be used to validate the empirical calculations of the munition code simulations.

The next step in this research is science only limited detail was given to substantiate the effect of surface topography on emissivity a detailed analysis needs to be done. In the literature there is an indication that diffraction through the surface may provide significant insight in describing the wavelength dependent emissivity for many materials. It appears that incorporating this effect into the overall model for emissivity is rich for development. In addition to a more complete model for emissivity work needs to be done to simplify the lens design and find a lower cost substitution for the Amber Inc. camera. The objective here is to lower the cost of the overall system to compete with other off-the-shelf single color pyrometers. In addition, further work needs to be done to characterize the emissivity of other materials of interest. After emissivity is characterized, the correct algorithm can be selected, and system accuracy analyzed. When the imaging spectrometer of this dissertation is used with an accurate emissivity model a highly accurate and low cost optical pyrometer will be created, suited perfectly for high-speed industrial applications.

## Appendix A-Temperature Estimation Software

The programs contained herein are those written to process the raw data and output the estimated temperature. There are basically two programs, a gain and offset procedure and the main data reduction procedure. The main data reduction procedure consists of the Gaussian reduction, singular value decomposition and Levenberg-Marquet solutions to fitting the four color data.

There are three function calls that accomplish the inversion using LU-decomposition to implement Gaussian elimination; MatbsD%, MatInvD% and MatluD%. An LU matrix is an upper triangle matrix (one with all non-zero entries on or above the main diagonal) and can be solved immediately. The goal of Gaussian elimination is to transform a non upper triangle system into an equivalent triangular one.

MatbsD% takes a matrix in LU form, found by matluD%, and a vector b and solves the system  $Ux=Lb$  for x. matrices A,b,x are double precision. Parameters: LU matrix in A, corresponding pivot vectors in rpvt and cpvt, right side in b Returns: solution in x, b is modified, rest unchanged

MatInvD% uses the matluD% and matbsD procedures to invert a square, double precision matrix. Let  $e(N)$  contain all zeroes except for the jth position, which is 1. Then the jth column of  $A^{-1}$  is x, where  $Ax=e$ . Parameters: A(n x n) matrix Returns:  $A^{-1}$

MatluD% does Gaussian elimination with total pivoting to put a square, double precision matrix in LU form. The multipliers used in the row operations to create zeroes below the main diagonal are saved in the zero spaces. Parameters: A(n x n) matrix, rpvt(n) and cpvt(n) permutation vectors used to index the row and column pivots Returns: A in LU form with corresponding pivot vectors; the total number of pivots in count, which is used to find the sign of the determinant.

## A1. Gain And Offset Acquired Data Program:

### Main routine

```
DECLARE SUB gainoff (a#(), BBmes!(), MLbb!(), MLmes!(), tlow!, tmed!, thigh!, temp#)
DECLARE SUB calcML (a#(), MLbb!(), MLsamp!(), temp#(), temp1#())
DECLARE SUB getbbdata (FILTERMAX!, BBmes!(), MLmes!())
DECLARE SUB Normalize (a#())
DECLARE SUB PLOTDATA (a#())

DIM SHARED o AS STRING * 1
DIM SHARED ML#(4, 10)
COMMON SHARED DLAM#, FILTERMAX, LAMMAX#(), LAMMIN#(), EMISS#, c1#, c2#, c3#
SCREEN 9
CLS
c1# = 3.7415 * 10 ^ 4
c2# = 1.43879 * 10 ^ 4
c3# = 1.88365 * 10 ^ 23

DIM a#(5, 500), BBmes(4, 10), MLbb(4, 10), MLmes(4, 10), MLsamp(4, 10), temp1#(10), temp#(10)
DIM LAMMIN#(5), LAMMAX#(5)
EMISS# = .9
FILTERMAX = 4
DLAM# = .005
LAMMIN#(1) = 2.7
LAMMAX#(1) = 5.2 - DLAM#
LAMMIN#(2) = 2.7
LAMMAX#(2) = 5.2 - DLAM#
LAMMIN#(3) = 2.7
LAMMAX#(3) = 5.2 - DLAM#
LAMMIN#(4) = 2.7
LAMMAX#(4) = 5.2 - DLAM#
LAMMIN#(5) = 2.7
LAMMAX#(5) = 5.2 - DLAM#

CALL Normalize(a#())
CALL PLOTDATA(a#())
CALL calcML(a#(), MLbb(), MLsamp(), temp#(), temp1#())
CALL getbbdata(FILTERMAX, BBmes(), MLmes())

tlow = 1
tmed = 3
thigh = 6

CALL gainoff(a#(), BBmes(), MLbb(), MLmes(), tlow, tmed, thigh, temp1#(tmed))

END

SUB calcML (a#(), MLbb(), MLsamp(), temp#(), temp1#())

temp#(1) = 98.6 + 273
temp#(2) = 108.4 + 273
temp#(3) = 117.8 + 273
temp#(4) = 129 + 273
temp#(5) = 137.9 + 273
temp#(6) = 149.4 + 273
temp#(7) = 149.4 + 273
temp#(8) = 1156 + 273
temp#(9) = 168.7 + 273
temp#(10) = 169.3 + 273

FOR t = 1 TO 10
FOR filter = 1 TO FILTERMAX
MLOLD# = 0
I = 0
FOR lam# = LAMMIN#(filter) TO LAMMAX#(filter) STEP DLAM#
I = I + 1
R# = a#(filter, I)
```

```

MLbb# = c1# / (lam# ^ 5 * (EXP(c2# / (lam# * temp#(t))) - 1)) * EMISS#
MLbb(filter, t) = MLbb# * R# * DLAM# + MLOLD#
MLOLD# = MLbb(filter, t)
NEXT lam#
'PRINT MLhigh#(filter)
NEXT filter
NEXT t

temp1#(1) = 108 + 273
temp1#(2) = 119 + 273
temp1#(3) = 140 + 273
temp1#(4) = 140 + 273
temp1#(5) = 159.5 + 273
temp1#(6) = 159.6 + 273
temp1#(7) = 164.9 + 273
temp1#(8) = 168.8 + 273
temp1#(9) = 179.7 + 273
temp1#(10) = 207.1 + 273

FOR t = 1 TO 10
FOR filter = 1 TO FILTERMAX
MLOLD# = 0
I = 0
FOR lam# = LAMMIN#(filter) TO LAMMAX#(filter) STEP DLAM#
I = I + 1
R# = a#(filter, I)
MLbb# = c1# / (lam# ^ 5 * (EXP(c2# / (lam# * temp1#(t))) - 1)) * 1
MLsamp(filter, t) = MLbb# * R# * DLAM# + MLOLD#
MLOLD# = MLsamp(filter, t)
NEXT lam#
'PRINT MLhigh#(filter)
NEXT filter
NEXT t

'FOR filter = 1 TO 4: PRINT MLh(filter, 1); MLh(filter, 2); MLh(filter, 3): NEXT filter

END SUB

```

## SUB gainoff (a#(), BBmes(), MLbb(), MLmes(), flow, tmed, thigh, temp#)

```

DIM MLtemp#(4)

DIM dfilter(4)

FOR filter = 1 TO FILTERMAX
'Gain and offset the data using low and high blackbody values
ofcet = (MLbb(filter, flow) * BBmes(filter, thigh) - MLbb(filter, thigh) * BBmes(filter, flow)) / (MLbb(filter, flow) - MLbb(filter, thigh))
gall = (BBmes(filter, thigh) - ofcet) / MLbb(filter, thigh)
IF filter = 1 THEN gall = gall * .93
'IF filter = 4 THEN gall = gall * .9
FOR t = 1 TO 10
MLmes(filter, t) = (MLmes(filter, t) - ofcet) / gall
'print MLmes(filter, t)
NEXT t
BBmes(filter, tmed) = (BBmes(filter, tmed) - ofcet) / gall'Gain and offset mid bb reading
PRINT ML; ML#(4, 10), gall; ofcet
NEXT filter

FOR t = temp# - 50 TO temp# + 50 STEP 5
FOR filter = 1 TO FILTERMAX
MLOLD# = 0
I = 0
FOR lam# = LAMMIN#(filter) TO LAMMAX#(filter) STEP DLAM#
I = I + 1
R# = a#(filter, I)
MLbb# = c1# / (lam# ^ 5 * (EXP(c2# / (lam# * t)) - 1)) * 1
MLtemp#(filter) = MLbb# * R# * DLAM# + MLOLD#

```

```

    MLOLD# = (MLtemp#(filter))
NEXT lam#
'PRINT MLmed#(filter); med(filter)
NEXT filter
FOR I = 1 TO FILTERMAX
    dfilter(I) = MLmes(I, tmed) / MLtemp#(I) - BBmes(i, tmed)
NEXT I
IF t = temp# THEN COLOR 5 ELSE COLOR 10
PRINT t; dfilter(1); dfilter(2); dfilter(1) - dfilter(2); dfilter(3); dfilter(4)
NEXT t

OPEN "a:\DATA.FIL" FOR OUTPUT AS #1
FOR filter = 1 TO FILTERMAX
    I = 0
    FOR lam# = LAMMIN#(filter) TO LAMMAX#(filter) STEP DLAM#
        I = I + 1
        PRINT #1, a#(filter, I)
    ' PRINT a#(filter, i)
    NEXT lam#
NEXT filter
CLOSE #1

OPEN "a:\DATA.SYS" FOR OUTPUT AS #2
PRINT #2, FILTERMAX
PRINT #2, DLAM#
FOR I = 1 TO FILTERMAX: PRINT #2, LAMMIN#(I): NEXT I
FOR I = 1 TO FILTERMAX: PRINT #2, LAMMAX#(I): NEXT I

FOR t = 1 TO 10
FOR I = 1 TO FILTERMAX: PRINT #2, MLmes(I, t): NEXT I
NEXT t

CLOSE #2
END SUB

SUB getbbdata (FILTERMAX, BBmes(), MLmes())

OPEN "a:\blackbo1.arr" FOR BINARY AS #1
GET #1, 1, o
a! = ASC(o)
GET #1, a!, o
PRINT

FOR I = 1 TO FILTERMAX

    FOR t = 1 TO 10
        GET #1, , BBmes(I, t)
    ' PRINT BBmes(I, t); : INPUT a$
    NEXT t
    ' INPUT a$
NEXT I

CLOSE #1

OPEN "a:\sample2.arr" FOR BINARY AS #1
GET #1, 1, o
a! = ASC(o)
GET #1, a!, o
PRINT

FOR I = 1 TO FILTERMAX

    FOR t = 1 TO 10
        GET #1, , MLmes(I, t)
    ' PRINT MLmes(i, t), i, t; : INPUT a$
    NEXT t
    ' INPUT a$
NEXT I

```

CLOSE #1

END SUB

### SUB Normalize (a#())

OPEN "a:\filter1.arr" FOR BINARY AS #2  
OPEN "a:\temp.arr" FOR BINARY AS #1

GET #2, 1, o  
b! = ASC(o)  
GET #2, b!, o

FOR I = 1 TO 499  
GET #1, , m#  
a#(5, I) = m# \* 1.5  
NEXT I

max = 0  
FOR filter = 1 TO 4  
GET #2, , OF1  
FOR I = 1 TO 499  
GET #2, , M1  
' a#(filter, I) = M1  
IF a#(5, I) > .01 AND I < 480 AND I > 10 THEN a#(filter, I) = M1 / a#(5, I)  
IF max < a#(filter, I) THEN max = a#(filter, I)  
NEXT I  
NEXT filter

CLOSE #1  
CLOSE #2

END SUB

### SUB PLOTDATA (a#())

LINE (5, 1)-(5, 100), 2  
LINE (1, 100)-(400, 100), 2  
FOR L = 10 TO 100 STEP 10: LINE (1, L)-(10, L), 2: NEXT L

FOR filter = 1 TO FILTERMAX  
I = 0  
PSET (5, 100)  
FOR lam# = LAMMIN#(filter) TO LAMMAX#(filter) STEP DLAM# 'Calculate and store emissivities Plot filter values  
I = I + 1  
X = (lam# - 2.7) \* 200  
Y = (1 - I \* a#(filter, I)) \* 100  
LINE -(X, Y), filter  
' LOCATE 20, 1: PRINT lam#; : INPUT a\$  
NEXT lam#  
' LOCATE 20, 1: INPUT a\$  
NEXT filter

END SUB

## A2. Process Data Program:

### Main Subroutine

```
DECLARE SUB FITDATUM (TEMP#, A#())
DECLARE SUB GETDATA (samp!)
DECLARE FUNCTION MATBSD% (A) AS DOUBLE, B() AS DOUBLE, X() AS DOUBLE)
DECLARE FUNCTION MATINVD% (A) AS DOUBLE)
DECLARE FUNCTION MATLUD% (A) AS DOUBLE)
DECLARE SUB SVBKS (U!(), W!(), V!(), M!, N!, MP!, np!, B!(), X!())
DECLARE SUB SVDCMP (A!(), M!, N!, MP!, np!, W!(), V!())
DECLARE SUB MRQCOF (X!(), Y!(), SIG!(), NDATA!, A!(), MA!, LISTA!(), MFIT!, ALPHA!(), BETA!(), NALP!, CHISQ!, DUM!)
DECLARE SUB GAUSSJ (A!(), N!, NP!, B!(), M!, MP!)
DECLARE SUB COVSRT (COVAR!(), NCVN!, MA!, LISTA!(), MFIT!)
COMMON SHARED BETA()
COMMON SHARED c1#, c2#, C3#, DLAM#, filtermax, LAMMAX#(), lammin#()
COMMON SHARED ML#(), R#(), filename$

DIM SHARED LO AS INTEGER, UP AS INTEGER
DIM SHARED CONTINUE AS INTEGER, COUNT AS INTEGER
DIM SHARED RPVT(LO TO UP) AS INTEGER, CPVT(LO TO UP) AS INTEGER

DIM LAMMAX#(10), lammin#(10), ML#(10), MQ#(10), ATARGET#(10)
DIM R$(4, 500)

'Declaration of constants
SCREEN 9
CLS
c1# = 3.7415 * 10 ^ 4
c2# = 1.43879 * 10 ^ 4
C3# = 1.88365 * 10 ^ 23

'CALL ACAL(ATARGET#())
'CALL FILTERS
'CALL FINDDATA(500, ATARGET#(), ML#(), MQ#())

filename$ = "a:DATA"

samp = 7
CALL GETDATA(samp)
DIM A#(filtermax - 1)

FOR TEMP# = 350 TO 450 STEP 5 'search temperature to find solution
    CALL FITDATUM(TEMP#, A#())
NEXT TEMP#
```

### SUB ACAL (ATARGET#())

'Do curvefit of data points as selected

```
DLAM# = .001
filtermax = 4
lammin#(1) = 3.4
lammin#(2) = 3.5
lammin#(3) = 3.6
lammin#(4) = 3.7
lammin#(5) = 3.8
lammin#(6) = 3.9
lammin#(7) = 4!
lammin#(8) = 4.1
lammin#(9) = 4.2
```

```

lammin#(10) = 4.3
LAMMAX#(1) = 3.5
LAMMAX#(2) = 3.6
LAMMAX#(3) = 3.7
LAMMAX#(4) = 3.8
LAMMAX#(5) = 3.9
LAMMAX#(6) = 4!
LAMMAX#(7) = 4.1
LAMMAX#(8) = 4.2
LAMMAX#(9) = 4.3
LAMMAX#(10) = 4.4

```

```

ATARGET#(1) = 0
ATARGET#(2) = 0
ATARGET#(3) = 0
ATARGET#(4) = -.1
ATARGET#(5) = 0
ATARGET#(6) = 2
ATARGET#(7) = 0
ATARGET#(8) = 0
ATARGET#(9) = 0
ATARGET#(10) = 0

```

```
END SUB
```

## SUB FILTERS

'Generate the filter values. The filter shapes used her are gaussian.

```
OPEN "DATA.FIL" FOR OUTPUT AS #1
```

```
FOR filter = 1 TO filtermax
```

```
I = 0
```

```
FOR lam# = lammin#(filter) TO LAMMAX#(filter) STEP DLAM#
```

```
I = I + 1
```

```
AVG = (lammin#(filter) + LAMMAX#(filter)) / 2
```

```
WID = (lammin#(filter) - LAMMAX#(filter)) / 2
```

```
R# = EXP(-3.141 * ((lam# - AVG) / WID) ^ 2) 'Gaussian filter shape
```

```
PRINT #1, R#
```

```
PRINT R#
```

```
NEXT lam#
```

```
NEXT filter
```

```
CLOSE #1
```

```
END SUB
```

## SUB FINDDATA (TEMP#, ATARGET#(), ML#(), MQ#())

'Calculate the radiant extdnce in terms of pawer (ML#) and photons  
'per second (MQ#)

```
OPEN "DATA.SYS" FOR OUTPUT AS #2
```

```
OPEN "DATA.FIL" FOR INPUT AS #1
```

```
FOR filter = 1 TO filtermax
```

```
MLOLD# = 0
```

```
MQOLD# = 0
```

```

FOR lam# = lammin#(filter) TO LAMMAX#(filter) STEP DLAM#
  INPUT #1, R#
  AOLD# = 0
  FOR I = 1 TO filtermax - 1
    emiss# = ATARGET#(I) * lam# ^ (filtermax - 1 - I) + AOLD#
    AOLD# = emiss#
  NEXT I
  MLbb# = c1# / (lam# ^ 5 * (EXP(c2# / (lam# * TEMP#)) - 1)) * emiss#
  MQBB# = C3# / (lam# ^ 4 * (EXP(c2# / (lam# * TEMP#)) - 1)) * emiss#
  ML#(filter) = MLbb# * R# * DLAM# + MLOLD#
  MQ#(filter) = MQBB# * R# * DLAM# + MQOLD#
  MLOLD# = ML#(filter)
  MQOLD# = MQ#(filter)
NEXT lam#
NEXT filter

PRINT #2, filtermax
PRINT #2, DLAM#
FOR I = 1 TO filtermax: PRINT #2, lammin#(I): NEXT I
FOR I = 1 TO filtermax: PRINT #2, LAMMAX#(I): NEXT I
FOR I = 1 TO filtermax: PRINT #2, ML#(I): NEXT I

CLOSE #1
CLOSE #2
END SUB

```

### SUB FITDATUM (TEMP#, A#())

'Find coef. at a given temperature and compute temperature

```

DIM MATRIXsvd#(1 TO filtermax, 1 TO filtermax - 1)
DIM MATRIX#(1 TO filtermax - 1, 1 TO filtermax - 1)
DIM MLOLD#(1 TO filtermax)
DIM U(4, 3), W(4, 3), V(4, 3), X(4), ML(4), ER(4)

'OPEN filename$ + ".FIL" FOR INPUT AS #1

' FOR filter = 1 TO filtermax - 1 'Generate the matrix of simotaneous equations
'   FOR I = 1 TO filtermax - 1: MLOLD#(I) = 0: NEXT I
'   FOR lam# = lammin#(filter) TO LAMMAX#(filter) STEP DLAM#
'     INPUT #1, R#
'     FOR COL = 1 TO filtermax - 1
'       MLbb# = c1# / (lam# ^ (5 - (filtermax - 1 - COL)) * (EXP(c2# / (lam# * TEMP#)) - 1))
'       MATRIX#(COL, filter) = MLbb# * R# * DLAM# + MLOLD#(COL)
'       MLOLD#(COL) = MATRIX#(COL, filter)
'     NEXT COL
'   NEXT lam#
' NEXT filter

' ERRCODE% = MATINVD%(MATRIX#())

'FOR ROW = 1 TO filtermax - 1          ' determine emissivity coef.
'  AOLD# = 0
'  FOR COL = 1 TO filtermax - 1
'    a#(ROW) = MATRIX#(COL, ROW) * ML#(COL) + AOLD#
'    AOLD# = a#(ROW)
'  NEXT COL
NEXT ROW

'FOR I = 1 TO FILTERMAX - 1: a = a#(I): PRINT a; : NEXT I

' MLOLD# = 0
' MLOLD1# = 0
' FOR lam# = lammin#(filtermax) TO LAMMAX#(filtermax) STEP DLAM#
'   INPUT #1, R#

```

```

' AOLD# = 0

' FOR I = 1 TO filtermax - 1      'determine emissivity of forth filter
'   emiss# = a#(I) * lam# ^ (filtermax - 1 - I) + AOLD#
'   AOLD# = emiss#
' NEXT I

' MLbb# = c1# / (lam# ^ 5 * (EXP(c2# / (lam# * TEMP#)) - 1)) * emiss#
' ML# = MLbb# * R# * DLAM# + MLOLD#
' MLOLD# = ML#
' NEXT lam#

' er = ML# - ML#(filtermax)

' AOLD# = 0
' FOR I = 1 TO filtermax - 1
'   em# = a#(I) * lammin#(4) + 450 * DLAM# ^ (filtermax - 1 - I) + AOLD#
'   AOLD# = em#
' NEXT I
' emis = ML#(filtermax) / ML1#
' PRINT emis; emiss#; TEMP# - 273; emis - em#, emis - emiss#

'CLOSE #1

FOR filter = 1 TO filtermax      'Generate the matrix for svd
  L = 0
  FOR I = 1 TO filtermax - 1: MLOLD#(I) = 0: NEXT I
  FOR lam# = lammin#(filter) TO LAMMAX#(filter) STEP DLAM#
    L = L + 1
    R# = R#(filter, L)
    FOR COL = 1 TO filtermax - 1
      MLbb# = c1# / (lam# ^ (5 - (filtermax - 1 - COL))) * (EXP(c2# / (lam# * TEMP#)) - 1))
      MATRIXsvd#(filter, COL) = MLbb# * R# * DLAM# + MLOLD#(COL)
      MLOLD#(COL) = MATRIXsvd#(filter, COL)
    NEXT COL
  NEXT lam#
NEXT filter

FOR filter = 1 TO filtermax      'Copy matrixsvd# into U#
  FOR COL = 1 TO filtermax - 1
    U(filter, COL) = MATRIXsvd#(filter, COL)
  NEXT COL
NEXT filter

CALL SVDCMP(U(), 4, 3, np, np, W(), V())  'Decompose matrix A

FOR filter = 1 TO filtermax
  ML(filter) = ML#(filter)
NEXT filter

WMAX = 0!
FOR filter = 1 TO filtermax      'Find maximum singular value
  IF W(filter) > WMAX THEN WMAX = W(filter)
NEXT filter
WMIN = WMAX * (.000001)          'Define "small"
FOR filter = 1 TO filtermax      'Zero the "small" singular values
  IF W(filter) < WMIN THEN W(filter) = 0!
NEXT filter

'Backsubstitute for each right-hand side vector
CALL SVBKS(U(), W(), V(), 4, 3, np, np, ML(), X())

FOR filter = 1 TO filtermax
  MLOLD# = 0
  MLOLD1# = 0
  L = 0
  FOR lam# = lammin#(filter) TO LAMMAX#(filter) STEP DLAM#
    L = L + 1

```

```

R# = R#(filter, L)
AOLD# = 0

FOR I = 1 TO filtermax - 1      'determine emissivity of forth filter
    emiss# = X(I) * lam# ^ (filtermax - 1 - I) + AOLD#
    AOLD# = emiss#
NEXT I

MLbb# = c1# / (lam# ^ 5 * (EXP(c2# / (lam# * TEMP#)) - 1)) * emiss#
ML# = MLbb# * R# * DLAM# + MLOLD#
MLOLD# = ML#
NEXT lam#

ER(filter) = ML# - ML#(filter)
NEXT filter

PRINT
PRINT TEMP# - 273; ER(1) + ER(2) + ER(3) + ER(4);
FOR K = 1 TO filtermax - 1: PRINT USING "#####.#####"; X(K); : NEXT K

END SUB

```

### SUB GETDATA (samp)

```

DIM MLt(4, 10)

OPEN filename$ + ".SYS" FOR INPUT AS #2

INPUT #2, filtermax
INPUT #2, DLAM#
FOR I = 1 TO filtermax: INPUT #2, lammin#(I): NEXT I
FOR I = 1 TO filtermax: INPUT #2, LAMMAX#(I): NEXT I

t = 1
FOR t = 1 TO 10
    FOR I = 1 TO filtermax
        INPUT #2, MLt(I, t)
        'PRINT MLt(I, t);
    NEXT I
    PRINT
NEXT t

FOR I = 1 TO filtermax
    ML#(I) = MLt(I, samp)
    ' PRINT MLt(I, samp)
NEXT I

CLOSE #2

OPEN filename$ + ".FIL" FOR INPUT AS #1
FOR filter = 1 TO filtermax      'Generate the matrix of filter values

    L = 0
    FOR lam# = lammin#(filter) TO LAMMAX#(filter) STEP DLAM#
        L = L + 1
        INPUT #1, R#
        R#(filter, L) = R#
        'PRINT R#(FILTER, L); FILTER; L'; : INPUT A$
    NEXT lam#

NEXT filter
CLOSE #1

END SUB

```

## FUNCTION MATBSD% (A() AS DOUBLE, B() AS DOUBLE, X() AS DOUBLE)

```
ON LOCAL ERROR GOTO DBSERR: MATBSD% = 0
'do row operations on b using the multipliers in L to find Lb
FOR PVT% = LO TO (UP - 1)
  C% = CPVT(PVT%)
  FOR ROW% = (PVT% + 1) TO UP
    R% = RPVT(ROW%)
    B(R%) = B(R%) + A(R%, C%) * B(RPVT(PVT%))
  NEXT ROW%
NEXT PVT%
FOR ROW% = UP TO LO STEP -1 'backsolve UX=Lb to find x
  C% = CPVT(ROW%)
  R% = RPVT(ROW%)
  X(C%) = B(R%)
  FOR COL% = (ROW% + 1) TO UP
    X(C%) = X(C%) - A(R%, CPVT(COL%)) * X(CPVT(COL%))
  NEXT COL%
  X(C%) = X(C%) / A(R%, C%)
NEXT ROW%
DBSEXIT:
EXIT FUNCTION
DBSERR:
  MATBSD% = ERR
  RESUME DBSEXIT
END FUNCTION
```

## SUB MRQMIN (X(), Y(), SIG(), NDATA, A(), MA, LISTA(), MFIT, COVAR(), ALPHA(), NCA, CHISQ, DUM, ALAMDA)

```
STATIC
DIM ATRY(MA), DA(MA, 1)
IF ALAMDA < 0! THEN
  KK = MFIT + 1
  FOR J = 1 TO MA
    IHIT = 0
    FOR K = 1 TO MFIT
      IF LISTA(K) = J THEN IHIT = IHIT + 1
    NEXT K
    IF IHIT = 0 THEN
      LISTA(KK) = J
      KK = KK + 1
    ELSEIF IHIT > 1 THEN
      PRINT "Improper permutation in LISTA"
      EXIT SUB
    END IF
  NEXT J
  IF KK > MA + 1 THEN PRINT "Improper permutation in LISTA": EXIT SUB
  ALAMDA = .001
  CALL MRQCOF(X(), Y(), SIG(), NDATA, A(), MA, LISTA(), MFIT, ALPHA(), BETA(), NCA, CHISQ, DUM)
  OCHISQ = CHISQ
  FOR J = 1 TO MA
    ATRY(J) = A(J)
  NEXT J
END IF
FOR J = 1 TO MFIT
  FOR K = 1 TO MFIT
    COVAR(J, K) = ALPHA(J, K)
  NEXT K
  COVAR(J, J) = ALPHA(J, J) * (1! + ALAMDA)
  DA(J, 1) = BETA(J, 1)
```

```

NEXT J
CALL GAUSSJ(COVAR(), MFIT, NCA, DA(), 1, 1)
IF ALAMDA = 0! THEN
  CALL COVSRT(COVAR(), NCA, MA, LISTA(), MFIT)
  ERASE DA, ATRY
  EXIT SUB
END IF
FOR J = 1 TO MFIT
  ATRY(LISTA(J)) = A(LISTA(J)) + DA(J, 1)
NEXT J
CALL MRQCOF(X(), Y(), SIG(), NDATA, ATRY(), MA, LISTA(), MFIT, COVAR(), DA(), NCA, CHISQ, DUM)
IF CHISQ < OCHISQ THEN
  ALAMDA = .1 * ALAMDA
  OCHISQ = CHISQ
  FOR J = 1 TO MFIT
    FOR K = 1 TO MFIT
      ALPHA(J, K) = COVAR(J, K)
    NEXT K
    BETA(J, 1) = DA(J, 1)
    A(LISTA(J)) = ATRY(LISTA(J))
  NEXT J
ELSE
  ALAMDA = 10! * ALAMDA
  CHISQ = OCHISQ
END IF
ERASE DA, ATRY
END SUB

```

## FUNCTION MATINVD% (A() AS DOUBLE)

```

ON LOCAL ERROR GOTO DINVERR: ERRCODE% = 0
LO = LBOUND(A, 1)
UP = UBOUND(A, 1)
DIM AIN(LO TO UP, LO TO UP) AS DOUBLE
DIM E(LO TO UP) AS DOUBLE, X(LO TO UP) AS DOUBLE
REDIM RPVT(LO TO UP) AS INTEGER, CPVT(LO TO UP) AS INTEGER
ERRCODE% = MATLUD%(A()) 'Get LU matrix
IF NOT CONTINUE THEN ERROR ERRCODE%
FOR COL% = LO TO UP 'Find A^-1 one column at a time
  E(COL%) = 1#
  BSERRCODE% = MATBSD%(A(), E(), X())
  IF BSERRCODE% THEN ERROR BSERRCODE%
  FOR ROW% = LO TO UP
    AIN(ROW%, COL%) = X(ROW%)
    E(ROW%) = 0#
  NEXT ROW%
NEXT COL%
FOR COL% = LO TO UP 'Put A^-1 in A
  FOR ROW% = LO TO UP
    A(ROW%, COL%) = AIN(ROW%, COL%)
  NEXT ROW%
NEXT COL%
IF ERRCODE% THEN ERROR ERRCODE%
DINVEXIT:
ERASE E, X, AIN, RPVT, CPVT
MATINVD% = ERRCODE%
EXIT FUNCTION
DINVERR:
  ERRCODE% = (ERR + 5) MOD 200 - 5
  RESUME DINVEXIT
END FUNCTION

```

## FUNCTION MATLUD% (A) AS DOUBLE

```

ON LOCAL ERROR GOTO DLUERR: ERRCODE% = 0
'Checks if A is square, returns error code if not
IF NOT (LO = LBOUND(A, 2) AND UP = UBOUND(A, 2)) THEN ERROR 198
DIM ROWNORM(LO TO UP) AS DOUBLE
COUNT = 0           'initialize count, continue
CONTINUE = -1
FOR ROW% = LO TO UP   'initialize rpvt and cpvt
    RPVT(ROW%) = ROW%
    CPVT(ROW%) = ROW%
    ROWNORM(ROW%) = 0#   'find the row norms of A()
    FOR COL% = LO TO UP
        ROWNORM(ROW%) = ROWNORM(ROW%) + ABS(A(ROW%, COL%))
    NEXT COL%
    IF ROWNORM(ROW%) = 0# THEN   'if any rownorm is zero, the matrix
        CONTINUE = 0           'is singular, set error, exit and
        ERROR 199               'do not continue
    END IF
NEXT ROW%
FOR PVT% = LO TO (UP - 1)
'Find best available pivot
    MAX# = 0#           'checks all values in rows and columns not
    FOR ROW% = PVT% TO UP   'already used for pivoting and saves the
        R% = RPVT(ROW%)     'largest absolute number and its position
        FOR COL% = PVT% TO UP
            C% = CPVT(COL%)
            TEMP# = ABS(A(R%, C%)) / ROWNORM(R%)
            IF TEMP# > MAX# THEN
                MAX# = TEMP#
                BESTROW% = ROW%   'save the position of new max#
                BESTCOL% = COL%
            END IF
        NEXT COL%
    NEXT ROW%
    IF MAX# = 0# THEN       'if no nonzero number is found, A is
        CONTINUE = 0       'singular, send back error, do not continue
        ERROR 199
    ELSEIF PVT% > 1 THEN    'check if drop in pivots is too much
        IF MAX# < (deps# * oldmax#) THEN ERRCODE% = 199
    END IF
    oldmax# = MAX#
    IF RPVT(PVT%) <> RPVT(BESTROW%) THEN
        COUNT = COUNT + 1     'if a row or column pivot is
        SWAP RPVT(PVT%), RPVT(BESTROW%) 'necessary, count it and permute
    END IF
    IF CPVT(PVT%) <> CPVT(BESTCOL%) THEN 'columns are not actually switched,
        COUNT = COUNT + 1     'only the order in which they are
        SWAP CPVT(PVT%), CPVT(BESTCOL%) 'used.
    END IF
'Eliminate all values below the pivot
    RP% = RPVT(PVT%)
    CP% = CPVT(PVT%)
    FOR ROW% = (PVT% + 1) TO UP
        R% = RPVT(ROW%)
        A(R%, CP%) = -A(R%, CP%) / A(RP%, CP%) 'save multipliers
        FOR COL% = (PVT% + 1) TO UP
            C% = CPVT(COL%)   'complete row operations
            A(R%, C%) = A(R%, C%) + A(RP%, CP%) * A(RP%, C%)
        NEXT COL%
    NEXT ROW%
NEXT PVT%
IF A(RPVT(UP), CPVT(UP)) = 0# THEN
    CONTINUE = 0           'if last pivot is zero or pivot drop is
    ERROR 199               'too large, A is singular, send back error
ELSEIF (ABS(A(RPVT(UP), CPVT(UP))) / ROWNORM(RPVT(UP))) < (deps# * oldmax#) THEN
    ERRCODE% = 199         'if pivot is not identically zero then

```

```

END IF          'continue remains TRUE
IF ERRCODE% THEN ERROR ERRCODE%
DLUEXIT:
MATLUD% = ERRCODE%
EXIT FUNCTION
DLUERR:
  IF ERRCODE% < 199 THEN CONTINUE = 0
  ERRCODE% = ERR
  RESUME DLUEXIT
END FUNCTION

```

## SUB PLOTDATA (ATARGET#())

```

I = 0
LINE (5, 1)-(5, 100), 2
LINE (1, 100)-(400, 100), 2
FOR L = 10 TO 100 STEP 10: LINE (1, L)-(10, L), 2: NEXT L
FOR lam# = 3 TO 5 STEP DLAM#          'Draw/plot emissivity curve
  AOLD# = 0
  FOR I = 1 TO filtermax - 1
    emiss# = ATARGET#(I) * lam# ^ (filtermax - 1 - I) + AOLD#
    AOLD# = emiss#
  NEXT I
  X = (lam# - 3) * 300
  Y = (1 - emiss#) * 100
  PSET (X, Y), 3
NEXT lam#

OPEN filename$ + ".FIL" FOR INPUT AS #1
'OPEN "DATA" FOR INPUT AS #1
FOR filter = 1 TO filtermax
  FOR lam# = lammin#(filter) TO LAMMAX#(filter) STEP DLAM#  'Calculate and store emissivities Plot filter values
    INPUT #1, R#
    PRINT R#
    AOLD# = 0
    FOR I = 1 TO filtermax - 1
      emiss# = ATARGET#(I) * lam# ^ (filtermax - 1 - I) + AOLD#
      AOLD# = emiss#
    NEXT I
    emiss# = 1
    X = (lam# - 3) * 300
    Y = (1 - emiss# * R#) * 100
    PSET (X, Y)
  NEXT lam#
NEXT filter

CLOSE #1

END SUB

```

## SUB SVBKSB (U0, W0, V0, M, N, MP, np, B0, X0)

```

DIM TMP(N)
FOR J = 1 TO N
  S = 0!
  IF W(J) <> 0! THEN
    FOR I = 1 TO M
      S = S + U(I, J) * B(I)
    NEXT I
  END IF
NEXT J

```

```

    S = S / W(J)
  END IF
  TMP(J) = S
NEXT J
FOR J = 1 TO N
  S = 0!
  FOR JJ = 1 TO N
    S = S + V(J, JJ) * TMP(JJ)
  NEXT JJ
  X(J) = S
NEXT J
ERASE TMP
END SUB

```

### SUB SVDCMP (A(), M, N, MP, np, W(), V())

```

DIM RV1(N)
IF M < N THEN PRINT "You must augment A with extra zero rows.": EXIT SUB
G = 0!
SCALE = 0!
ANORM = 0!
FOR I = 1 TO N
  L = I + 1
  RV1(I) = SCALE * G
  G = 0!
  S = 0!
  SCALE = 0!
  IF I <= M THEN
    FOR K = I TO M
      SCALE = SCALE + ABS(A(K, I))
    NEXT K
    IF SCALE <> 0! THEN
      FOR K = I TO M
        A(K, I) = A(K, I) / SCALE
        S = S + A(K, I) * A(K, I)
      NEXT K
      F = A(I, I)
      G = -ABS(SQR(S)) * SGN(F)
      H = F * G - S
      A(I, I) = F - G
      IF I <> N THEN
        FOR J = L TO N
          S = 0!
          FOR K = I TO M
            S = S + A(K, I) * A(K, J)
          NEXT K
          F = S / H
          FOR K = I TO M
            A(K, J) = A(K, J) + F * A(K, I)
          NEXT K
        NEXT J
      END IF
      FOR K = I TO M
        A(K, I) = SCALE * A(K, I)
      NEXT K
    END IF
  END IF
  W(I) = SCALE * G
  G = 0!
  S = 0!
  SCALE = 0!
  IF I <= M AND I <> N THEN
    FOR K = L TO N
      SCALE = SCALE + ABS(A(I, K))
    NEXT K
  END IF

```

```

IF SCALE <> 0! THEN
  FOR K = L TO N
    A(I, K) = A(I, K) / SCALE
    S = S + A(I, K) * A(I, K)
  NEXT K
  F = A(I, L)
  G = -ABS(SQR(S)) * SGN(F)
  H = F * G - S
  A(I, L) = F - G
  FOR K = L TO N
    RV1(K) = A(I, K) / H
  NEXT K
  IF I <> M THEN
    FOR J = L TO M
      S = 0!
      FOR K = L TO N
        S = S + A(J, K) * A(I, K)
      NEXT K
      FOR K = L TO N
        A(J, K) = A(J, K) + S * RV1(K)
      NEXT K
    NEXT J
  END IF
  FOR K = L TO N
    A(I, K) = SCALE * A(I, K)
  NEXT K
END IF
END IF
IF ABS(W(I)) + ABS(RV1(I)) > ANORM THEN ANORM = ABS(W(I)) + ABS(RV1(I))
NEXT I
FOR I = N TO 1 STEP -1
  IF I < N THEN
    IF G <> 0! THEN
      FOR J = L TO N
        V(J, I) = (A(I, J) / A(I, L)) / G
      NEXT J
      FOR J = L TO N
        S = 0!
        FOR K = L TO N
          S = S + A(I, K) * V(K, J)
        NEXT K
        FOR K = L TO N
          V(K, J) = V(K, J) + S * V(K, I)
        NEXT K
      NEXT J
    END IF
    FOR J = L TO N
      V(I, J) = 0!
      V(J, I) = 0!
    NEXT J
  END IF
  V(I, I) = 1!
  G = RV1(I)
  L = I
NEXT I
FOR I = N TO 1 STEP -1
  L = I + 1
  G = W(I)
  IF I < N THEN
    FOR J = L TO N
      A(I, J) = 0!
    NEXT J
  END IF
  IF G <> 0! THEN
    G = 1! / G
  IF I <> N THEN
    FOR J = L TO N
      S = 0!

```

```

        FOR K = L TO M
            S = S + A(K, I) * A(K, J)
        NEXT K
        F = (S / A(I, I)) * G
        FOR K = 1 TO M
            A(K, J) = A(K, J) + F * A(K, I)
        NEXT K
    NEXT J
END IF
FOR J = 1 TO M
    A(J, I) = A(J, I) * G
NEXT J
ELSE
    FOR J = 1 TO M
        A(J, I) = 0!
    NEXT J
END IF
A(I, I) = A(I, I) + 1!
NEXT I
FOR K = N TO 1 STEP -1
    FOR ITS = 1 TO 30
        FOR L = K TO 1 STEP -1
            NM = L - 1
            IF ABS(RV1(L)) + ANORM = ANORM THEN EXIT FOR
            IF ABS(W(NM)) + ANORM = ANORM THEN EXIT FOR
        NEXT L
        IF ABS(RV1(L)) + ANORM <> ANORM THEN
            C = 0!
            S = 1!
            FOR I = L TO K
                F = S * RV1(I)
                RV1(I) = C * RV1(I)
                IF ABS(F) + ANORM <> ANORM THEN
                    G = W(I)
                    H = SQR(F * F + G * G)
                    W(I) = H
                    H = 1! / H
                    C = G * H
                    S = -F * H
                    FOR J = 1 TO M
                        Y = A(J, NM)
                        Z = A(J, I)
                        A(J, NM) = Y * C + Z * S
                        A(J, I) = -Y * S + Z * C
                    NEXT J
                END IF
            NEXT I
        END IF
    NEXT I
END IF
Z = W(K)
IF L = K THEN
    IF Z < 0! THEN
        W(K) = -Z
        FOR J = 1 TO N
            V(J, K) = -V(J, K)
        NEXT J
    END IF
    EXIT FOR
END IF
IF ITS = 30 THEN PRINT "No convergence in 30 iterations": ERASE RV1: END
X = W(L)
NM = K - 1
Y = W(NM)
G = RV1(NM)
H = RV1(K)
F = ((Y - Z) * (Y + Z) + (G - H) * (G + H)) / (2! * H * Y)
G = SQR(F * F + 1!)
F = ((X - Z) * (X + Z) + H * ((Y / (F + ABS(G) * SGN(F))) - H)) / X
C = 1!

```

```

S = 1!
FOR J = L TO NM
  I = J + 1
  G = RV1(I)
  Y = W(I)
  H = S * G
  G = C * G
  Z = SQR(F * F + H * H)
  RV1(J) = Z
  C = F / Z
  S = H / Z
  F = X * C + G * S
  G = -X * S + G * C
  H = Y * S
  Y = Y * C
  FOR JJ = 1 TO N
    X = V(JJ, J)
    Z = V(JJ, I)
    V(JJ, J) = X * C + Z * S
    V(JJ, I) = -X * S + Z * C
  NEXT JJ
  Z = SQR(F * F + H * H)
  W(J) = Z
  IF Z <> 0! THEN
    Z = 1! / Z
    C = F * Z
    S = H * Z
  END IF
  F = C * G + S * Y
  X = -S * G + C * Y
  FOR JJ = 1 TO M
    Y = A(JJ, J)
    Z = A(JJ, I)
    A(JJ, J) = Y * C + Z * S
    A(JJ, I) = -Y * S + Z * C
  NEXT JJ
NEXT J
RV1(L) = 0!
RV1(K) = F
W(K) = X
NEXT ITS
NEXT K
ERASE RV1
END SUB

```

### SUB test (TEMP#)

```

OPEN filename$ + ".FIL" FOR INPUT AS #1

FOR filter = 1 TO 4

  MLOLD1# = 0
  FOR lam# = lammin#(filtermax) TO LAMMAX#(filtermax) STEP DLAM#
    INPUT #1, R#
    AOLD# = 0
    MLbb1# = c1# / (lam# ^ 5 * (EXP(c2# / (lam# * TEMP#)) - 1)) * I
    ML1# = MLbb1# * R# * DLAM# + MLOLD1#
    MLOLD1# = ML1#

  NEXT lam#

  emis = ML#(filter) / ML1#
  PRINT emis;

```

NEXT filter  
 PRINT TEMP# - 273

CLOSE #1

END SUB

# **SUB MRQMIN (X0, Y0, SIG0, NDATA, A0, MA, LISTA0, MFIT, COVAR0, ALPHA0, NCA, CHISQ, DUM, ALAMDA)**

```

  STATIC
  DIM ATRY(MA), DA(MA, 1)
  IF ALAMDA < 0! THEN
    KK = MFIT + 1
    FOR J = 1 TO MA
      IHIT = 0
      FOR K = 1 TO MFIT
        IF LISTA(K) = J THEN IHIT = IHIT + 1
      NEXT K
      IF IHIT = 0 THEN
        LISTA(KK) = J
        KK = KK + 1
      ELSEIF IHIT > 1 THEN
        PRINT "Improper permutation in LISTA"
        EXIT SUB
      END IF
    NEXT J
    IF KK <> MA + 1 THEN PRINT "Improper permutation in LISTA": EXIT SUB
    ALAMDA = .001
    CALL MRQCOF(X0, Y0, SIG0, NDATA, A0, MA, LISTA0, MFIT, ALPHA0, BETA0, NCA, CHISQ, DUM)
    OCHISQ = CHISQ
    FOR J = 1 TO MA
      ATRY(J) = A(J)
    NEXT J
    END IF
    FOR J = 1 TO MFIT
      FOR K = 1 TO MFIT
        COVAR(J, K) = ALPHA(J, K)
      NEXT K
      COVAR(J, J) = ALPHA(J, J) * (1! + ALAMDA)
      DA(J, 1) = BETA(J, 1)
    NEXT J
    CALL GAUSSJ(COVAR0, MFIT, NCA, DA0, 1, 1)
    IF ALAMDA = 0! THEN
      CALL COVSRT(COVAR0, NCA, MA, LISTA0, MFIT)
      ERASE DA, ATRY
      EXIT SUB
    END IF
    FOR J = 1 TO MFIT
      ATRY(LISTA(J)) = A(LISTA(J)) + DA(J, 1)
    NEXT J
    CALL MRQCOF(X0, Y0, SIG0, NDATA, ATRY0, MA, LISTA0, MFIT, COVAR0, DA0, NCA, CHISQ, DUM)
    IF CHISQ < OCHISQ THEN
      ALAMDA = .1 * ALAMDA
      OCHISQ = CHISQ
      FOR J = 1 TO MFIT
        FOR K = 1 TO MFIT
          ALPHA(J, K) = COVAR(J, K)
        NEXT K
        BETA(J, 1) = DA(J, 1)
        A(LISTA(J)) = ATRY(LISTA(J))
      NEXT J
    ELSE
      ALAMDA = 10! * ALAMDA
      CHISQ = OCHISQ
    END IF
    ERASE DA, ATRY
  
```

END SUB

### A3. Reconstruct Program:

```
DECLARE SUB Normalize (a#())
DECLARE SUB PLOTDATA (ATARGET#())

DIM SHARED o AS STRING * 1
DIM SHARED ML#(10)
COMMON SHARED DLAM#, FILTERMAX, LAMMAX#(), LAMMIN#()
SCREEN 9
CLS

DIM a#(5, 500), lo(4), med(4), hi(4), MLhigh#(4), MLlow#(4), MLmid#(4)
DIM LAMMIN#(5), LAMMAX#(5)
EMISS# = 1
FILTERMAX = 4
DLAM# = .005
LAMMIN#(1) = 2.7
LAMMAX#(1) = 5.2 - DLAM#
LAMMIN#(2) = 2.7
LAMMAX#(2) = 5.2 - DLAM#
LAMMIN#(3) = 2.7
LAMMAX#(3) = 5.2 - DLAM#
LAMMIN#(4) = 2.7
LAMMAX#(4) = 5.2 - DLAM#
LAMMIN#(5) = 2.7
LAMMAX#(5) = 5.2 - DLAM#

x$ = STR$(1)
x$ = MID$(x$, 2)
f$ = "a:\monocr" + x$ + ".arr"
PRINT f$

OPEN f$ FOR BINARY AS #1
GET #1, 1, o
a! = ASC(o)
GET #1, a!, o
GET #1, , OF
FOR I = 1 TO 499
  GET #1, , m
  a#(1, I) = m
NEXT I
CLOSE #1

LINE (5, 1)-(5, 100), 2
LINE (1, 100)-(400, 100), 2
FOR I = 10 TO 100 STEP 10: LINE (1, I)-(10, I), 2: NEXT I

I = 0
PSET (5, 100)
FOR lam# = LAMMIN#(1) TO LAMMAX#(1) STEP DLAM# 'Calculate and store emissivities Plot filter values

  I = I + 1
  IF I < 55 THEN a#(1, I) = a#(1, 55) * I / 55
  IF I > 294 AND I < 336 THEN a#(1, I) = a#(1, 294) - (a#(1, 294) - a#(1, 336)) * (I - 294) / 40
  IF I > 435 THEN a#(1, I) = a#(1, 435) - a#(1, 435) * (I - 435) / 64
  x = (lam# - 2.7) * 200
  Y = (1 - .1 * a#(1, I)) * 100
  LINE -(x, Y), 5
  LOCATE 20, 1: PRINT lam#, i; : INPUT a$
NEXT lam#
LOCATE 20, 1: INPUT a$

OPEN f$ FOR BINARY AS #1
OPEN "a:\temp.arr" FOR BINARY AS #2
```

```

GET #1, 1, o
a! = ASC(o)
GET #1, a!, o
GET #1, , OF
FOR I = 1 TO 499
PUT #2, , a#(1, I)
NEXT I
CLOSE #1
CLOSE #2

SUB calcML (a#(), MLhigh#(), MLlow#())

C1# = 3.7415 * 10 ^ 4
C2# = 1.43879 * 10 ^ 4
C3# = 1.88365 * 10 ^ 23

INPUT "input low temp", temp#
FOR FILTER = 1 TO FILTERMAX
  MLOLD# = 0
  I = 0
  FOR lam# = LAMMIN#(FILTER) TO LAMMAX#(FILTER) STEP DLAM#
    I = I + 1
    R# = a#(FILTER, I)
    MLBB# = C1# / (lam# ^ 5 * (EXP(C2# / (lam# * temp#)) - 1)) * EMISS#
    MLlow#(FILTER) = MLBB# * R# * DLAM# + MLOLD#
    MLOLD# = MLlow#(FILTER)
  NEXT lam#
NEXT FILTER

INPUT "input high temp", temp#
FOR FILTER = 1 TO FILTERMAX
  MLOLD# = 0
  I = 0
  FOR lam# = LAMMIN#(FILTER) TO LAMMAX#(FILTER) STEP DLAM#
    I = I + 1
    R# = a#(FILTER, I)
    MLBB# = C1# / (lam# ^ 5 * (EXP(C2# / (lam# * temp#)) - 1)) * EMISS#
    MLhigh#(FILTER) = MLBB# * R# * DLAM# + MLOLD#
    MLOLD# = MLhigh#(FILTER)
  NEXT lam#
NEXT FILTER

END SUB

SUB gainoff (a#(), lo(), mid(), hi(), MLlow#(), MLhigh#(), MLmid#())

INPUT "input data file name (sample1) and no. in file (0-2)", filename$, no!
filename$ = "sample1.arr": no! = 2
DIM dfilter(4)
OPEN filename$ FOR BINARY AS #3
GET #1, 1, o
a! = ASC(o) + 4! * no!
GET #1, a!, o

OPEN "a:\DATA.FIL" FOR OUTPUT AS #1
FOR FILTER = 1 TO FILTERMAX 'Gain and offset the data using low and high blackbody values
  Gall = (hi(FILTER) - lo(FILTER)) / (MLhigh#(FILTER) - MLlow#(FILTER))
  ofcet = lo(FILTER) - MLlow#(FILTER) * Gall
  GET #3, , ML
  ML#(FILTER) = (ML - ofcet) / Gall
  I = 0
  FOR lam# = LAMMIN#(FILTER) TO LAMMAX#(FILTER) STEP DLAM#
    I = I + 1
    PRINT #1, a#(FILTER, I)
  NEXT lam#
NEXT FILTER
CLOSE #1
CLOSE #3

```

```

INPUT "input mid temp", t 'Calculate errors using 3rd blackbody value
FOR temp# = t - 10 TO t + 10
FOR FILTER = 1 TO FILTERMAX
  MLOLD# = 0
  I = 0
  FOR lam# = LAMMIN#(FILTER) TO LAMMAX#(FILTER) STEP DLAM#
    I = I + 1
    R# = a#(FILTER, I)
    MLBB# = C1# / (lam# ^ 5 * (EXP(C2# / (lam# * temp#)) - 1)) * EMISS#
    MLmid#(FILTER) = MLBB# * R# * DLAM# + MLOLD#
    MLOLD# = (MLmid#(FILTER) - ofcet) / Gall
  NEXT lam#
NEXT FILTER
FOR I = 1 TO FILTERMAX
  dfilter(I) = MLmid#(I) - mid(I)
NEXT I
PRINT temp#, dfilter(1), dfilter(2), dfilter(3), dfilter(4)
NEXT temp#

OPEN "DATA.SYS" FOR OUTPUT AS #2
PRINT #2, FILTERMAX
PRINT #2, DLAM#
FOR I = 1 TO FILTERMAX: PRINT #2, LAMMIN#(I): NEXT I
FOR I = 1 TO FILTERMAX: PRINT #2, LAMMAX#(I): NEXT I
FOR I = 1 TO FILTERMAX: PRINT #2, ML#(I): NEXT I
CLOSE #2
END SUB

SUB getbbdata (FILTERMAX, lo(), med(), hi())

OPEN "a:\blackbo1.arr" FOR BINARY AS #1
GET #1, 1, o
a! = ASC(o)
GET #1, a!, o
FOR I = 1 TO FILTERMAX
  GET lo(I), med(I), hi(I)
NEXT I
CLOSE #1

END SUB

SUB Normalize (a#())

END SUB

SUB PLOTDATA (a#())

END SUB

```

## Appendix B-Amber Proview Software

The programs contained in this appendix have been developed in the Amber ProView TDF language. There were used to interface the Amber 256 x 256 snapshot camera and there purpose is basic data collection.

### **B1. Calibrate Monochromator Light Source:**

```
set timeout(120)
arr discard(a10)
arr discard(a11)
arr discard(a12)
arr discard(a13)
arr create(a13,2, 500)
arr create(a10, 256, 256)
arr create(a11, 5, 500)
arr create(a12, 5, 3)
a11 = 0.0
a12 = 0.0
a13 = 0.0
i5=0

loop (500)

i5= i5 + 1
s5 = chr(13)
s0 = '2700.0 GOTO' + s5
gpib write(11,s0)
delay(15000)

r5=1.0
i1 = 0
loop (500)
  acquire(1,1,N)
  a10 = upload(c1, 0, 65536)
  a13[1,i1] = a10[1, 127]
  a13[1,i1] = a13[1,i1] + a10[1, 128]
  a13[1,i1] = a13[1,i1] + a10[1, 129]
  a13[1,i1] = a13[1,i1] + a10[2, 127]
  a13[1,i1] = a13[1,i1] + a10[2, 128]
  a13[1,i1] = a13[1,i1] + a10[2, 129]
  a13[1,i1] = a13[1,i1] + a10[3, 127]
  a13[1,i1] = a13[1,i1] + a10[3, 128]
  a13[1,i1] = a13[1,i1] + a10[3, 129]
  if (i1> 0 )
    r5=a13[1, i1]/a13[1,0]
  endif
  message(1,30,r5)
  a13[0,i1] = a10[127, 222]
  a13[0,i1] = a13[0,i1] + a10[127, 223]
  a13[0,i1] = a13[0,i1] + a10[127, 224]
  a13[0,i1] = a13[0,i1] + a10[128, 222]
  a13[0,i1] = a13[0,i1] + a10[128, 223]
  a13[0,i1] = a13[0,i1] + a10[128, 224]
  a13[0,i1] = a13[0,i1] + a10[126, 222]
  a13[0,i1] = a13[0,i1] + a10[126, 223]
  a13[0,i1] = a13[0,i1] + a10[126, 224]
  if (i1>0)
    r6=a13[0,0] * r5
    a13[0,i1] = a13[0,i1] - r6
  endif
```

```

i1 = i1 + 1
i2 = i1 * 5
i3 = i2 + 2700
s2 = str(i3)
s0 = s2 + '.0 GOTO'
s0 = s0 + s5
gpib write(i1,s0)
i4 = i1 - 1
message (1,1,i4)
message (2,1,i3)
message (4,1,a13[0,i4])
message (1, 20, i5)
endloop

s1 = str(i5)
s9 = 'b:\monocr' + s1
arr save file(a13,s9)

endloop

```

## B2. Get Data For Filter Bandpasses:

```

set timeout(120)
arr discard(a10)
arr discard(a11)
arr discard(a12)
arr discard(a13)
arr create(a13,2, 500)
arr create(a10, 256, 256)
arr create(a11, 5, 500)
arr create(a12, 5, 3)
a11 = 0.0
a12 = 0.0
a13 = 0.0

s5 = chr(13)
s0 = '2700.0 GOTO' + s5
gpib write(i1,s0)
s1='Wait for Monochrometer'
message (1,1,s1)
read(s1,,)
;echo (off)

i1 = 0
r5 = 1.0
loop (500)
    acquire(1,i1,N)
    a10 = upload(c1, 0, 65536)
    a11[4, i1] = a10[1, 127]
    a11[4, i1] = a11[4, i1] + a10[1, 128]
    a11[4, i1] = a11[4, i1] + a10[1, 129]
    a11[4, i1] = a11[4, i1] + a10[2, 127]
    a11[4, i1] = a11[4, i1] + a10[2, 128]
    a11[4, i1] = a11[4, i1] + a10[2, 129]
    a11[4, i1] = a11[4, i1] + a10[3, 127]
    a11[4, i1] = a11[4, i1] + a10[3, 128]
    a11[4, i1] = a11[4, i1] + a10[3, 129]
    if (i1 > 0)
        r5 = a11[4, i1] / a11[4, 0]
    endif
    r10 = 1 - r5
    message(1,30,r5)

    a11[0, i1] = a10[127, 30]
    a11[0, i1] = a11[0, i1] + a10[127, 31]
    a11[0, i1] = a11[0, i1] + a10[127, 32]

```

```

a11[0, I1] = a11[0, I1] + a10[128, 30]
a11[0, I1] = a11[0, I1] + a10[128, 31]
a11[0, I1] = a11[0, I1] + a10[128, 32]
a11[0, I1] = a11[0, I1] + a10[126, 30]
a11[0, I1] = a11[0, I1] + a10[126, 31]
a11[0, I1] = a11[0, I1] + a10[126, 32]
if (i1>0)
r6 = a11[0,0] * r5
a11[0, I1] = a11[0, I1] - r6
endif
a11[1, I1] = a10[127, 94]
a11[1, I1] = a11[1, I1] + a10[127, 95]
a11[1, I1] = a11[1, I1] + a10[127, 96]
a11[1, I1] = a11[1, I1] + a10[128, 94]
a11[1, I1] = a11[1, I1] + a10[128, 95]
a11[1, I1] = a11[1, I1] + a10[128, 96]
a11[1, I1] = a11[1, I1] + a10[126, 94]
a11[1, I1] = a11[1, I1] + a10[126, 95]
a11[1, I1] = a11[1, I1] + a10[126, 96]
if (i1>0 )
r7=a11[1,0] * r5
a11[1, I1] = a11[1, I1] - r7
endif
a11[2, I1] = a10[127, 158]
a11[2, I1] = a11[2, I1] + a10[127, 159]
a11[2, I1] = a11[2, I1] + a10[127, 160]
a11[2, I1] = a11[2, I1] + a10[128, 158]
a11[2, I1] = a11[2, I1] + a10[128, 159]
a11[2, I1] = a11[2, I1] + a10[128, 160]
a11[2, I1] = a11[2, I1] + a10[126, 158]
a11[2, I1] = a11[2, I1] + a10[126, 159]
a11[2, I1] = a11[2, I1] + a10[126, 160]
if (i1>0)
r8=a11[2,0] * r5
a11[2, I1] = a11[2, I1] - r8
endif
a11[3, I1] = a10[127, 222]
a11[3, I1] = a11[3, I1] + a10[127, 223]
a11[3, I1] = a11[3, I1] + a10[127, 224]
a11[3, I1] = a11[3, I1] + a10[128, 222]
a11[3, I1] = a11[3, I1] + a10[128, 223]
a11[3, I1] = a11[3, I1] + a10[128, 224]
a11[3, I1] = a11[3, I1] + a10[126, 222]
a11[3, I1] = a11[3, I1] + a10[126, 223]
a11[3, I1] = a11[3, I1] + a10[126, 224]
if (i1>0)
r9=a11[3,0] * r5
a11[3, I1] = a11[3, I1] - r9
endif
I1 = I1 + 1
i2 = I1 * 5
i3 = i2 + 2700
s2 = str(i3)
s0 = s2 + '.0 GOTO'
s0 = s0 + s5
gplib write(11,s0)
i4 = I1 - 1
message (1,1,i4)
message (2,1,i3)
message (3,1,a11[0, i4])
message (4,1,a11[1, i4])
message (5,1,a11[2, i4])
message (6,1,a11[3, i4])
message (7,1,a11[4, i4])
r1=a11[0, i4]-a11[1, i4]
r2=a11[1, i4]-a11[2, i4]
r3=a11[2, i4]-a11[3, i4]
message (9,1,r1)

```

```

message (10,1,r2)
message (11,1,r3)
endloop
s9 = 'b:\filter1'
arr save file(a11,s9)

```

### B3. Calibrate Monochromator:

```

set timeout(120)
arr discard(a10)
arr discard(a11)
arr discard(a12)
arr discard(a13)
arr create(a13,2, 500)
arr create(a10, 256, 256)
arr create(a11, 5, 500)
arr create(a12, 5, 3)
a11 = 0.0
a12 = 0.0
a13 = 0.0

s5 = chr(13)
s0 = '2700.0 GOTO' + s5
gpib write(11,s0)
s1='Wait for Monochrometer'
message (1,1,s1)
read(s1,,)
;echo (off)

r5=1.0
i1 = 0
loop (500)
    acquire(1,1,N)
    a10 = upload(c1, 0, 65536)
    a13[1,i1] = a10[1, 127]
    a13[1,i1] = a13[1,i1] + a10[1, 128]
    a13[1,i1] = a13[1,i1] + a10[1, 129]
    a13[1,i1] = a13[1,i1] + a10[2, 127]
    a13[1,i1] = a13[1,i1] + a10[2, 128]
    a13[1,i1] = a13[1,i1] + a10[2, 129]
    a13[1,i1] = a13[1,i1] + a10[3, 127]
    a13[1,i1] = a13[1,i1] + a10[3, 128]
    a13[1,i1] = a13[1,i1] + a10[3, 129]
    if (i1 > 0)
        r5=a13[1, i1]/a13[1,0]
    endif
    message(1,30,r5)
    a13[0,i1] = a10[127, 222]
    a13[0,i1] = a13[0,i1] + a10[127, 223]
    a13[0,i1] = a13[0,i1] + a10[127, 224]
    a13[0,i1] = a13[0,i1] + a10[128, 222]
    a13[0,i1] = a13[0,i1] + a10[128, 223]
    a13[0,i1] = a13[0,i1] + a10[128, 224]
    a13[0,i1] = a13[0,i1] + a10[126, 222]
    a13[0,i1] = a13[0,i1] + a10[126, 223]
    a13[0,i1] = a13[0,i1] + a10[126, 224]
    if (i1 > 0)
        r6=a13[0,0] * r5
        a13[0,i1] = a13[0,i1] - r6
    endif

    i1 = i1 + 1
    i2 = i1 * 5
    i3 = i2 + 2700
    s2 = str(i3)
    s0 = s2 + '.0 GOTO'
    s0 = s0 + s5
    gpib write(11,s0)

```

```

i4 = i1 - 1
message (1,1,i1)
message (2,1,i3)
message (4,1,a13[0,i4])
endloop

s9 = 'b:\monocr1'
arr save file(a13,s9)
□
i1=0
set timeout (60)
arr discard (a10)
arr create (a10,256,256)

loop (100)

i1=i1+1
acquire(1,1,N)
a10=upload(c1,0,65536)
s8=str(i1)
s9='b:\test' + s8
; arr save file(a10,s9)
greyscale(a10,6,nowait,noclear)
read (s1,,)
if (s1 in ('q'))
    exitloop
endif
message (1,1,s9)

endloop□

```

#### B4. Get Blackbody And Sample Data:

```

set timeout(120)
arr discard(a10)
arr discard(a12)
arr discard(a13)
arr discard(a14)

arr create(a10, 256, 256)
arr create(a12, 5, 10)
arr create(a13, 5, 10)
arr create(a14, 5, 10)
a12 = 0.0
a13 = 0.0
a14 = 0.0

i0=0
loop(10)

s1='Set Blackbody at temp'
message (1,1,s1)
read(s1,,)
acquire(1,1,N)
a10 = upload(c1, 0, 65536)
a12[0, i0] = a10[127, 31]
a12[1, i0] = a10[127, 95]
a12[2, i0] = a10[127, 159]
a12[3, i0] = a10[127, 223]
a12[4, i0] = a10[1, 1]

s1='Set Sample at temp'
message (1,1,s1)
read(s1,,)
acquire(1,1,N)
a10 = upload(c1, 0, 65536)
a13[0, i0] = a10[127, 31]

```

```
a13[1, i0] = a10[127, 95]
a13[2, i0] = a10[127, 159]
a13[3, i0] = a10[127, 223]
a13[4, i0] = a10[1, 1]
```

```
s1='Set Sample at temp'
message (1,1,s1)
read(s1,,)
acquire(1,1,N)
a10 = upload(c1, 0, 65536)
a14[0, i0] = a10[127, 31]
a14[1, i0] = a10[127, 95]
a14[2, i0] = a10[127, 159]
a14[3, i0] = a10[127, 223]
a14[4, i0] = a10[1, 1]
i0=i0+1
```

```
endloop
```

```
s9 = 'b:\blackbo1'
arr save file(a12,s9)
```

```
s9 = 'b:\sample1'
arr save file(a13,s9)
```

```
s9 = 'b:\sample2'
arr save file(a14,s9)
```

## REFERENCES

1. M. A. Bramson, *Infrared Radiation*, Plenum press, New York, p. 686, (1968)
2. B. E. Saleh and M. C. Teich, *Fundamentals of Photonics*, John Wiley & Sons, New York, 1991, p. 405.
3. R. W. Boyd, *Radiometry and the Detection of Optical Radiation*, John Wiley & Sons, New York, 1983, pp. 43-49.
4. V. N. Snopko, "Methods of Optical Polychromatic Pyrometry," Institute of Physics. Academy of Sciences of the Belorussian SSR, Translations from Teplofizika Vysokikh Temperatur, Vol. 25, No. 5, p. 984, (1987)
5. V. N. Snopko, "Methods of Optical Polychromatic Pyrometry," Institute of Physics. Academy of Sciences of the Belorussian SSR, Translations from Teplofizika Vysokikh Temperatur, Vol. 25, No. 5, p. 980, (1987)
6. G. A. Hornbeck, "Optical Methods of Temperature Measurements", Applied Optics vol. 5 No. 2, pp. 179-186, Feb. 1966.
7. D. P. DeWitt, "inferring temperature from optical radiation measurements", Optical Engineering vol. 25, pp. 596-601, April 1986.
8. Y.W. Zhang et al., "Quantitative Measurements of Ambient Radiation, Emissivity and True Temperature of a Graybody: Methods and Experimental Results", Applied Optics vol. 25 No. 20, pp. 3683-3689, Oct. 1986.
9. Y. S. Touloukian and D. P. DeWitt, *Thermal Radiation Properties, Metallic Elements and Alloys*, IFI/Plenum, New York, 1970, pp. 3a-42a.
10. E. Hecht, *Optics*, 2nd Edition, Anderson-Wisley, p. 112, 1987
11. O. Staaf, C. G. Ribbing, and S. K. Andersson, "Temperature Dependence of the Band Emittance for Nongray Bodies," Applied Optics, Vol. 35 No. 31, pp. 6120-6125, 1 November 1996.

## REFERENCES (continued)

12. B.K. Tsai, *Dual-Wavelength Radiation Thermometry: Emissivity Compensation Algorithms*. MSME thesis, Prude University, West Lafayette, In, 1990.
13. B.K. Tsai, *Dual-Wavelength Radiation Thermometry: Emissivity Compensation Algorithms*. MSME thesis, Prude University, West Lafayette, In, 1990.
14. D.R. Snyder, "IR Imaging Spectrometer," USAF TR #:WLTR967049, Feb 1996
15. M.R. Descour, E.L. Dereniak, "Nonscanning no-moving-parts imaging spectrometer," International Symposium on Satellite Communication and Remote Sensing, Xi'an, China (September 1995).
16. A. Hirai, T. Inoue, K. Itoh and Yichioka," Application of Multiple-Image Fourier Transform Spectral Imaging to Measurement of Fast Phenomena," Optical Review, Vol. 1, No. 2, 1994, pp. 205-207.
17. W. F. Kosonocky, Et al., " Multi-Wavelength Imaging Pyrometer (M-WIP) for Semiconductor Process Monitoring and Control," WL-TR-95-8010, pp. 118-119. 1995.
18. D.R. Snyder, "IR Imaging Spectrometer," USAF TR #: WLTR967049, Feb 1996.
19. Hadland Photonics," The Ultra High Speed Imaging System," Specification Brochure on the Imacon 468, 20480 Pacifica Drive, Suite D, Cupertino, CA 95014.
20. D.R. Snyder, "Compact Imaging Spectrometer," USAF TR#: WLTR967047, Feb. 1996.
21. B. E. Saleh and M. C. Teich, *Fundamentals of Photonics*, John Wiley & Sons, New York, 1991, p. 362.
22. M. Born and E. Wolf, *Principles of Optics*, Sixth (Corrected) Edition , Pergamon Press, New York, 1991, pp. 510-514.
23. B. E. Saleh and M. C. Teich, *Fundamentals of Photonics*, John Wiley & Sons, New York, 1991, p. 362.

## REFERENCES (continued)

24. M.R. Descour, E.L. Dereniak, "Nonscanning no-moving-parts imaging spectrometer," *Imaging Spectrometry*, SPIE 2480-05 (April 1995).
25. B. E. Saleh and M. C. Teich, *Fundamentals of Photonics*, John Wiley & Sons, New York, 1991, p. 405.
26. B. E. Saleh and M. C. Teich, *Fundamentals of Photonics*, John Wiley & Sons, New York, 1991, p. 450.
27. B. E. Saleh and M. C. Teich, *Fundamentals of Photonics*, John Wiley & Sons, New York, 1991, p. 452.
28. Drude, P., "Bestimmung der Optischen Constanten der Metalle," *Ann. Physik* 64, 159, 1896; available as AFCRL translations "Demonstration of the optical constants of metals"
29. R. L. Shoemaker, "Notes from Lasers & Solid-State Devices course (Optical Sciences 511)," Optical Sciences Center Reading Room, Chapter 1, pp. 1-7, Spring 1993)
30. N. Peyghambarian, S. W. Koch and A. Mysyrowicz, *Introduction to Semiconductor Optics*, Prentice Hall, New Jersey, 1993, p. 59.
31. N. Peyghambarian, S. W. Koch and A. Mysyrowicz, *Introduction to Semiconductor Optics*, Prentice Hall, New Jersey, 1993, p. 56.
32. N. Peyghambarian, S. W. Koch and A. Mysyrowicz, *Introduction to Semiconductor Optics*, Prentice Hall, New Jersey, 1993, p. 59.
33. M. A. Bramson, *Infrared Radiation*, Plenum press, New York, pp. 535-552, (1968)
34. N. Peyghambarian, S. W. Koch and A. Mysyrowicz, *Introduction to Semiconductor Optics*, Prentice Hall, New Jersey, 1993, pp. 72-74.
35. N. Peyghambarian, S. W. Koch and A. Mysyrowicz, *Introduction to Semiconductor Optics*, Prentice Hall, New Jersey, 1993, pp. 60-61.

## REFERENCES (continued)

36. N. Peyghambarian, S. W. Koch and A. Mysyrowicz, *Introduction to Semiconductor Optics*, Prentice Hall, New Jersey, 1993, pp. 59-62.
36. D. P. DeWitt, "Comments on the Surface Characterization of real Metals," National Bureau of Standards pub, Vol. 12, Washington, D. C., pp141-144, 1978.
37. Y. S. Touloukian and D. P. DeWitt, *Thermal Radiation Properties, Metallic Elements and Alloys*, IFI/Plenum, New York, 1970, p. 26a.
38. M. A. Bramson, *Infrared Radiation*, Plenum press, New York, p. 686, (1968)
39. W. H. Press, S. A. Teukolsky, W. T. Vetterling and B. P. Flannery, *Numerical Recipes in C, The Art in Scientific Computing*, 2nd Edition, Cambridge University Press, pp. 683-688, 1992.
40. W. H. Press, S. A. Teukolsky, W. T. Vetterling and B. P. Flannery, *Numerical Recipes in C, The Art in Scientific Computing*, 2nd Edition, Cambridge University Press, pp. 683-688, 1992.
41. W. H. Press, S. A. Teukolsky, W. T. Vetterling and B. P. Flannery, *Numerical Recipes in C, The Art in Scientific Computing*, 2nd Edition, Cambridge University Press, pp. 683-688, 1992.
42. W. L. Wolfe and G. J. Zissis, *The Infrared Handbook*, 1978, Washington, D.C.: Office of Naval Research, Department of the Navy, pg. 2-77.

## **SECTION II.**

### **FOUR COLOR PYROMETRY FOR METAL EMISSIVITY CHARACTERIZATION.**

**MARK F. HOPKINS**

**(SPIE CONFERENCE PRESENTATION)**

# Four color pyrometry for metal emissivity characterization

Mark F. Hopkins  
Wright Laboratories, Armament Directorate  
Eglin AFB, Florida 32542

## ABSTRACT

Real time analysis of the IR spectrum is becoming increasingly important for the accurate measurement of the emissive characteristics of materials. The objective is once the emissivity is defined the temperature across a surface can be observed using passive IR techniques. It is both important to create accurate emissivity models as well as develop instrumentation that can acquire data accurately. With the advent of large high speed infrared detector arrays it has become possible to realize high resolution imaging spectrometers. To develop a model for materials such as metals we observe that the primary contribution to absorption characteristics can be attributed to the free electron plasma. It can be shown that for heated metals in thermal equilibrium the emissivity can be modeled as a second order polynomial. Consequently, a four color pyrometer can be used to accurately determine emissivity profile so that the true temperature can be determined.

## 1. INTRODUCTION

Over the past few years I have been working in the area of energetic materials pyrometry. I have found a great need for accurate temperature measurement for events such as the internal combustion in engines; materials deformation in metal processing; and detonating or deflagrating explosives. For these environments the objects that we are interest in are moving at high rates. In addition the temperature may also be moving at high rates; on the order of hundreds of degrees per millisecond. After an extensive survey of the technologies that could possibly solve some of this need I found little that is applicable to the energetic environment.

In recent years the inclusion of temperature effects in high speed deformation models has become more critical. The Wright laboratory armament directorate has been working to develop accurate models that predict penetrator type weapons deformation as the projectile encounters harden structures. The work presented in this paper is in the support of temperature profilometry of the metal casing material used in penetrator weapons. It is the intent of this paper to develop the theory leading to an accurate model of emissivity and to substantiate this model with experimental data.

## 2. BACKGROUND

As energy is delivered to a stricture at first it undergoes elastic deformation and will return to its original condition after the force is released. When enough force has been applied the material it reaches its "yield point" and the structure will deform plastically until it breaks. After the yield point is reached the stricture will not return to its original condition after the force is released. Consequently, work has been done to the structure in the form of material realignment and the generation of heat energy. In fact most of the deformation energy gets turned into heat and this heat energy modifies how the material will plastically deform. If the emissivity of the material is known radiometric techniques can be used to determine the surface temperature passively.

Methods for determining the surface temperature of heated material using optical pyrometers has often been based on assumptions that lead to erroneous results. The primary problems here is the uncertainties in the collected optical energy. Emissivity, atmospheric transmission, detector non-linearities etc. can all affect the amount of energy collected depending on the wavelength and bandwidth the measurement was made. Often the problem can be reduced to an uncertainty in Emissivity<sup>1</sup>. Emissivity is often characterized with a  $M^{th}$  order polynomial with

$$\epsilon_{eff}(\lambda) = a_{M+1}\lambda^M + a_M\lambda^{M-1} + a_{M-1}\lambda^{M-2} + \dots + a_1,$$

where the  $\alpha$ 's are unknown constants that describe emissivity behavior. If for instance a given material had a constant emissivity we would need to determine  $\alpha_1$  where all the other  $\alpha$ 's would be identically zero. Consequently, we would require two spectral measurements to determine temperature. Accordingly, if an  $M^{\text{th}}$  order polynomial provides a given materials emissivity profile we will require a minimum of  $M+2$  spectral measurements. However, the instrumentation errors increase strongly as  $M$  increases<sup>2</sup>, consequently, it is very important to limit the number of spectral measurements by use of simple models.

### 3. BLACKBODY RADIATION

Light emitted from solids under conditions of thermal equilibrium and in the absence of any other external sources, is known as thermal light. In this section I will attempt to validate the thermal equilibrium assumption for the high speed application. The thermal light derivation done here will closely follow that which is done in Fundamentals of Photonics<sup>3</sup>. Consider a cavity of unit volume whose walls have many atoms that have two energy states that are separated by energy difference  $h\nu$ . The cavity will support broadband radiation. Now let  $N_1$  and  $N_2$  representing the number of atoms per unit volume occupying energy levels one and two. Spontaneous emission creates radiation in the cavity, assuming one atom is at energy level two. Subsequently absorption and stimulated emission can occur. The three states exist in equilibrium when steady state is reached. We assume that there are an average number of photons per radiation mode  $\bar{n}$ .

We first consider the spontaneous emission rate and then we will move on to absorption and stimulated emission. The probability that an atom in the upper energy state undergoes spontaneous emission into any of the modes within the time increment from  $t$  to  $t + \Delta t$  is  $P_{sp} \Delta t = \Delta t / t_{sp}$ . There are  $N_2$  such atoms and the average number of photons emitted in  $\Delta t$  seconds is therefor  $N_2 \Delta t / t_{sp}$ . This is also the number of atoms that leave level 2 during the time interval. Consequently the rate that atoms increase in level 2 due to spontaneous emission is given by,

$$\frac{dN_2}{dt} = -\frac{N_2}{t_{sp}}$$

The solution is a exponential decaying function as a function of initial state  $N_{02}$  at time equals zero.

$$N_2 = N_{02} e^{\left(\frac{-t}{t_{sp}}\right)}$$

In the presence of radiation absorption and stimulated emission will occur. This changes the populations of  $N_1$  and  $N_2$ . Lets consider the absorption first. Since there are  $N_1$  in level one capable of absorbing, the rate of increase of the population of atoms in the upper level due to absorption is,

$$\frac{dN_2}{dt} = \frac{N_1 \bar{n}}{t_{sp}}$$

In a similar way the stimulated emission can be written as,

$$\frac{dN_2}{dt} = -\frac{N_2 \bar{n}}{t_{sp}}$$

As you can see the absorption and spontaneous rates are proportional to the average number of photons in each mode.

We can now write the rate equation for the overall process as,

$$\frac{dN_2}{dt} = -\frac{N_2}{t_{sp}} + \frac{N_1 \bar{n}}{t_{sp}} - \frac{N_2 \bar{n}}{t_{sp}}$$

Notice that this equation does not include transitions to other than the two levels, however, adding more levels is a trivial extension when we are in thermal equilibrium. In steady state the rate of change the levels will be zero. Consequently, we have

$$\frac{N_2}{N_1} = \frac{\bar{n}}{1 + \bar{n}}$$

We know that we are in thermal equilibrium and therefore we know that the populations obey a Boltzman distribution, i.e.,

$$\frac{N_2}{N_1} = e^{-\left(\frac{h\nu}{k_B T}\right)}$$

and we can now write,

$$\bar{n} = \frac{1}{e^{\left(\frac{h\nu}{k_B T}\right)} - 1}$$

The average energy  $\bar{E}$  of each mode in this situation will be simply  $\bar{n}h\nu$ , so that

$$\bar{E} = \frac{h\nu}{e^{\left(\frac{h\nu}{k_B T}\right)} - 1}$$

Multiplying this expression by the modal density  $8\pi\nu^2/c^3$  we have the blackbody radiation law

$$M_\nu = \frac{8\pi h\nu^3}{c^3 \left( e^{\left(\frac{h\nu}{k_B T}\right)} - 1 \right)}$$

We have derived the relation above under the assumption that we could assume thermal equilibrium. Let me now see if this assumption is a good one. If the temperature changes from  $T_1$  to  $T_2$  During the time interval  $\Delta t$  the change in the populations will be related as,

$$\Delta N_2 = -\Delta N_1$$

If ten atom move to level two then level one loses ten atoms. We can also write

$$\Delta N_2 = \left[ \frac{\bar{n}}{1 + \bar{n}} N_1 \right]_{T_2} - \left[ \frac{\bar{n}}{1 + \bar{n}} N_1 \right]_{T_1}$$

For our purposes we will be looking at objects at about 500 K. If the temperature raises by 100° and our operational wavelength is at three microns we can write

$$\Delta N_2 \approx [\bar{n}N_1]_{T2=600} - [\bar{n}N_1]_{T2=500}$$

We can't solve this equation without knowledge of the population of level one, however, we can ballpark the range of  $\Delta N_2$ . In the equation above we know that the first term is larger than the second term and that they are both positive. Dropping the second term we can write

$$\Delta N_2 < [\bar{n}N_1]_{T2=600} = 10^{-4} N_1.$$

We can also write the population of level two in terms of level one as

$$N_2 \approx [\bar{n}N_1]_{T2=500} \approx 10^{-5} N_1.$$

and

$$\Delta N_2 < N_2$$

Consequently, if the time of our observation is one microsecond and the relaxation time is  $10^{-14}$  seconds then the changing term is negligible, i.e.,

$$\frac{dN_2}{dt} = -\frac{N_2}{t_{sp}} + \frac{N_1\bar{n}}{t_{sp}} - \frac{N_2\bar{n}}{t_{sp}} \approx -\frac{N_2}{t_{sp}}$$

and

$$dN_2 \approx \frac{10\Delta t N_2}{t_{sp}} = 10^{-9} N_2$$

Therefore,

$$\frac{dN_2}{dt} = 0$$

and the steady state assumption is validated. It appears as though the blackbody radiation law will hold true until the relaxation time approaches the camera integration time.

#### 4. EMISSIVITY USING A FREE ELECTRON MODEL

We have looked the characteristic manner that a ideal solid generates its IR spectrum and now I divert our attention to the characterization of a metals absorption spectrum and consequently its emissivity. Here I will model the metal as an electron plasma with characteristic relaxation time and effective mass. This model does show promise to accurately model emissivity. In equilibrium according to Kirkoff's law the absorption of a material is equivalent to the emissivity. Consequently if we can determine the absorption characteristics of a materiel we know the emissivity characteristics, at least if the temperature is not changing quickly. Since much of our application is considering the properties of heated metals I will obtain the absorption relationship for a simple metal. Test results will support the accuracy of this technique.

The earliest attempts to predict the optical properties of metals were made by Lorentz and Durde<sup>4</sup>, who assumed the metal to contain electrons which were essentially free to move under the influence of the electric field induced by the incident

electromagnetic wave. These free electrons are the valence electrons in the outer shell of the atoms constituting the metal. When the wave is incident upon its surface, an oscillating electric field parallel to the surface is induced in the metal and the free electrons will oscillate under the influence of this field at the frequency of the incident wave. To describe the optical behavior requires two parameters: the number density of free electrons,  $n$ , being excited by the induced field, and the average time (relaxation time  $\tau$ ) between collisions of the electron with the atomic lattice. This is called the Drude Free Electron model. If the assumption can be made that  $\omega\tau \ll 1$  then a simplified model can be generated.

For many metals, particularly at higher temperatures and for relatively high purity, the electrical receptivity is proportional to temperature; through integration of the emissivity equation it can be shown that the normal total emissivity is proportional to the first power of the temperature<sup>5</sup>. To obtain the absorption characteristic we need to determine the polarization of the material from which we can derive the dielectric function. Using some well known relations for coefficient of absorption in terms of dielectric function we can derive the dependence with wavelength. Let us first assume that the metal crystal structure consists of charges (electrons) that respond to an electric field,  $E(t)$ , polarized in the  $x$  direction. We can write the equations of motion for each electron in the field using Newton's second law

$$m_e \frac{d^2 x(t)}{dt^2} + \frac{m_e}{\tau} \frac{dx(t)}{dt} = -eE(t)$$

where  $x(t)$  is the electron displacement from equilibrium,  $\tau$  is the relaxation time and  $m_e$  is the effective mass of an electron. Notice we have neglected the nucleus motion effect known as the dipole approximation. The second term of the above equation represents the damping due to collisions with ions. Notice that since the electrons in a metal are free to conduct there is no restoring force in the above equation.

If we assume a single wavelength interacting at frequency,  $\omega$  we have

$$E(t) \cong E_0 e^{-i\omega t}$$

Accordingly the position of the electron will follow the field oscillation and can be written as,

$$x(t) \cong x_0 e^{-i\omega t}$$

Substituting into the first equation and dividing both sides by  $e^{-i\omega t}$ , we have

$$-m_e \omega^2 x_0 - m_e \frac{i\omega}{\tau} x_0 = -eE_0$$

or

$$x_0 = \frac{e\tau}{m_e \omega} E_0 \frac{\omega\tau - i}{\omega^2 \tau^2 + 1}$$

This is a solution to the equation of motion differential equation for which a general oscillator model can be derived.

$$\epsilon(\omega) = \epsilon_\infty - \frac{4\pi n e^2 \tau}{m_e \omega} \frac{\omega\tau - i}{\omega^2 \tau^2 + 1}$$

The  $\epsilon_\infty$  term is referred to as the background dielectric function and is due to the displacement of bound electrons. This formula is known as the Drude oscillator model dielectric function and can also be written as

$$\epsilon(\omega) = \epsilon_{\infty} - \frac{4\pi n e^2 \tau^2}{m_e} \frac{1}{\omega^2 \tau^2 + 1} + i \frac{4\pi n e^2 \tau}{m_e \omega} \frac{1}{\omega^2 \tau^2 + 1}$$

Now we can go about solving for the coefficient of absorption in terms of dielectric function. This relationship is derived in many texts as is

$$\alpha(\omega) = \frac{\omega}{c n(\omega)} \epsilon'(\omega)$$

and

$$n(\omega) = \sqrt{\frac{1}{2} \left( \epsilon' + \sqrt{(\epsilon')^2 + (\epsilon'')^2} \right)}$$

Accomplishing the appropriate substitutions we have

$$\alpha(\omega) = \frac{\sqrt{2} \omega \epsilon_{\infty}'' - \frac{\sqrt{2} \omega 4\pi n e^2 \tau}{m_e \omega} \frac{1}{\omega^2 \tau^2 + 1}}{\sqrt{\epsilon_{\infty}' - \frac{4\pi n e^2 \tau^2}{m_e} \frac{1}{\omega^2 \tau^2 + 1} + \sqrt{\left( \epsilon_{\infty}' - \frac{4\pi n e^2 \tau^2}{m_e} \frac{1}{\omega^2 \tau^2 + 1} \right)^2 + \left( \epsilon_{\infty}'' - \frac{4\pi n e^2 \tau}{m_e \omega} \frac{1}{\omega^2 \tau^2 + 1} \right)^2}}}$$

In this form it seems rather formidable, however we can look at it a little more simply, or at least how we may go about solving for the unknowns. There are five unknown constants in the system,  $\epsilon_{\infty}'$ ,  $\epsilon_{\infty}''$ ,  $\tau$ ,  $m_e$  and  $n$ . Consequently, with unknown temperature there will be six unknowns and a six color pyrometer will be required. In addition the system of six equations will be nonlinear and require a nonlinear optimization technique such as proposed by Levenberg and Marquard. These types of algorithms tend to take a long time to optimize and often get caught in local minim's. There is, however, some simplifications that can be done for our application. Since polished metals have very few bound electrons that interact in the 3 to 5  $\mu\text{m}$  energy band we can assume that  $\epsilon_{\infty}$  is small, therefore

$$\alpha(\omega) = \frac{\frac{\sqrt{2} \omega 4\pi n e^2 \tau}{m_e \omega} \frac{1}{\omega^2 \tau^2 + 1}}{\sqrt{-\frac{4\pi n e^2 \tau^2}{m_e} \frac{1}{\omega^2 \tau^2 + 1} + \sqrt{\left( \frac{4\pi n e^2 \tau^2}{m_e} \frac{1}{\omega^2 \tau^2 + 1} \right)^2 + \left( \frac{4\pi n e^2 \tau}{m_e \omega} \frac{1}{\omega^2 \tau^2 + 1} \right)^2}}}$$

or by rearranging terms can be written as

$$\alpha(\omega) = \frac{\sqrt{\frac{8\pi n e^2}{m_e} \frac{1}{\omega^2 \tau^2 + 1}}}{\sqrt{\sqrt{1 + \frac{1}{\omega^2 \tau^2}} - 1}}$$

Conductivity measurements have shown that the relaxation time for metals is in the range of  $10^{-13}$  to  $10^{-15}$  seconds<sup>6</sup>. Since our sensor is operating at 3 to 5  $\mu\text{m}$  then  $\tau^2\omega^2 \geq 36$  when  $\frac{1}{\omega^2\tau^2}$  is small and with using the binomial expansion approximation we have,

$$\alpha(\omega) = \sqrt{\frac{16\pi ne^2}{m_e} \frac{\omega^2\tau^2}{\omega^2\tau^2 + 1}}$$

or

$$\alpha(\omega) = \sqrt{\frac{16\pi ne^2}{m_e}} \sqrt{\frac{1}{1 + \frac{1}{\omega^2\tau^2}}}$$

While we have simplified the equation it is still nonlinear and suffers from the same problem of the previous equation. We can expand this equation in a binomial series expansion and absorption can be written as,

$$\alpha(\omega) = \sqrt{\frac{16\pi ne^2}{m_e}} \left[ 1 - \frac{1}{2\omega^2\tau^2} + \frac{3}{8} \frac{1}{\omega^4\tau^4} \right]$$

or,

$$\alpha(\omega) = \sqrt{\frac{16\pi ne^2}{m_e}} \left[ 1 - \frac{1}{8\pi^2 c^2 \tau^2} \lambda^2 + \frac{3}{128 \pi^4 c^4 \tau^4} \lambda^4 \right]$$

The third term is very small and can be left out. Therefore a second order polynomial should provide a good model for our calculations in temperature emissivity decoupling. As you can see there is no  $\lambda$  term in the equation and experimental results in the past have shown that there is a small amount of dependence on the first order term. However, the third order terms and higher have been essentially nonexistent in the data previously collected. While I these results will again be encountered in this research I will later address the impact on accuracy from the neglecting of these terms.

## 5. EXPERIMENTAL RESULTS

To validate the emissivity model proposed in this paper I set up an experiment using a heated plate of aluminum and copper ( $T=500^\circ\text{K}$ ) and a fourier transform IR spectrometer manufactured by Boman. Let me first start with a discussion of the technique used for the solution of the system of equations. The emissivity can be expanded to as many orders as we have spectral bins in our spectrometer. However, due to computational rounding errors the calculation of coefficients beyond the seventh order are erroneous. This should work fine for the validation here because the series should converge after the second term. The experiment calculated the eight coefficients for the emissivity model for the aluminum and copper samples, however, to simplify the discussion I will use a second order model. The four equations of the system are

$$\Phi_{\text{pixel}}(\lambda_i, T) = \frac{c_1(a_1\lambda^2 + a_2\lambda + a_3)}{\lambda_i^5 \left( e^{\frac{c_2}{\lambda_i T}} - 1 \right)} \text{Re}(\lambda_i) d\lambda_i \quad \text{for } i=1, 2, 3 \text{ \& } 4$$

where:

$c_1 = \text{const.}$

$c_2 = \text{const.}$

$T = \text{Temperature of target}$

$\lambda = \text{Wavelength in microns}$

$\text{Re}(\lambda) = \text{Response of detector/filter}$

$d\lambda = \text{Differential wavelength}$

Rearranging the terms we have

$$\Phi_{\text{pixel}}(\lambda_i, T) = a_1 \int \frac{c_1 \text{Re}(\lambda_i) d\lambda_i}{\lambda_i^3 \left( e^{\frac{c_2}{\lambda_i T}} - 1 \right)} + a_2 \int \frac{c_1 \text{Re}(\lambda_i) d\lambda_i}{\lambda_i^4 \left( e^{\frac{c_2}{\lambda_i T}} - 1 \right)} + a_3 \int \frac{c_1 \text{Re}(\lambda_i) d\lambda_i}{\lambda_i^5 \left( e^{\frac{c_2}{\lambda_i T}} - 1 \right)}$$

Since the temperature is held constant then any three of the four equations has a linear solution. The first three equations can be written

$$\Phi_{\text{pixel}}(\lambda_i, T) = a_1 \int c_1(T) \frac{\text{Re}(\lambda_i) d\lambda_i}{\lambda_i^3} + a_2 \int c_2(T) \frac{\text{Re}(\lambda_i) d\lambda_i}{\lambda_i^4} + a_3 \int c_3(T) \frac{\text{Re}(\lambda_i) d\lambda_i}{\lambda_i^5}$$

Each of the integrals is evaluatable and can be written as

$$\Phi_{\text{pixel}}(\lambda_i, T) = a_1 I_{1_i}(T) + a_2 I_{2_i}(T) + a_3 I_{3_i}(T)$$

or can be rewritten in linear algebra form as

$$\begin{bmatrix} \Phi_{\lambda_1} \\ \Phi_{\lambda_2} \\ \Phi_{\lambda_3} \end{bmatrix} = \begin{bmatrix} I_{1_1}(T) & I_{2_1}(T) & I_{3_1}(T) \\ I_{1_2}(T) & I_{2_2}(T) & I_{3_2}(T) \\ I_{1_3}(T) & I_{2_3}(T) & I_{3_3}(T) \end{bmatrix} \cdot \begin{bmatrix} a_1 \\ a_2 \\ a_3 \end{bmatrix}$$

The solution for the unknown  $a_1$ ,  $a_2$  &  $a_3$  coefficients is

$$\begin{bmatrix} a_1 \\ a_2 \\ a_3 \end{bmatrix} = \begin{bmatrix} I_{1_1}(T) & I_{2_1}(T) & I_{3_1}(T) \\ I_{1_2}(T) & I_{2_2}(T) & I_{3_2}(T) \\ I_{1_3}(T) & I_{2_3}(T) & I_{3_3}(T) \end{bmatrix}^{-1} \cdot \begin{bmatrix} \Phi_{\lambda_1} \\ \Phi_{\lambda_2} \\ \Phi_{\lambda_3} \end{bmatrix}$$

The procedure of inverting a matrix is fairly complicated. There many techniques for inverting a matrix and there usage depends on the specific application. I have chosen the Gaussian elimination method because it provides the greatest versatility and it is easily implemented. The data from the spectrometer was substituted into the above equation the solution matrix was attained. What we saw was that coefficients after the square term were negligible. The inclusion of the other terms constitute a  $\pm 7\%$  variation in the calculated emissivity. Keeping the last three terms and calculating the temperature from a ninth equation I arrived at a 575°K prediction and seventy five degrees off the true temperature.

## 6. CONCLUSIONS

The fundamental process of passively predicting the temperature of heated materials inevitably will be limited by the accuracy of the model for emissivity and instrumentation noise. The theory has shown that metal materials have an emissivity that follow a second order polynomial with an absent linear term. However, the experimental data has shown that the linear term is significant and can't be left out of the model. It seems likely that a four color pyrometer will be able to collect all the basic data needed to estimate temperature accurately. The source of the error in temperature prediction of the experiment performed for this paper is primarily due to instrumentation calibration inaccuracies. To eliminate this source of error new instrumentation is required to be developed. This will be the subject of further work.

---

<sup>1</sup> V.N Snopko, "Methods of optical polychromatic pyrometry," Plenum Publishing Co., 1988. pp.724-729.

<sup>2</sup> Same as 1

<sup>3</sup> SaleH B. and Teich M., "Fundamentals of Photonics," Wiley and Sons, New York, pp. 450-454.

<sup>4</sup> Drude, P., "Bestimmung der Optischen Constanten der Metalle," Ann. Physik 64, 159, 1896; available as AFCRL translations "Demonstration of the optical constants of metals".

<sup>5</sup> Touloukian Y. S. and DeWitt D. P., "Thermal Properties of metals-Metallic Elements and Alloys," IFI/Plenum, New York, Vol. 7, pp. 22-27.

<sup>6</sup> Peyghambarian N., Konk S. W. and Mysyrowicz A., "Introduction to semiconductor optics," Prentice-Hall, New Jersey, 1993.

**SECTION III.**

**BEHIND PANEL DEBRIS TEMPERATURE PROFILOMETRY.**

**EUSTACE L. DERINIAK**

**AND**

**JOHN P. GARCIA**

**UNIVERSITY OF ARIZONA GRANT REPORT  
(F49620-95-1-0456)  
MARCH 1998**

**Behind Panel Debris Temperature Profilometry**

**By**

**EUSTACE L. DERENIAK**

**&**

**JOHN P. GARCIA**

**Optical Sciences Center**

**University of Arizona**

**Tucson, Arizona 85721**

**for**

**U.S. Air Force Office of Scientific Research**

**110 Duncan Ave., Suite B115**

**Bolling AFB, DC 20332-0001**

**March, 1998**

**Contract No. F49620-95-1-0456**

**The views, opinions, and/or findings contained in this report are those of the the authors and should not be construed as an official Department of the Air Force position, policy, or decision, unless so designated by other documentation.**

## **Introduction:**

This report documents the research methods used and data compiled during this project. The development of algorithms to extract spectral emissivity and temperature values from radiometric data taken in several bands in the 3-5 micron region is described. In addition, progress toward an instrument capable of providing the raw data for these algorithms for each pixel in a single snapshot image is detailed.

## **I. Tasks:**

### **A) Search available literature for relevant spectral emissivity studies.**

The literature search was completed. Our findings indicated that the spectral emissivity of many metals in the 3 - 5 micron region could be accurately represented by a third order polynomial in wavelength:

$$\varepsilon(\lambda) = a + b \cdot \lambda + c \cdot \lambda^2$$

As shown in Fig. 1, Aluminum, and Steel Alloy show a parabolic dependency of emissivity with wavelength. Ceramics and dielectric materials however, exhibit more complicated spectral behavior as shown for brick and fireclay in Fig. 2. Since composite armor can produce projectile debris consisting of ceramic and metal, a higher order polynomial approximation of emissivity must be used. In addition, a higher order expression allows the identification of emission lines from combustion processes which could perturb the temperature solution. To do otherwise would be to adapt the problem to an existing technology when competent engineering practice demands the opposite approach.

B) Determine the feasibility of using spectral radiance data to find absolute temperature without prior knowledge of spectral emissivity.

Originally, a polynomial fit of spectral emissivity was combined with the Levenberg-Marquardt algorithm<sup>1</sup> to solve a system of equations of the form:

$$\text{Kcal} \cdot \int_{\lambda_1 - \Delta\lambda}^{\lambda_1 + \Delta\lambda} \frac{\varepsilon(\lambda) \cdot 2 \cdot \pi \cdot c}{\lambda^4 \cdot \left( e^{\frac{h \cdot c}{\lambda \cdot k \cdot T}} - 1 \right)} d\lambda = \text{Data}_{\lambda_1}$$

$$\text{Kcal} \cdot \int_{\lambda_2 - \Delta\lambda}^{\lambda_2 + \Delta\lambda} \frac{\varepsilon(\lambda) \cdot 2 \cdot \pi \cdot c}{\lambda^4 \cdot \left( e^{\frac{h \cdot c}{\lambda \cdot k \cdot T}} - 1 \right)} d\lambda = \text{Data}_{\lambda_2}$$

Where Kcal is a known radiometric calibration constant and  $\text{Data}_{\lambda}$  is the photon irradiance (photons/cm<sup>2</sup>-second) in each band. The integrals on the left-hand side

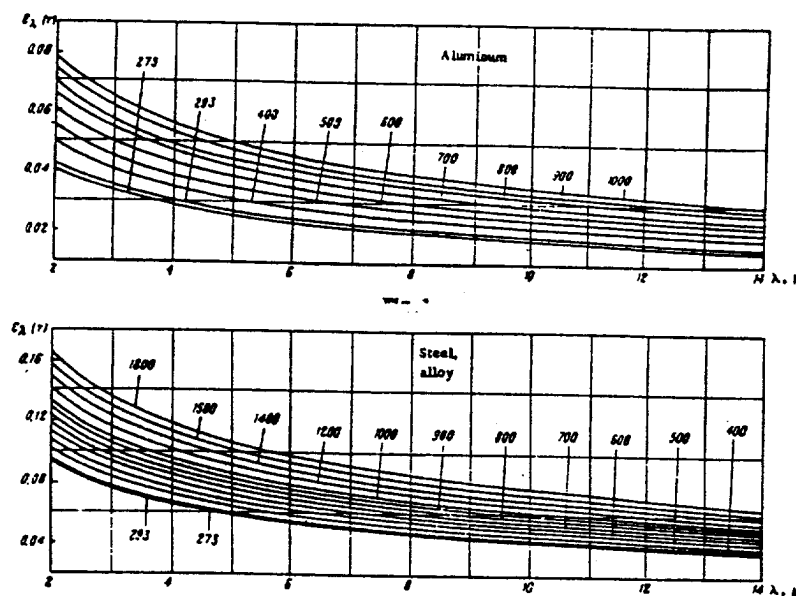


Fig.1 Spectral emissivity of Aluminum (Top) and Steel Alloy<sup>2</sup>.

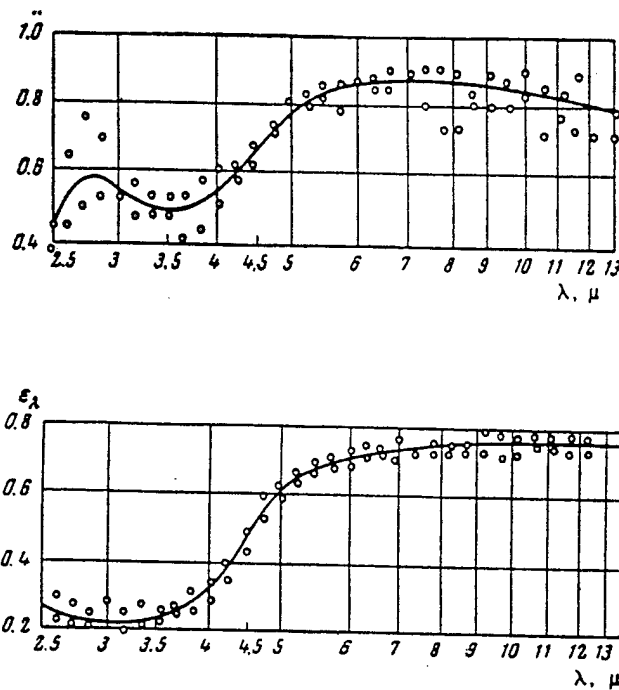


Fig. 2 Spectral emissivity of brick (Top) and fireclay 100 - 300 C<sup>2</sup>.

represent the calculated band irradiance, which is ideally equal to the measured band irradiance on the right. For a third order polynomial expression of emissivity, at least four such equations must be solved simultaneously for  $a$ ,  $b$ ,  $c$  and  $T$ .

In practice, the system can be solved only approximately. It was found during tests of the algorithm on simulated data with additive Gaussian noise that higher order polynomial expressions for  $\epsilon(\lambda)$  resulted in unacceptable susceptibility to noise. Since we were aiming for field images of projectile debris at small integration times, we anticipated noisy data. Therefore the polynomial fit approach was abandoned in favor of independent band averaged emissivities for each band. This resulted in a system of equations of the following form:

$$\begin{array}{c}
 \text{Kcal} \cdot \epsilon_1 \cdot \left[ \begin{array}{c} \lambda_1 + \Delta\lambda \\ \lambda_1 - \Delta\lambda \end{array} \right] \cdot \frac{2 \cdot \pi \cdot c}{\lambda^4 \cdot \left( e^{\frac{h \cdot c}{\lambda \cdot kT}} - 1 \right)} d\lambda = \text{Data}_{\lambda_1} \\
 \\
 \text{Kcal} \cdot \epsilon_2 \cdot \left[ \begin{array}{c} \lambda_2 + \Delta\lambda \\ \lambda_2 - \Delta\lambda \end{array} \right] \cdot \frac{2 \cdot \pi \cdot c}{\lambda^4 \cdot \left( e^{\frac{h \cdot c}{\lambda \cdot kT}} - 1 \right)} d\lambda = \text{Data}_{\lambda_2}
 \end{array}$$

Effectively, we chose to model  $\epsilon(\lambda)$  by a rectangle function in each band and the entire spectral profile by several such bands as shown in Fig. 3. The astute reader will note that this system is inherently underdetermined due to the presence of one more variable (  $T$  ) than the number of equations. Accordingly, additional constraints such as positivity on  $\epsilon_1$ ,  $\epsilon_2$  etc. had to be applied and several different initial values of temperature had to be used as starting points. Further computer simulations indicated that Levenberg-Marquardt, applied to such a system, tended to produce inaccurate results owing to the algorithm's tendency to converge to local, rather than absolute, minima. Accordingly, globally convergent algorithms were investigated and tested. After considerable trial and error, Broyden's Method proved to give good noise immunity and reasonably accurate results when applied to simulated data with noise<sup>3</sup>. As with Levenberg-Marquardt, several different seed values of  $T$  over the interval of interest had to be used, then the algorithm automatically chose the best solution based on a least-squares merit function. An attempt to fit one fewer emissivity value than the number of data points, thereby producing an adequately determined system, proved unsuccessful.

Having obtained good results with this technique on simulated noisy data, we tested the program on real data generated with the experimental setup shown in Fig. 4. We simulated a target of unknown emissivity and temperature by placing a known spectral filter in the radiation path from a blackbody set at a known temperature. Since we had not yet manufactured an IR disperser, the output of the laboratory blackbody was passed through a monochromator to produce radiation in six contiguous bands with center wavelengths of 3.20, 3.44, 3.68, 3.92, 4.16 and 4.40 microns. The monochromator output was first chopped and then sent to a 256 x 256 pixel PtSi camera operating at 78 K. This was the imager we intended to use in the actual IR snapshot imaging spectrometer. A magnified image of the exit slit of the monochromator was sent via RS-170 to a video monitor and subsequently to a lock-in amplifier to extract the signal magnitude. Since we were unable to capture video frames from the camera with frame grabbers currently in our lab, the use of a lock-in was necessary to separate the signal of interest from the various components of the PtSi imager's composite video output.

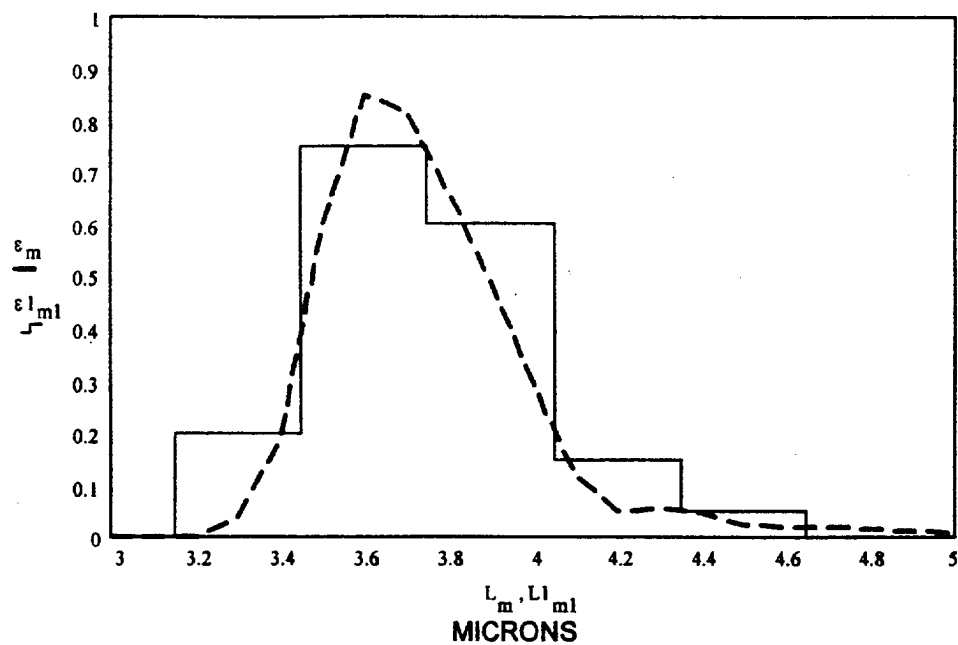


Fig. 3 Rectangle approximation of spectral emissivity.

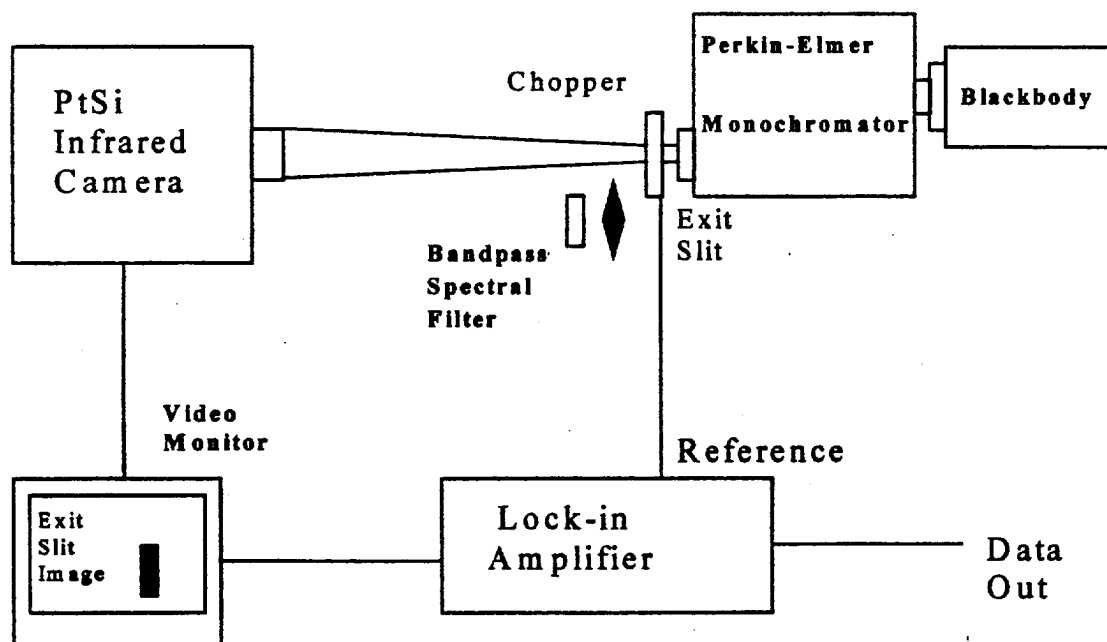


Fig. 4 Experimental setup for unknown target measurements.

Readings were taken in each band with the blackbody set for 873 K to obtain a calibration of the system as a whole. Then the blackbody temperature was increased to 973 K ; a previously scanned bandpass filter was placed in the radiation path after the chopper and the data collection process was repeated. The filter transmission versus wavelength was used to simulate a target with unknown spectral emissivity characteristics at an unknown temperature. Both the system calibration data and the target data were processed with a program that incorporated Broyden's Method. The results are shown in Fig. 5 below.

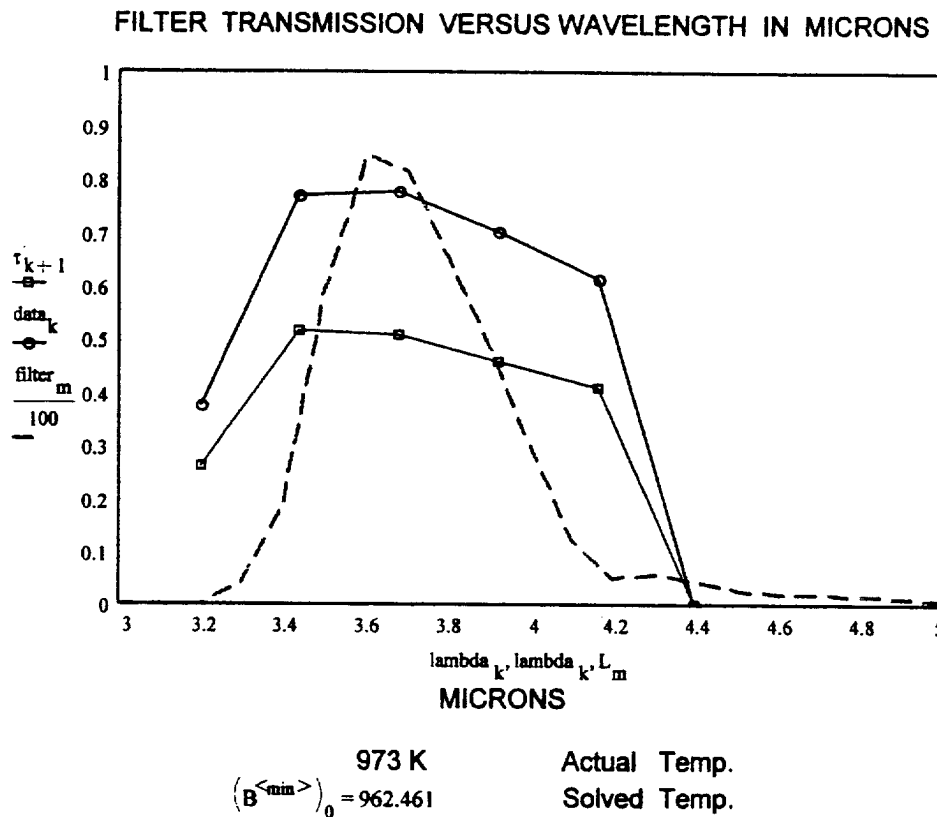


Fig. 5 Results of the emissivity-temperature algorithm. The bandpass filter transmission is the continuous dashed line; the measured data for the six spectral bands is the upper trace with circles; the output of the program is the lower trace with squares.

The algorithm converged to a temperature of 962.5 K which is 10.5 K lower than the actual source temperature, thereby proving the ability to recover temperature with good accuracy. The lack of a good emissivity fit was probably due to inadequate wavelength calibration of the monochromator.

### C) Design and manufacture diffractive elements for the 3 to 5 micron region.

This task has been completed. Prior to the design and manufacture of dispersive elements, it was strongly suggested, by the contract monitor, that we spend several months developing a model of the IR Computed Tomography Imaging Spectrometer. Our extensive experience with the visible version of this instrument was apparently not applicable to the 3 – 5 micron band. We then used this model as a starting point to optimize the disperser design while recognizing that trial and error experiments were inevitable. The optical layout upon which this model is based appears below.

#### OPTICAL SYSTEM LAYOUT

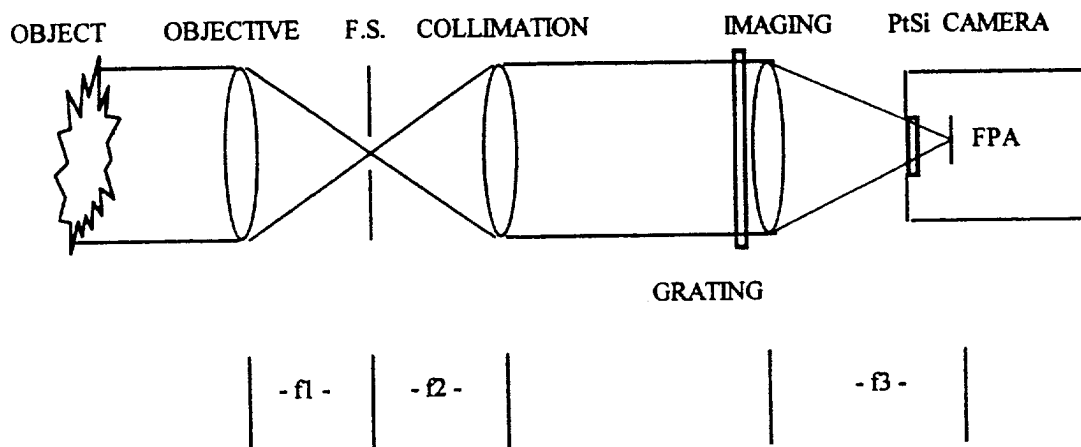


Fig. 6. Simplified optical layout of the IR CTIS system showing the focal lengths of the objective lens, the collimating lens and the final imaging lens which is actually attached to the PtSi camera dewar. The field stop (F.S.) is located at the focal plane of both the objective lens and the collimating lens to reduce stray light.

A Fourier optics approach was chosen for the system model to account for the diffractive effects of the grating. The method is an extension of a incoherent diffraction calculation presented by Goodman to two-dimensional binary phase gratings<sup>4</sup>. A two dimensional binary phase grating is one which is etched into a transmissive material and has only two levels as shown schematically below in Fig. 7.

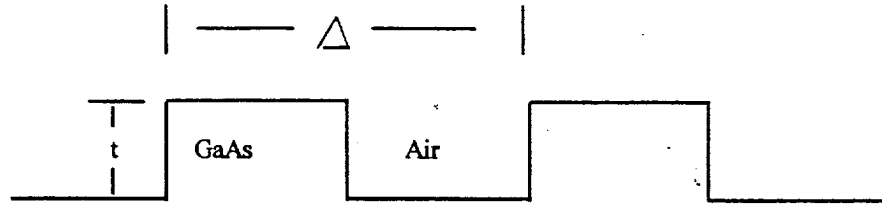


Fig. 7. Two-dimensional binary phase grating in cross section. The grating period is given by  $\Delta$  and the grating modulation thickness is given by  $t$ . From above, the grating looks like a pattern of square islands with the "moats" separating them as wide as the squares themselves. This particular pattern was chosen because it could be fabricated at the Optical Sciences Center in GaAs and required only a single mask and etch step.

Following and generalizing Goodman's model, we found for a one-dimensional sinusoidal phase grating coincident with a square aperture,

$$t(x_1, y_1) = \exp\left(\frac{j \cdot m(\lambda)}{2} \cdot \sin(2 \cdot \pi \cdot f_0 \cdot x_1)\right) \cdot \text{rect}\left(\frac{x_1}{L}\right) \cdot \text{rect}\left(\frac{y_1}{L}\right) \quad (1)$$

where

$t(x_1, y_1)$  = The pupil transmission function of the grating.

$m(\lambda) = 2\pi(n-1)t/\lambda$  is the phase modulation factor,  $n = 3.4$  for GaAs.

$f_0 = 1/\Delta$  is the grating frequency in line pairs per mm.

$l$  = The lateral dimensions of the square aperture.

and  $\text{rect}(x_1/l)\text{rect}(y_1/l)$  is a function which is 1 inside the aperture and 0 outside.

At this point, we chose only to model a one dimensional grating coincident with a square aperture and calculate the resulting diffraction pattern a distance  $z$  away. Effects

of the other optical components in the IR CTIS would be included later. To apply this result to a binary squarewave phase grating, we expanded the squarewave phase profile in a Fourier series to obtain:

$$t(x_1, y_1) = \exp \left[ \frac{j \cdot m(\lambda)}{2} \cdot \left( \frac{4}{\pi} \sum_n \frac{1}{n} \cdot \sin(2 \cdot \pi \cdot n \cdot f_0 \cdot x_0) \right) \right] \cdot \text{rect} \left( \frac{x_1}{L} \right) \cdot \text{rect} \left( \frac{y_1}{L} \right) \quad (2)$$

$$n = 1, 3, 5 \dots$$

which is equivalent to

$$t(x_1, y_1) = \prod_n \exp \left( \frac{2 \cdot j \cdot m(\lambda)}{\pi \cdot n} \cdot \sin(2 \cdot \pi \cdot n \cdot f_0 \cdot x_1) \right) \cdot \text{rect} \left( \frac{x_1}{L} \right) \cdot \text{rect} \left( \frac{y_1}{L} \right) \quad (3)$$

$$n = 1, 3, 5 \dots$$

Using the identity

$$\exp \left( j \cdot \frac{m(\lambda)}{2} \cdot \sin(2 \cdot \pi \cdot f_0 \cdot x_1) \right) = \sum_{q=-\infty}^{\infty} J_q \left( \frac{m(\lambda)}{2} \right) \cdot \exp(j \cdot 2 \cdot \pi \cdot q \cdot f_0 \cdot x_1) \quad (4)$$

we arrived at

$$t(x_1, y_1) = \prod_n \left[ \sum_{q=-\infty}^{\infty} J_q \left( \frac{2 \cdot m(\lambda)}{\pi \cdot n} \right) \cdot \exp(j \cdot 2 \cdot \pi \cdot q \cdot n \cdot f_0 \cdot x_1) \right] \cdot \text{rect} \left( \frac{x_1}{L} \right) \cdot \text{rect} \left( \frac{y_1}{L} \right) \quad (5)$$

$$n = 1, 3, 5 \dots$$

for the pupil transmittance function of a one-dimensional binary squarewave phase grating. The grating is a squarewave along  $x_1$  and constant along  $y_1$ . To find the Fraunhofer diffraction pattern a distance  $z$  away, we took the Fourier Transform of this expression, noting that multiplications become convolutions in the transform domain.

$$\begin{aligned}
 F(t; x_1, y_1) = & \left[ \sum_{q=-\infty}^{\infty} J_q \left( 2 \frac{m(\lambda)}{\pi} \right) \cdot \delta(f_x - q \cdot f_0, f_y) \right] \cdot \Theta \cdot \left[ \sum_{q=-\infty}^{\infty} J_q \left( 2 \frac{m(\lambda)}{3 \cdot \pi} \right) \cdot \delta(f_x - 3 \cdot q \cdot f_0, f_y) \right] \cdot \Theta \\
 & \cdot \left[ \sum_{q=-\infty}^{\infty} J_q \left( 2 \frac{m(\lambda)}{5 \cdot \pi} \right) \cdot \delta(f_x - 5 \cdot q \cdot f_0, f_y) \right] \cdot \Theta \cdot \left[ \sum_{q=-\infty}^{\infty} J_q \left( 2 \frac{m(\lambda)}{7 \cdot \pi} \right) \cdot \delta(f_x - 7 \cdot q \cdot f_0, f_y) \right] \cdot \Theta \\
 & L^2 \cdot \text{sinc}(L \cdot f_x) \cdot \text{sinc}(L \cdot f_y)
 \end{aligned} \tag{6}$$

where we truncated the expansion of the sine function to four terms for simplicity. For a unit amplitude plane wave incident upon the aperture, this transmission function is also the amplitude of the transmitted wave immediately behind the aperture.

$$F(u(x_1, y_1)) = F(t(x_1, y_1)) \tag{7}$$

We took advantage of the properties of convolution applied to delta functions, namely if

$$g(x) = \left[ \sum_{i=-\infty}^{\infty} a_1 \cdot \delta(x - i \cdot b_1) \right] \cdot \Theta \cdot \left[ \sum_{j=-\infty}^{\infty} a_2 \cdot \delta(x - j \cdot b_2) \right] \tag{8}$$

then

$$g(x) = \sum_{i=-\infty}^{\infty} \sum_{j=-\infty}^{\infty} a_1 \cdot a_2 \cdot \delta(x - i \cdot b_1 - j \cdot b_2) \tag{9}$$

and arrived at the following result.

$$F(u(x_1, y_1)) = L^2 \cdot \sum_{q_1=-\infty}^{\infty} \sum_{q_2=-\infty}^{\infty} \sum_{q_3=-\infty}^{\infty} \sum_{q_4=-\infty}^{\infty} J_{q_1} \left( \frac{2 \cdot m}{\pi} \right) \cdot J_{q_2} \left( \frac{2 \cdot m}{3 \cdot \pi} \right) \cdot J_{q_3} \left( \frac{2 \cdot m}{5 \cdot \pi} \right) \cdot J_{q_4} \left( \frac{2 \cdot m}{7 \cdot \pi} \right) \\
\cdot \operatorname{sinc} \left[ L \left( f_x - q_1 \cdot f_0 - 3 \cdot q_2 \cdot f_0 - 5 \cdot q_3 \cdot f_0 - 7 \cdot q_4 \cdot f_0 \right) \right] \cdot \operatorname{sinc} \left( L \cdot f_y \right) \quad (10)$$

Here the asterisk denotes multiplication.

The Fraunhofer diffraction pattern at a distance  $z$  from the aperture was found by taking the modulus squared of this expression and scaling the appropriate variables. The coordinate system in the Fraunhofer plane is denoted by  $x_0, y_0$ .

$$I(x_0, y_0) = \left( \frac{L^2}{\lambda \cdot z} \right)^2 \cdot \left[ \sum_{q_1=-\infty}^{\infty} \sum_{q_2=-\infty}^{\infty} \sum_{q_3=-\infty}^{\infty} \sum_{q_4=-\infty}^{\infty} J_{q_1} \left( \frac{2 \cdot m}{\pi} \right) \cdot J_{q_2} \left( \frac{2 \cdot m}{3 \cdot \pi} \right) \cdot J_{q_3} \left( \frac{2 \cdot m}{5 \cdot \pi} \right) \cdot J_{q_4} \left( \frac{2 \cdot m}{7 \cdot \pi} \right) \right]^2 \\
\cdot \left[ \operatorname{sinc} \left[ \frac{L}{\lambda \cdot z} \cdot (x_0 - q_1 \cdot f_0 - 3 \cdot q_2 \cdot f_0 - 5 \cdot q_3 \cdot f_0 - 7 \cdot q_4 \cdot f_0) \right] \cdot \operatorname{sinc} \left[ \frac{L}{\lambda \cdot z} \cdot (y_0) \right] \right]^2 \quad (11)$$

This result was applied to the situation of a unit amplitude plane wave incident on a two-dimensional binary phase grating coincident with a lens of focal length  $f_3$  to calculate the diffraction pattern at the focal plane.

$$I(x_0, y_0) = \left( \frac{L^2}{\lambda \cdot f_3} \right)^2 \cdot \prod_{(i=x, y)} \left[ \sum_{q_{1_i}=-\infty}^{\infty} \sum_{q_{2_i}=-\infty}^{\infty} \sum_{q_{3_i}=-\infty}^{\infty} \sum_{q_{4_i}=-\infty}^{\infty} J_{q_{1_i}} \left( \frac{2 \cdot m}{\pi} \right) \cdot J_{q_{2_i}} \left( \frac{2 \cdot m}{3 \cdot \pi} \right) \cdot J_{q_{3_i}} \left( \frac{2 \cdot m}{5 \cdot \pi} \right) \cdot J_{q_{4_i}} \left( \frac{2 \cdot m}{7 \cdot \pi} \right) \right]^2 \\
\cdot \left[ \operatorname{sinc} \left[ \frac{L}{\lambda \cdot f_3} \cdot (i_0 - q_{1_i} \cdot f_0 - 3 \cdot q_{2_i} \cdot f_0 - 5 \cdot q_{3_i} \cdot f_0 - 7 \cdot q_{4_i} \cdot f_0) \right] \right]^2 \quad (12)$$

Equation 12 describes the idealized case of a unity amplitude plane wave incident on a grating-lens system similar to the grating-imaging lens combination in the IR CTIS. By considering the diffraction properties of the other lenses in the system, we were able to modify (12) to characterize the whole system. To do this, we considered the case of an

extended object which produces a uniform irradiance distribution in the field stop of Fig. 6. We noted that an ideal objective lens would merely scale the object exitance by  $1/(4(F/\#)^2+1)$  and we asked about the nature of the wavefront incident upon the grating-imaging lens combination just in front of the PtSi FPA. We were able to show that in

$$u_2(x_2, y_2) = \left( \frac{I_0}{4 \cdot F\_num^2 + 1} \right) \frac{\lambda \cdot f_2}{(L_1)^2} \cdot \text{sinc} \left( \frac{x_2}{L_1} \right) \cdot \text{sinc} \left( \frac{y_2}{L_1} \right) \quad (13)$$

collimated space just prior to the grating, the plane wavefront amplitude is given by

$$L_1 = \frac{\lambda \cdot f_2}{D} \quad (14)$$

where

$F\_num$  = Objective lens  $F/\#$ .

$I_0$  = Generalized "Intensity" leaving the object.

$f_2$  = focal length of the collimating lens.

$D$  = Lateral dimension of the square field stop.

To simplify the derivation, we took into account the finite extent of the field stop only, not the objective or collimating lenses. To further simplify the derivation from this point on, we chose not include the finite extent of the grating-imaging lens combination. These approximations result in the following expression for the focal plane irradiance due to an extended object of exitance  $M_{OBJ}$ :

$$E(x_0, y_0) = \left( \frac{M_{OBJ}}{4 \cdot F\_num^2 + 1} \right) \cdot \left( \frac{f_2}{f_3} \right)^2 \cdot \prod_{(i=x,y)} \left[ \sum_{q1_i=-\infty}^{\infty} \sum_{q2_i=-\infty}^{\infty} \sum_{q3_i=-\infty}^{\infty} \sum_{q4_i=-\infty}^{\infty} J_{q1_i} \left( \frac{2 \cdot m}{\pi} \right) J_{q2_i} \left( \frac{2 \cdot m}{3 \cdot \pi} \right) J_{q3_i} \left( \frac{2 \cdot m}{5 \cdot \pi} \right) J_{q4_i} \left( \frac{2 \cdot m}{7 \cdot \pi} \right) \right] \quad (15)$$

$$\left[ \text{rect} \left[ \frac{f_2}{f_3 \cdot D} \cdot (i_0 - q1_i \cdot f_0 - 3 \cdot q2_i \cdot f_0 - 5 \cdot q3_i \cdot f_0 - 7 \cdot q4_i \cdot f_0) \cdot \frac{\lambda \cdot f_3}{\Delta} \right] \right]^2$$

Here,

$$m = m(\lambda) = 2\pi(n-1)t / \lambda$$

$\Delta$  = The grating period.

Since the measurable quantity we sought was the number of electrons collected from each pixel of the PtSi camera, we needed to take into account the spectral response of the FPA and the 300 K background noise. Fortunately, both quantities had been previously measured for this particular camera<sup>5</sup>. The spectral quantum efficiency of the array can be characterized by<sup>5</sup>:

$$\eta(\lambda) = C1 \cdot \frac{h \cdot c}{\lambda} \cdot \left( 1 - \frac{\psi \cdot \lambda}{h \cdot c} \right) \quad (16)$$

with  $C1$  = quantum yield =  $0.190 \text{ ev}^{-1}$  and  $\psi$  = barrier height =  $0.240 \text{ ev}$  by previous measurement<sup>6</sup>. This gave for the number of electrons produced by a pixel during one integration period when the system was viewing an object of temperature  $T$  after a 300 K background offset correction:

$$Ne(x_0, y_0) = T_{opt} \cdot t_{int} \cdot A_{pixel} \cdot \int_{\lambda 1}^{\lambda 2} \eta(\lambda) \cdot E(x_0, y_0, \lambda) d\lambda \quad (17)$$

where

$T_{opt}$  = System optics transmission.

$t_{int}$  = FPA integration time.

$A_{pixel}$  = Pixel area.

$\lambda 2$  = Longest wavelength of interest.

$\lambda 1$  = Shortest wavelength of interest.

and the 973 K object exitance ( $\text{photons/cm}^2\text{-sec.}$ ) with the 300 K background subtracted in equation 15 was given by

$$M_{\text{OBJ}} = \left[ \frac{2 \cdot \pi \cdot c}{\lambda^4 \cdot \left( \exp \frac{h \cdot c}{\lambda \cdot k \cdot T} - 1 \right)} \right]_{T=973} - \left[ \frac{2 \cdot \pi \cdot c}{\lambda^4 \cdot \left( \exp \frac{h \cdot c}{\lambda \cdot k \cdot T} - 1 \right)} \right]_{T=300} \quad (18)$$

For tractable computer implementation, the summations from  $-\infty$  to  $\infty$  in (15) were reduced to summations from  $-2$  to  $2$ . In other words,

$$\sum_{-\infty}^{\infty} \sum_{-\infty}^{\infty} \sum_{-\infty}^{\infty} \sum_{-\infty}^{\infty} \Rightarrow \sum_{-2}^2 \sum_{-2}^2 \sum_{-2}^2 \sum_{-2}^2 \quad (19)$$

The model was implemented in MathCad and run for various combinations of etch depth ( $t$  in Fig. 7) and wavelengths of interest in the 3 to 5  $\mu\text{m}$  band using a constant grating period of  $\Delta = 1/11 \text{ mm}$ . A run for an etch depth of 0.85  $\mu\text{m}$  with  $\lambda_1 = 3.4 \mu\text{m}$  and  $\lambda_2 = 3.6 \mu\text{m}$  and a blackbody temperature of  $T = 973 \text{ K}$  is shown in Fig. 8.

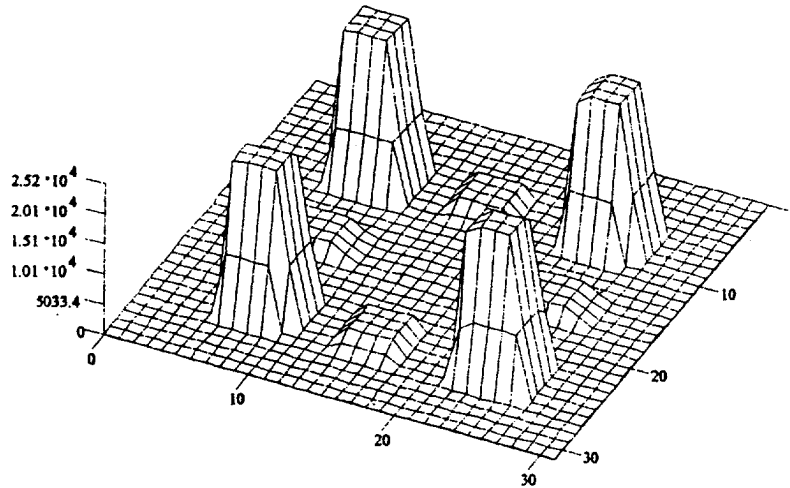


Fig. 8. Simulation run of IR CTIS physical system including PtSi quantum efficiency. Shown in this figure is the number of electrons collected per pixel over the surface of the 256x256 array during one integration time. Pixels have been binned into 8x8 groups to increase computational speed.

Our goal was to achieve uniformity of response across the surface of the PtSi FPA and to compensate for the characteristic falloff of quantum efficiency at longer wavelengths in this type of photodiode array. Numerous simulations were run for etch depths between  $0.3\text{ }\mu\text{m}$  and  $1.0\text{ }\mu\text{m}$  for various wavelength intervals between  $3.4\text{ }\mu\text{m}$  and  $4.9\text{ }\mu\text{m}$ . Based on these simulation runs, it was determined that an etch depth near  $0.7\text{ }\mu\text{m}$  was optimal. Due to the expense and delays associated with outside vendors, we eventually chose to develop grating fabrication capability in-house. A series of small prototype gratings were fabricated on optical quality Gallium Arsenide wafers using a reactive ion etch process. Depths ranging from  $0.6\text{ }\mu\text{m}$  to  $0.9\text{ }\mu\text{m}$  were chosen and evaluated in the breadboard prototype. These results will be discussed in the next section.

Initially, problems were encountered with maintaining a uniform etch depth across a sufficiently large area ( $25\text{mm} \times 25\text{ mm}$ ) to be useful in our instrument. These difficulties were surmounted by increasing the flow rate of the methane and chlorine gas mixture used in the etching chamber and a grating with a 1 micron nominal etch depth was fabricated. A surface profile scan of this grating was taken with a Wyko interferometer and the results appear in Fig. 9.

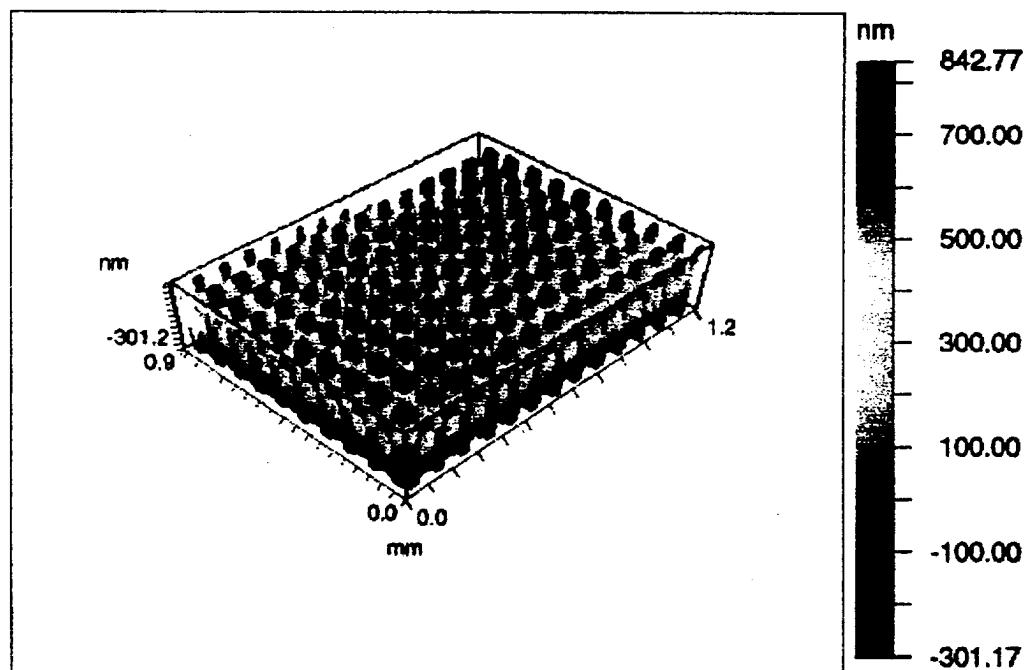


Fig. 9. Wyko interferometer surface profile of the large area crossed binary phase grating fabricated using Reactive Ion Etching at the Optical Sciences Center by Michael Descour and Daniel Simon. Average etch depth came in at  $1.1\text{ }\mu\text{m}$ . (Courtesy M. Descour and D. Simon).

#### D) Breadboard a prototype snapshot imaging spectrometer.

Having been graciously warned that the AFOSR does not like hardware built under 6.1 funding, we nevertheless proceeded to breadboard a prototype snapshot imaging infrared spectrometer system, as specified in our original contract, without hesitation. Clearly, any perceived agenda underlying such an inconsistency could only have been the product of an overactive imagination. During this phase of the project we gained many optical insights into the system shown below in Fig. 10.

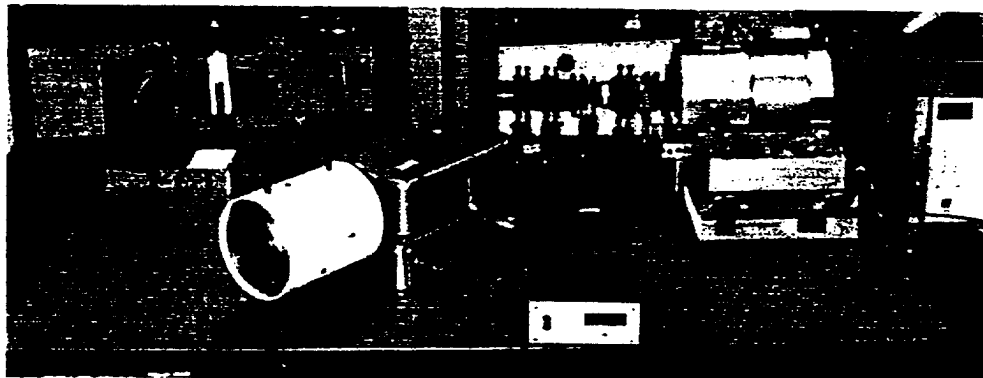


Fig. 10. Prototype snapshot IR imaging spectrometer. In the foreground, a commercial blackbody (white cylindrical object) supplies IR radiation to a Perkin-Elmer monochromator. The exit slit of the monochromator is reflected by a folding mirror into the spectrometer optical train in the right background. From left to right we have 1) a  $f=100$  mm objective lens followed by 2) a 2 mm square field stop. The black conical object with its apex to the left is 3) a 100 mm collimating lens followed by the disperser mount. Finally, on the far left is the 50 mm re-imaging lens attached to the liquid nitrogen dewar which houses the PtSi array. See Fig. 6. for further details. Not shown is the computer and associated frame-grabber card used to digitize the image.

Using this setup, we evaluated small prototype gratings of varying etch depths to determine the optimum depth as mentioned in section C) above. Once we eventually found a way for a commercial frame-grabber board to reliably accept the non-standard video output from the PtSi camera, we were able to acquire full images. The monochromator was used to restrict the spectral bandwidth so that the diffraction efficiency as a function of wavelength could be gauged. The result for one grating appears in Fig. 11.

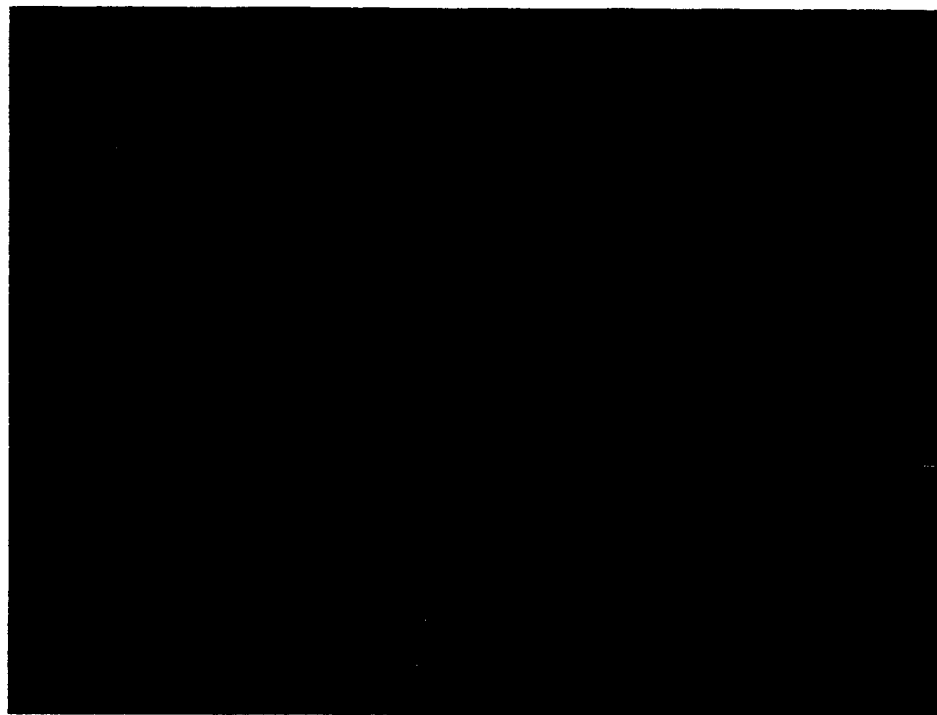


Fig. 11. Graylevel profile of a  $0.85\text{ }\mu\text{m}$  deep grating with a period of  $\Delta = 1/11\text{ mm}$  at a center wavelength of  $\lambda_c = 3.5\text{ }\mu\text{m}$ . The vertical axis is proportional to the number of electrons collected by each pixel of the focal plane array during one integration period. The horizontal axes are proportional to the x and y axis of the focal plane. The blackbody temperature was 973 K.

A comparison with Fig. 8 reveals significant discrepancies with the mathematical model. In particular, the center order in the real data shown above is far greater than predicted by the model. We believe this is due the requirement of having to truncate the quadruple summation in (19) for tractable (12 hrs. on a 266 MHz Pentium II) computer simulation. However, photons from higher order summation terms contribute directly to the zero and first order diffraction patterns in a complex fashion as indicated in (15). More work needs to be done in this area if modeling is determined to be actually important. But as far as disperser design is concerned, we believe we have a workable, if not optimal, large area candidate.

**E) Measure high temperature laboratory targets which approximate actual penetrator debris.**

Actual behind panel debris from Eglin AFB (Tests at Range C-64A) would have been analyzed, had it been made available.

**F) Extract temperature and emissivity values to compare with true parameters.**

This task has been completed for the purposes of software validation. However a serious IR camera malfunction prevented us from completing this phase of the project with an actual snapshot imaging spectrometer. To date we have been unable to fix the problem.

**III. Publications: None.**

**IV. Technical Exchange Meetings:**

Telephone calls and in-person meetings with the technical contract monitor plus several visits by the technical monitor to Tucson.

**V. Travel: None.**

**VI. Problem Areas:**

A clock driver coaxial cable in the IR camera was damaged during routine maintenance. All attempts at repair have failed to date. The camera probably requires major rewiring inside the dewar, but hopefully not a new PtSi array.

## REFERENCES

- 1) W.H. Press, S.A. Teukolsky, W.T. Vetterling, B.P. Flannery, Numerical Recipes in C, 2<sup>ND</sup> Edition., Cambridge University Press, Cambridge, UK (1993), p. 685.
- 2) M.A. Bramson, Infrared Radiation, a Handbook for Applications, Plenum Press: New York (1968), pp. 121-123.
- 3) W.H. Press, S.A. Teukolsky, W.T. Vetterling, B.P. Flannery, Numerical Recipes in C, 2<sup>ND</sup> Edition., Cambridge University Press, Cambridge, UK (1993), p. 390.
- 4) J.W. Goodman, Introduction To Fourier Optics, McGraw-Hill, San Francisco, 1968, pp. 65-70.
- 5) D.L. Perry, Nonuniformity Effects In A Hybrid Platinum Silicide Imaging Device, Ph.D. Thesis, University of Arizona, 1991, p. 179.
- 6) Op. Cit., p 23.

**SECTION IV.**

**BEHIND PANEL DEBRIS TEMPERATURE PROFILOMETRY.**

**EUSTACE L. DERINIAK**

**AND**

**JOHN P. GARCIA**

**UNIVERSITY OF ARIZONA WHITE PAPER  
(F49620-95-1-0456)  
MAY 23 1997**

# Behind Panel Debris Temperature Profilometry

## Objective

The objective of this research is to extend the techniques developed during the first two years of this project. Namely, we will improve the emissivity-temperature recovery algorithm already developed and we will improve the instrumentation that provides the raw data to this algorithm. As in the first phase of this research, the fundamental goal is to investigate ways of providing an absolute temperature map of behind panel debris from penetrating type weapons and to understand the radiative process of the debris itself.

## Background

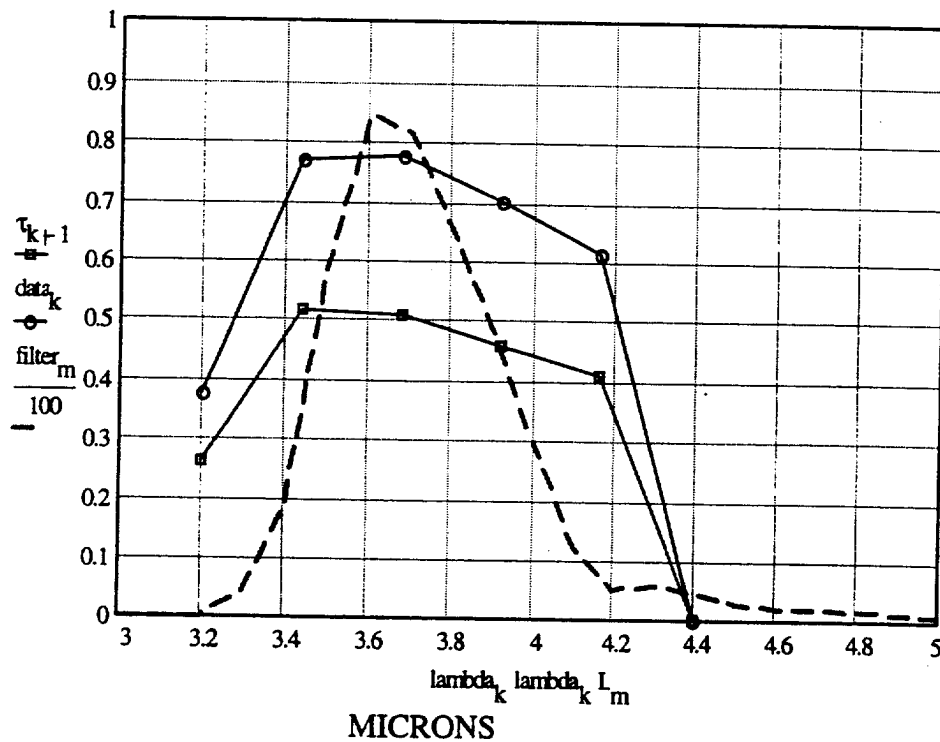
Under the present contract, a unique iterative approach was shown to obtain accurate temperature of a remote object with a complex emissivity profile from measurements of a test object's radiant exitance in six contiguous spectral sub-bands covering the 3.4 to 4.9 micron region. This method does not expand the object's emissivity profile in a polynomial function of wavelength such as

$$\epsilon(\lambda) := a + b\lambda + c\lambda^2 + d\lambda^3$$

which is valid over the entire spectral region. Instead our method expresses emissivity as an independent constant within each spectral sub-band. The emissivity profile for the entire spectral region then is simply the juxtaposition of all the sub-band emissivities. Simulations of noisy data have shown this technique to be effective in recovering target temperatures even when the data signal-to-noise ratio is low. An experimental setup consisting of a hot target, a monochromator and a PtSi camera operating in the 3.4 - 4.9 micron region was used to simulate an infrared imaging spectrometer<sup>1</sup>. The radiation from the target was separated into six bands with center wavelengths of 3.20, 3.44, 3.68, 3.92, 4.16 and 4.40 microns. In Fig. 1, the continuous dashed curve shows the target's true emissivity as measured with a high resolution non-imaging spectrometer. The broad upper trace with circles is the simulated imaging spectrometer output with the instrument spectral response divided out. The lower broad trace with squares is the fit given by our iterative algorithm which converged to within 11 K of the actual target temperature of 973 K, despite less than ideal recovery of the true emissivity profile.

In a parallel effort, an imaging spectrometer using computed tomography was developed for the visible spectrum under another contract. The software will be readily applicable, with minor modifications, to the infrared version of this instrument which is currently under construction. This will enable us to apply the temperature recovery algorithm on a pixel by pixel basis.

# FILTER TRANSMISSION VERSUS WAVELENGTH IN MICRONS



Actual Temperature = 973 K  
Solved Temperature = 962.5 K

Fig. 1 Results of the emissivity-temperature algorithm. The true target emissivity is the continuous dashed line; the measured data for the six spectral bands is the broad upper trace with circles; the output of the program is the broad lower trace with squares.

## Approach

Our approach to the next phase of this research will focus on the fundamental physics of radiating surfaces, the data acquisition system as a whole, the infrared disperser in particular and further evolution of the temperature recovery algorithm. The block diagram of the overall system in Fig. 2 indicates the interrelationship of these components.

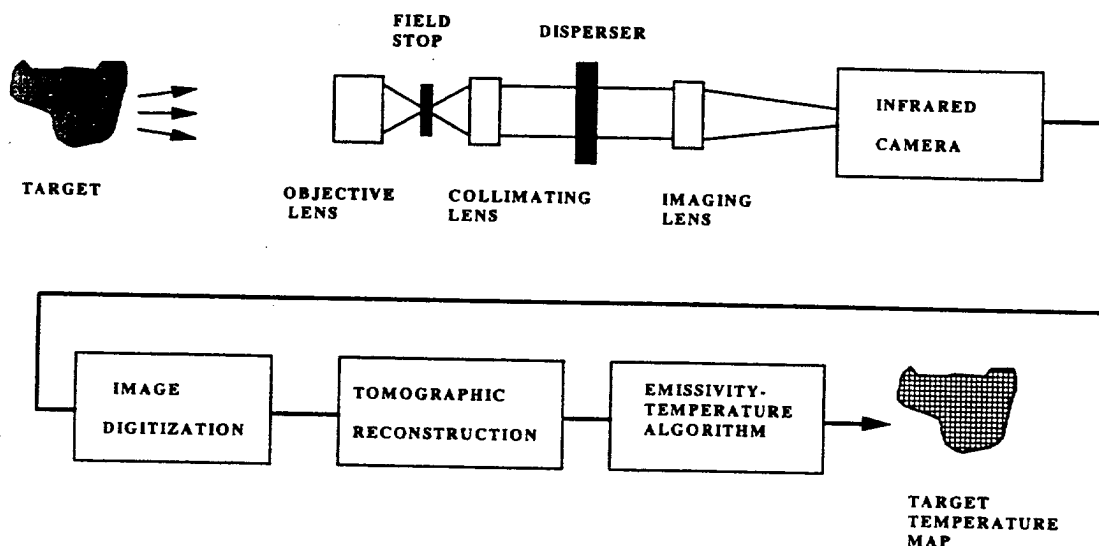


Fig. 2 Overall system block diagram

In the second phase of the research, we will continue to pursue increased understanding of both the measurement technology and the physics of IR radiation production. We will investigate the limitations of the Planck model itself that can influence accuracy. Studies in the 400 nm to 800 nm wavelength range of behind armor debris indicate that emission lines from reacting  $\text{FeO}_2$  can perturb the otherwise  $T = 1050$  K greybody spectrum of the debris<sup>2</sup>. If similar emission lines exist in the 3 - 5 micron region, they could seriously degrade the accuracy of the temperature recovery algorithm. We need to identify potentially reactive species and find ways of incorporating them into the model.

The data acquisition system as a whole can benefit from improved spatial and spectral resolution. For a given focal plane format, both spatial and spectral resolution are primarily determined by the tomographic reconstruction software. By modifying this software we can will greater spatial and spectral resolution than the current goal of 10 x

10 reconstructed pixels with 10 spectral bands per pixel. In addition, the overall throughput of the system can be improved for true IR snapshot imagery to be feasible. Modeling of the present optical system including the current PtSi camera indicates that low SNR will occur at wavelengths beyond 4.5 microns making integration times less than 1/60 of a second a practical impossibility. Since integration times below 100 microseconds are needed to freeze rapidly moving behind panel debris, increased optical throughput and a higher quantum efficiency FPA are required.

For similar reasons, more efficient holographic dispersers must be designed and tested. The current system will employ a simple binary crossed phase grating which will not make efficient use of the available IR radiation from the target. In conjunction with design and fabrication techniques being developed in parallel for the visible version of this instrument, we will fabricate better dispersers.

Finally, additional work needs to be done on the emissivity-temperature algorithm both to improve its performance and to understand its limitations. As it stands, the software is able to take six sub-band data points and solve for six sub-band emissivity values only by imposing numerous constraints upon the solution. While the technique is entirely automatic and needs no user intervention, it is slow and reduces the temperature recovery accuracy. We will investigate methods such as Simulated Annealing which has proven capable of dealing with previously insoluble problems of this type<sup>3</sup>.

## REFERENCES

- 1) *Progress Report for Grant F49620-95-0456*, submitted to Karen Seward, Administrative Contracting Officer, Office of Naval Research, San Diego, CA.
- 2) Chris Anderson, *et al.* "Measurement of behind-armor debris using cylindrical holograms", *Optical Engineering*, 36 (1), pp 40-46, January 1997.
- 3) W.H. Press, *et al.* *Numerical Recipes in C / The Art of Scientific Computing*. (Cambridge: Cambridge University Press, 1992).

**SECTION V.**

**INTERFERING IMAGING SPECTROMETER  
PATENT AWARD.**

**GRANTED TO  
MARK F. HOPKINS  
AFRL/MNSA**

**LETTER AND PATENT GRANT**



DEPARTMENT OF THE AIR FORCE  
AIR FORCE RESEARCH LABORATORY (AFMC)  
EGLIN AIR FORCE BASE, FLORIDA

MEMORANDUM FOR MARK F. HOPKINS  
430 W. NEW ENGLAND AVE  
SUITE 10  
WINTER PARK, FL 32789  
(407) 539-1639

FROM: AFRL/MNMF

SUBJECT: Patent Award and Final Review

1. Congratulations on your being awarded a patent for your outstanding work on the development of a new and novel spectroscopic imaging method. The patent number 5,708,504 for an Interfering Imaging Spectrometer was issued on 13 Jan 98. A copy of this award will be placed in the program files prior to retirement and forwarded to Civilian personnel for inclusion in your records. Your contributions have been recognized as key to future capabilities for research in energetic materials. Recent discussions have indicated interest in further advancing the work you initiated here. Innovative Research investments may be available at some date in the future to support University Research and Post Doctoral Research in development and validation of the empirical models for surface emissivity you discussed in your final report. Future sponsored research would be dependent on this work, based on input from key scientists in various discipline areas.
2. In order to complete and close out the prior research in this area, it is anticipated that a review of the reports and research files be performed during the week of 12-18 April at your facility and University of Central Florida. A research plan from our discussion will be sponsored for briefing to the MN associate chief scientist and to AFOSR (Capt. Brian Sanders).
3. Mr Donald R. Snyder is the point of contact for this effort and can be reached at (850) 882-2005 ext. 257 or (850) 882-5810.

Kenneth L. Echternacht, Jr., Major, USAF  
Chief, Fuzes Branch

Attachment:  
Notification of Patent Award

cc:  
CA-N (Dr. Sierakowski)  
MNOR (Kay Cushing)



**DEPARTMENT OF THE AIR FORCE**  
AIR FORCE MATERIEL COMMAND LAW OFFICE (AFMC)  
WRIGHT-PATTERSON AIR FORCE BASE OHIO

30-Dec-97

MEMORANDUM FOR WL/MNSI (MARK F. HOPKINS)  
101 W. EGLIN BLVD, STE 309  
EGLIN AFB FL 32542

FROM: AFMC LO/JAZ  
2240 B Street, Room 100  
Wright-Patterson AFB, OH 45433-7109

SUBJECT: S/N 08/736,690 (AF Inv D00103) – M. Hopkins – INTERFERING  
IMAGING SPECTROMETER

1. Attached is a copy of the Issue Notification in the matter of the above-identified case. As indicated, the patent issue date is 13 Jan 98 and the patent number is 5,708,504.
2. A copy of the issued patent will be forwarded to you as soon as we receive it.

A handwritten signature in black ink, appearing to read "Bobby D. Searce", is positioned above the typed name.

BOBBY D. SCEARCE  
Chief, Physics Section  
New Technology Division  
Directorate of Intellectual Property Law

Attachment:  
Issue Notification

ISSUE NOTIFICATION



UNITED STATES DEPARTMENT OF COMMERCE  
 Patent and Trade Mark Office  
 ASSISTANT SECRETARY AND COMMISSIONER  
 OF PATENTS AND TRADEMARKS  
 Washington, D.C. 20231

APPLICATION NUMBER	PATENT NUMBER	ISSUE DATE	ATTORNEY DOCKET NO.
08/736,690	5708504	01/13/98	AFD-00103

8504  
 BOBBY D SCEARCE  
 AFMC LO/JAZ BLDG 11  
 2240 B STREET ROOM 100  
 WRIGHT PATTERSON AFB OH 45433-7109

7707

APPLICANT(S) MARK F. HOPKINS, FORT WALTON BEAFLORIDA



**DEPARTMENT OF THE AIR FORCE**  
AIR FORCE MATERIEL COMMAND LAW OFFICE (AFMC)  
WRIGHT-PATTERSON AIR FORCE BASE OHIO

21-Jan-98

MEMORANDUM FOR WL/MNSI (MARK F. HOPKINS)  
101 W. EGLIN BLVD, STE 309  
EGLIN AFB FL 32542

FROM: AFMC LO/JAZ  
2240 B Street, Room 100  
Wright-Patterson AFB, OH 45433-7109

SUBJ: U.S. Patent 5,708,504 – M. Hopkins – INTERFERING IMAGING SPECTRO-  
METER

We are pleased to forward a copy of U.S. Patent 5,708,504, which recently issued on your above-identified invention.

  
THOMAS L. KUNDERT  
Director of Intellectual Property Law

Attachment:  
Patent copy

# United States Patent [19]

Hopkins

[11] Patent Number: 5,708,504

[45] Date of Patent: Jan. 13, 1998

[54] INTERFERING IMAGING SPECTROMETER

[75] Inventor: Mark F. Hopkins, Fort Walton Beach, Fla.

[73] Assignee: The United States of America as represented by the Secretary of the Air Force, Washington, D.C.

5,260,767	11/1993	Cook	356/326
5,276,321	1/1994	Chang et al.	250/226
5,287,214	2/1994	Robertson et al.	356/352
5,297,555	3/1994	Martens	128/665
5,357,340	10/1994	Zochbauer	356/352
5,369,481	11/1994	Berg et al.	356/319
5,371,358	12/1994	Chang et al.	250/226
5,377,003	12/1994	Lewis et al.	356/300

[21] Appl. No.: 736,690

[22] Filed: Oct. 25, 1996

[51] Int. Cl.<sup>6</sup> G01B 9/02

[52] U.S. Cl. 356/346; 356/352

[58] Field of Search 356/345, 346, 356/352

Primary Examiner—Frank G. Font  
Assistant Examiner—Robert Kim  
Attorney, Agent, or Firm—Bobby D. Searce; Thomas L. Kundert

## [57] ABSTRACT

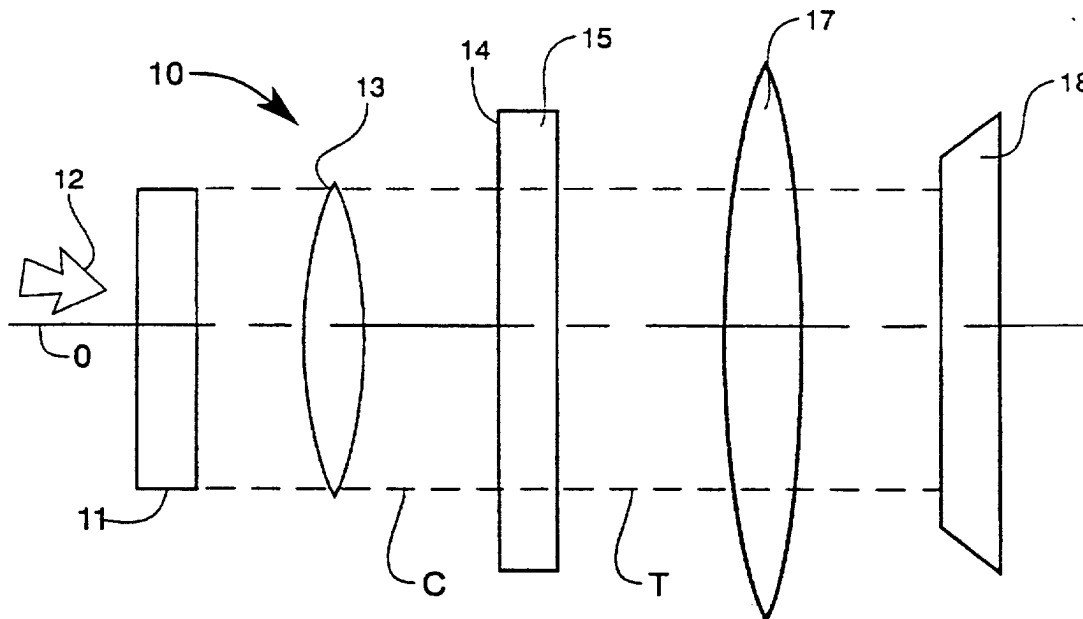
An interfering imaging spectrometer is described wherein a single interference filter disposed in preselected angular relationship with one or more mirrors separates an incoming optical signal or field of view into multiple contiguous images separated spatially and spectrally, each image having a unique spectral content.

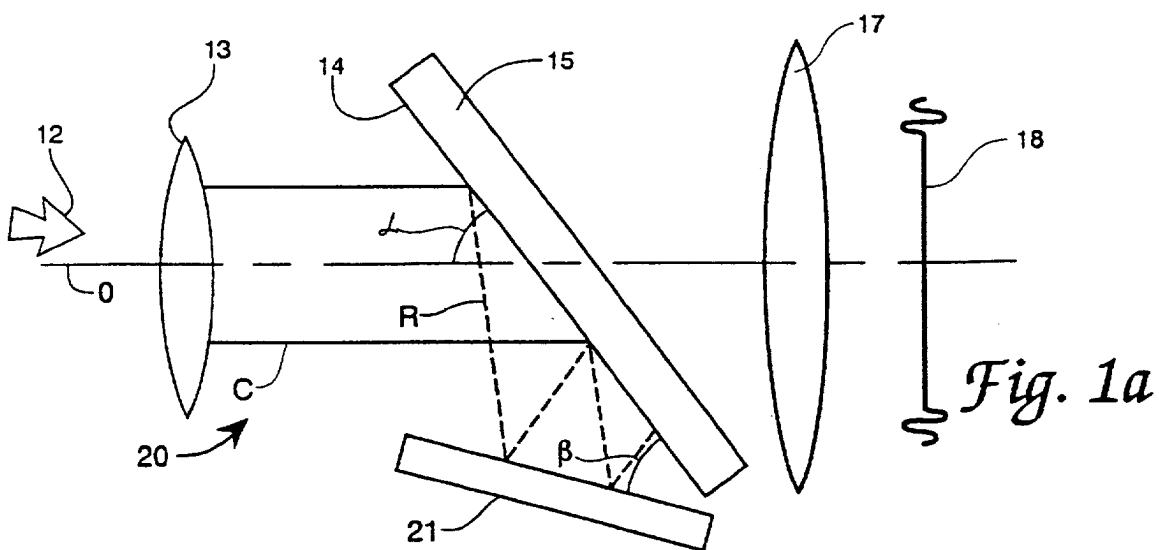
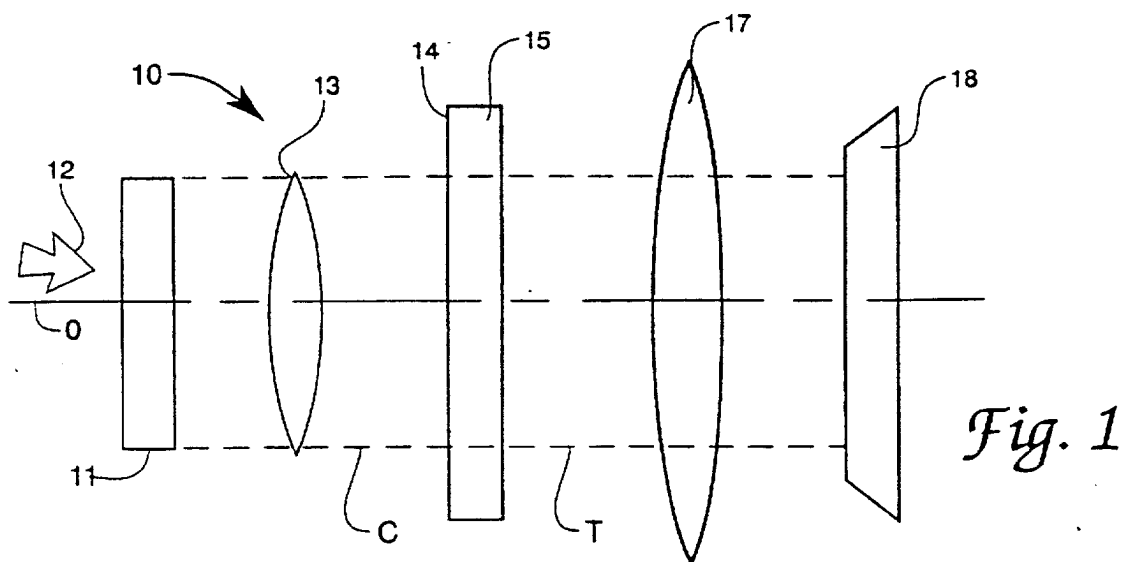
## [56] References Cited

### U.S. PATENT DOCUMENTS

5,116,133	5/1992	Sweeney	356/352
5,177,556	1/1993	Rioux	356/73
5,251,007	10/1993	Rinke	356/319

2 Claims, 3 Drawing Sheets





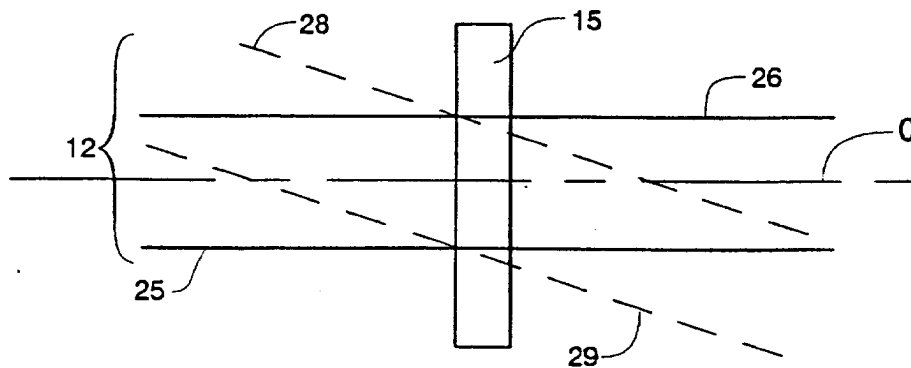


*Fig. 2*

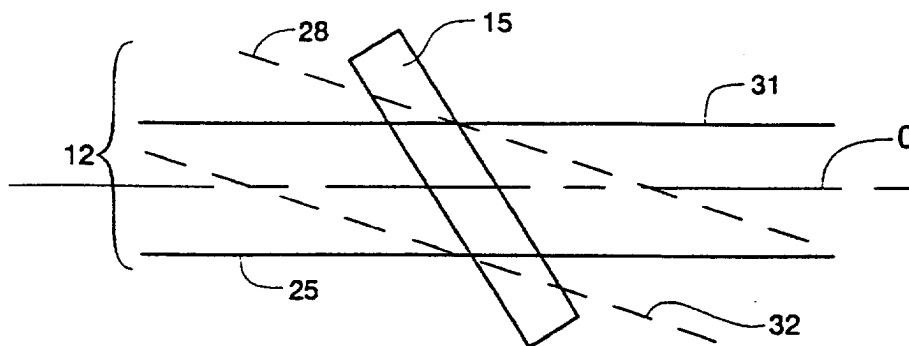
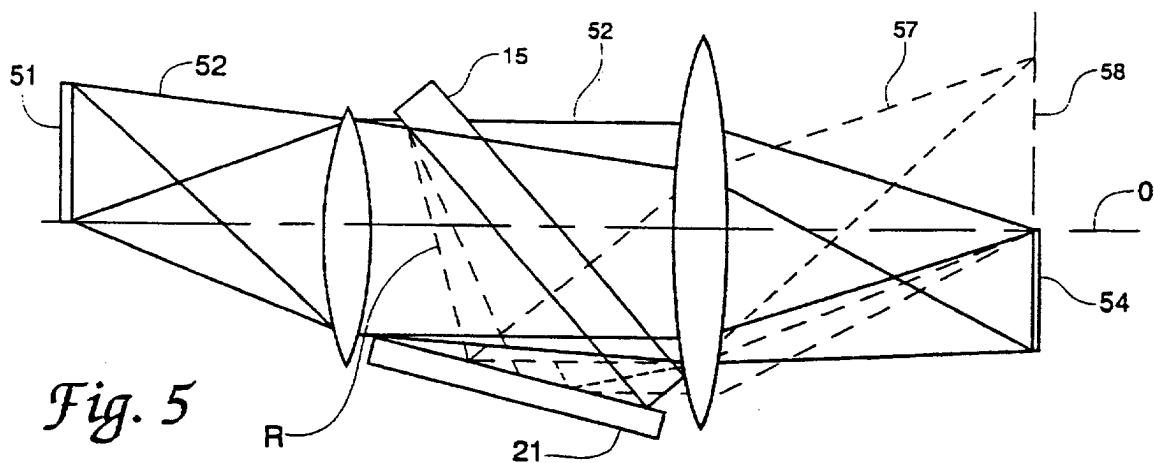
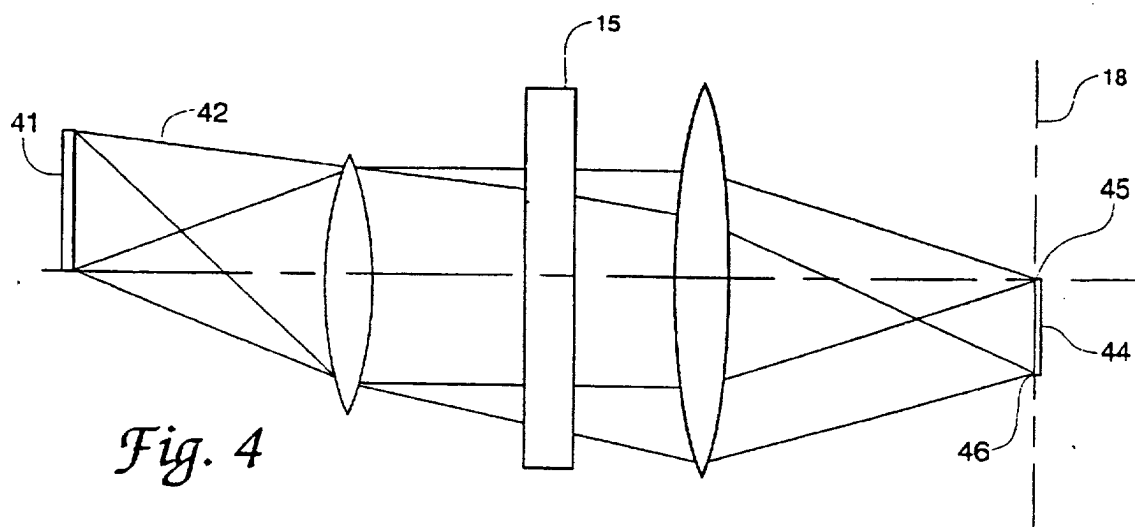


*Fig. 3*



1

## INTERFERING IMAGING SPECTROMETER

## RIGHTS OF THE GOVERNMENT

The invention described herein may be manufactured and used by or for the Government of the United States for all governmental purposes without the payment of any royalty.

## BACKGROUND OF THE INVENTION

The present invention relates generally to imaging spectrometer systems and methods, and more particularly to an imaging spectrometer system having no moving parts and rapid response time.

In the operation of existing commercially available imaging spectrometers, spectral scanning is generally performed using a prism, diffraction grating or filter which is moved into and out of the optical path of an incident optical signal. The time required to scan the spectral energy of the optical signal onto an optical detector, such as a charge-coupled-device, can be at least several milliseconds and is therefore undesirably long. Because certain spectral analysis applications, such as the temperature analysis of projectiles, require fast (of the order of a microsecond) response time, prior art spectrometer systems and methods are inadequate.

The invention solves or substantially reduces in critical importance problems with prior art spectrometer systems and methods by providing an improved imaging spectrometer including a single interference filter for spectral analysis of the incoming signal and takes advantage of the spectral transmission and reflection variations with incident angle of the incoming signal within the interference filter. The invention exhibits a rapid response time in the microsecond range, and multiple images can be formed from a single incoming signal so that a single snapshot will acquire all spectral information of the signal. The spectrometer of the invention has no moving parts and can therefore have a rugged simple structure which is easily and accurately calibrated.

It is therefore a principal object of the invention to provide an improved spectrometer system and method.

It is a further object of the invention to provide an interfering imaging spectrometer system and method.

It is yet another object of the invention to provide an imaging spectrometer having very fast response time.

It is another object of the invention to provide an interfering imaging spectrometer having no moving parts.

It is yet another object of the invention to provide an interfering imaging spectrometer which is rugged in construction and which can be easily and accurately calibrated.

It is another object of the invention to provide an interfering imaging spectrometer having a single spectral filter.

These and other objects of the invention will become apparent as a detailed description of representative embodiments thereof proceeds.

## SUMMARY OF THE INVENTION

In accordance with the foregoing principles and objects of the invention, an interfering imaging spectrometer is described wherein a single interference filter disposed in preselected angular relationship with one or more mirrors separates an incoming optical signal or field of view into multiple contiguous images separated spatially and spectrally, each image having a unique spectral content.

## DESCRIPTION OF THE DRAWINGS

The invention will be more clearly understood from the following detailed description of representative embodi-

2

ments thereof read in conjunction with the accompanying drawings wherein:

FIG. 1 is a schematic block diagram illustrating the essential components of a spectrometer system according to the invention;

FIG 1a is a schematic block diagram of another embodiment of the invention;

FIG. 2 is a schematic illustration of the interaction of incoming optical signals with the interference filter of the FIG. 1 system;

FIG. 3 is a schematic illustration of the interaction of incoming optical signals with the interference filter of FIG. 2 tilted with respect to the optical axis of the FIG. 1 system;

FIG. 4 is a schematic illustration of the interaction of an off-axis incoming optical signal with the interference filter of the FIG. 1 system; and

FIG. 5 is a schematic illustration of the interaction of an off-axis incoming optical signal with the interference filter tilted with respect to the optical axis of the FIG 1 system and with the addition of a mirror for providing multiple images of the incoming signal.

## DETAILED DESCRIPTION

Referring now to the drawings, FIG 1 illustrates in schematic block diagram form the essential components of a representative spectrometer system 10 according to the invention. In system 10, any suitable optical train 11 (mirrors, etc) may be disposed for directing an incoming optical signal 12 along optical axis O onto collimating lens 13. Collimated beam C is then directed onto interference filter 15 having transmittance in a preselected passband. Filter 15 have any desired passband in any selected spectral region, ultraviolet to infrared, depending on the intended use of the invention, the particular selected passband not considered limiting of the invention. For example, in selecting a passband for an incoming signal in the range of about 3 microns ( $\mu\text{m}$ ) to 5  $\mu\text{m}$ , it may be appropriate to select a filter having four filter bands, viz., 3-3.4  $\mu\text{m}$ , 3.5-3.9  $\mu\text{m}$ , 4.04-4.5  $\mu\text{m}$  and 4.6-5.0  $\mu\text{m}$ . Spectral energy within the transmission passband of filter 15 is transmitted as transmitted beam T onto imaging lens 17 and imaged onto optical detector 18 as suggested in the schematic of FIG 1. Optical energy within beam C which is not within the passband of filter 15 is substantially totally reflected from filter 15 at incident surface 14 thereof.

Any suitable optical detector 18 sensitive to the selected passband of filter 15 may be used, within scope of the invention, as would occur to the skilled artisan practicing the invention and guided by these teachings, such as a charge-couple device, photodiode array or infrared array, detector selection therefore not being considered limiting of the invention.

Referring now to FIG. 1a, shown therein is a schematic block diagram of another embodiment of the invention in the form of representative system 20, wherein incoming signal 12 is formed into multiple images separated spatially and spectrally. In accordance with a principle of operation for the FIG. 1a embodiment, filter 15 is disposed at preselected angle  $\alpha$  because the transmission characteristics of interference filter 15 having a specific passband is a function of the angle of incidence of the incident optical energy. Selection of the angle  $\alpha$  of filter 15 with respect to axis O may be made by the skilled artisan practicing the invention and will be the material used and the selected band pass for each of the subsequent filters. Accordingly, one or more mirrors 21 may

be disposed between collimating lens 13 and filter 15 at respective separation angles  $\beta$  and at different planes corresponding to different azimuthal angles of incidence of signal 12 relative to optical axis O (the separation angle  $\beta$  of one such mirror 21 is illustrated in FIG. 1a) to reflect the beam R reflected from surface 14 onto filter 15 at an angle of incidence different from the angle of incidence of collimated beam C. The transmission character of filter 15 is dependent on the cosine of the angle of incidence of the incident beam, and filter 15 therefore transmits differently for the reflected beam R as redirected by mirror 21 than for collimated beam C. The selected angle  $\beta$  between mirror 21 and filter 15 will correspond to a particular field angle for incoming signal 12, and to its unique cosine dependent filter value (passband). Multiple (depending on the number of mirrors 21 included in system 20) contiguous images are therefore formed at detector 18 from a single field of view or incident signal 12, and each such image has its own unique spectral content.

FIG. 2 shows a simplified schematic illustration of the interaction of incoming optical signal 12 with filter 15 in system 10 of FIG. 1. Consider a filter 15 having a bandpass in the red end of the optical spectrum. For an optical signal 12 comprising substantially white light, that portion 25 of signal 12 corresponding to a field angle along optical axis O would result in a transmitted beam 26 in the red corresponding to the filter 15 passband. For any portion 28 of signal 12 corresponding to a field of view at successively greater incidence angles on filter 15, the corresponding transmitted beam 29 would be shifted to a shorter (green) wavelength as a function of the cosine of the angle of incidence. For example, filter 15 has a bandpass at normal incidence of one micron, then for a portion 28 in the field of view incident at  $60^\circ$ , the bandpass would be about one-half micron and somewhat more narrow than the passband at normal incidence. Referring now to FIG. 3, it is noted that if filter 15 is inclined with respect to optical axis O, as, for example, shown in FIG. 1a, portion 25 of signal 12 incident along axis O has a corresponding transmitted beam 31 shifted to the green, and portion 28 has a corresponding transmitted beam 32 shifted further into the blue. Accordingly, and with reference now to FIG. 4, wherein filter 15 is disposed for normal incidence of signal 42 along optical axis O, object 41 comprising a white source would result in an image 44 on detector 18 having an end 45 nearest axis O shifted in spectral content to the yellow and an end 46 furthest from axis O shifted in spectral content further into the blue.

Referring now to FIG. 5, shown therein is a schematic illustration of the interaction of a white signal 52 from object 51 with inclined (with respect to axis O) filter 15 and mirror 21 as in the FIG. 1a system. That portion of signal 52 which passes through filter 15 without reflection is indicated by solid lines and results in a first image 54 having, similarly to the illustration of FIG. 4, spectral content shifted toward the yellow nearest axis O and further into the blue furthest from axis O. In addition, reflected portion R (shown by broken lines) of signal 52 is redirected toward filter 15 by reflection off mirror 21, where the total deviation is now twice the separation angle between filter 15 and mirror 21, which results in a second transmitted beam 57 (also shown by

broken lines) and a second image 58 shifted in spectral content further into the red with distance from axis O. Each additional mirror 21 (not shown) may be disposed at a respective preselected angles with respect to filter 15 to provide an additional image contiguous with images derived from reflections from the other mirrors, each such image containing its unique spectral content. Contiguous images will result where the separation angle between filter 15 and a respective mirror 21 is one-half the maximum field angle subtended by the object.

The invention therefore provides an interfering imaging spectrometer wherein a single interference filter and detector separates an image into its spectral components, and a single set of optics collects all optical energy needed to form the desired images. The invention has no moving parts, is simple and accurate in its calibration, and is highly light efficient, which is important for high speed applications. It is understood that modifications to the invention may be made as might occur to one with skill in the field of the invention within the scope of the teachings herein and of the appended claims. All embodiments contemplated hereunder which achieve the objects of the invention have therefore not been shown in complete detail. Other embodiments may be developed without departing from the spirit of the invention or from the scope of the appended claims.

I claim:

1. An interfering imaging spectrometer system, comprising:

- (a) optical means for directing an optical signal along a preselected optical axis;
- (b) a collimating lens disposed along said optical axis for collimating said optical signal and directing a collimated optical signal along said optical axis;
- (c) an interference filter disposed along said optical axis for selectively filtering said collimated optical signal, said interference filter having transmittance in a preselected passband and disposed at a preselected angle to said optical axis for transmitting a first transmitted signal along said optical axis and reflecting a reflected signal at an angle corresponding to said preselected angle of said interference filter;
- (d) a mirror disposed near said interference filter in preselected angular relationship to said interference filter and said optical axis for directing said reflected signal onto said interference filter and providing a second transmitted signal along said optical axis and a second reflected signal from said interference filter, said second transmitted signal having spectral content dependent on the angular relationship between said interference filter and said mirror and defining an image separated spatially and spectrally from the image defined by said first transmitted signal; and
- (e) an imaging lens and an optical detector disposed along said optical axis, said imaging lens disposed for imaging the transmitted signals onto said optical detector.

2. The spectrometer system of claim 1 wherein said optical detector is a charge-couple device, photodiode array or infrared array.

\* \* \* \* \*

DISTRIBUTION LIST  
AFRL-MN-EG-TR-2001-7066

Defense Technical Information Center 8725 John J. Kingman Road, Ste 0944 Ft Belvoir, VA 22060-6218	1
----------------------------------------------------------------------------------------------------------	---

**EGLIN AFB OFFICES:**

AFRL/MN CA-N	1
AFRL/MNOC-1 (STINFO Office)	1
AFRL/MNGG	1

## FOOTNOTES

- <sup>1</sup> Bramson.
- <sup>2</sup> Thermal light as a maxwell-boltzman distribution ref.
- <sup>3</sup> Planck distribution ref.
- <sup>4</sup> V.N Snopko, "Methods of optical polychromatic pyrometry.
- <sup>5</sup> V.N Snopko, "Methods of optical polychromatic pyrometry.
- <sup>6</sup> G.A. Hornbeck, "Optical Methods Of Temperature Measurements", Applied Optics vol. 5 No. 2, pp. 179-186, Feb. 1966.
- <sup>7</sup> D.P. deWitt, "inferring temperature from optical radiation measurements", Optical Engineering vol. 25, pp. 596-601, April 1986.
- <sup>8</sup> Y.W. Zhang et al., "Quantitative measurements of ambient radiation, emissivity and truth temperature of a graybody: methods and experimental results", Applied Optics vol. 25 No. 20, pp. 3683-3689, Oct. 1986.
- <sup>9</sup> Insert emissivity variation with direction.
- <sup>10</sup> Hecht p112.
- <sup>11</sup> papers on emissivity variation with temp.
- <sup>12</sup> B.K. Tsai, Dual-wavelength radiation thermometry: emissivity compensation algorithms, MSME thesis, Prude University, West Lafayette, In, 1990.
- <sup>13</sup> Table.
- <sup>14</sup> IRIS TR.
- <sup>15</sup> Descors dissertation.
- <sup>16</sup> Japanese paper.
- <sup>17</sup> Moving filter inst. Ref.
- <sup>18</sup> Graduated filter ref.
- <sup>19</sup> Framing camera ref.
- <sup>20</sup> Scanning Fabry-Perot ref.
- <sup>21</sup> Michelson FTS.
- <sup>22</sup> Born and Wolf.
- <sup>23</sup> E. Linderman, Concept of the spectral emissivity and temperature of surfaces with a Fourier transform IR spectrometry,
- <sup>24</sup> Descour's dissertation.
- <sup>25</sup> Thermal light reference.
- <sup>26</sup> how is this two level system broadband.
- <sup>27</sup> why is adding more levels trivial.

- 
- <sup>28</sup> Drude, P., "Bestimmung der Optischen Constanten der Metalle," Ann. Physik 64, 159, 1896; available as AFCRL translations "Demonstration of the optical constants of metals".
- <sup>29</sup> Dipole approx. Rick's notes.
- <sup>30</sup> Pegembarium background polarization is small.
- <sup>31</sup> Absorption and index of refraction (Peg)
- <sup>32</sup> relaxation time for metals (Peg).
- <sup>33</sup> Bramson wavelength profile.
- <sup>34</sup> E and H fields for the system are.
- <sup>35</sup> dielectric function is small compared to the real part and can be neglected.
- <sup>36</sup> plasma frequency in the ultraviolet.
- <sup>37</sup> D. P. DeWitt, "Comments on the Surface Characteristics of Real Metals,"
- <sup>38</sup> Reference on radiation from bound states.
- <sup>39</sup>
- <sup>40</sup> Numerical Recipes
- <sup>41</sup> Numerical Recipes
- <sup>42</sup> Numerical Recipes
- <sup>43</sup> W. L. Wolfe and G. J. Zissis, *The Infrared Handbook*, 1978, Washington, D.C.: Office of Naval Research, Department of the Navy, pg. 2-77.